This is to certify that the
dissertation entitled

ELECTROMAGNETIC INTERACTIONS WITH MATERIALS:
MAGNETO-DIELECTRIC COMPOSITES DESIGN AND
DEVELOPMENT OF A NOVEL MICROWAVE HEATING DEVICE

presented by

SUSAN A. FARHAT

has been accepted towards fulfillment
of the requirements for the

Ph.D. degree in Chemical Engineering

Major Professor's Signature

August 20, 2010

Date

ELECTROMAGNETIC INTERACTIONS WITH MATERIALS: MAGNETO-DIELECTRIC COMPOSITES DESIGN AND DEVELOPMENT OF A NOVEL MICROWAVE HEATING DEVICE

By

SUSAN A. FARHAT

A DISSERTATION

Submitted to
Michigan State University
in partial fulfillment of the requirements
for the degree of

DOCTOR OF PHILOSOPHY

Chemical Engineering

2010

ABSTRACT

ELECTROMAGNETIC INTERACTIONS WITH MATERIALS:
MAGNETO-DIELECTRIC COMPOSITES DESIGN AND
DEVELOPMENT OF A NOVEL MICROWAVE HEATING DEVICE

By

SUSAN A. FARHAT

Electromagnetic interactions with materials dictate their performance for several applications ranging from wireless communications to energy transport. Understanding how these interactions are affected by material properties is essential for improving application performance and was the underlying theme for this work. Projects included the design and fabrication of magneto-dielectric composites and the development of a novel microwave heating device for activated carbon regeneration.

Engineered magneto-dielectric materials differ from conventional electromagnetic materials due to their enhanced magnetic properties; these materials can increase bandwidth and efficiency for a variety of technologies. However, naturally occurring magneto-dielectric materials are often non-magnetic and exhibit a large loss at frequencies greater than 1GHz. The goal of this project was to design and fabricate materials with enhanced dielectric and magnetic properties at GHz frequencies. Preliminary experimental work was focused on investigating polymer composites with spherical iron oxide nanoparticles; very large loadings of iron oxide were necessary to increase the magnetic permeability, at the cost of material integrity. Alternatively, by using frequency selective surface (FSS) layers within a polymer matrix, the design objective was successfully met. The FSS layers were designed as periodic metallic

arrays, which acted as "inductive inclusions" within the polymer, collectively causing an effective susceptibility due to the interactions between inclusions and a self inductance of the inclusions, resulting in an enhanced magnetic response. The shape, dimension, and periodicity of the metallic elements of the array were variables for the final design and determined the effective properties and operational bandwidth for the composites. These materials were designed to have a permittivity and permeability greater than 2, with very low loss, from 2-5GHz. The details of the design, fabrication, and characterization of these materials will be presented in this work.

While the focus of the first project was primarily materials design, the second project involved the development of a novel application, based on the dielectric properties of the material. Activated carbon is often used as an adsorbent for applications involving removal of toxic effluents from waste streams and emissions. It has been shown that high power microwave heating is a promising alternative method to heat small volumes of activated carbon. In contrast, some applications may require heating large volumes of carbon with lower power inputs; hence, developing a novel microwave heating applicator would be important for eliminating the problem of "hot spots" found often in conventional microwave cavity heating. An applicator similar to a coaxial transmission line was designed at 2.45GHz to heat activated carbon using under 120 Watts of power; bench-top systems were constructed to analyze the efficiency of the design. An energy balance was used to model the temperature throughout the carbon in the device. Results of the device design, experimentation, and modeling will be discussed.

To my mother, my sisters and brothers,
and in memory of my father

ACKNOWLEDGEMENTS

I am very fortunate to have had the opportunity to work under the guidance of Professor Martin Hawley, whose constant encouragement and support throughout my time as a graduate student have been invaluable; his mentoring has helped me become a better scientist and researcher, for which I will always be grateful.

I would also like to acknowledge my committee members – Professors Shanker Balasubramaniam, Leo Kempel, and Krishnamurthy Jayaraman – for their helpful discussions and insight during my thesis work, as well as for teaching several courses that were essential for me to make progress throughout my Ph.D. program. Special thanks are due to Shanker and Leo for closely assisting with my work; their collaboration with our group and additional guidance were always much appreciated.

Further thanks are extended to past and current graduate students and other lab personnel who helped me considerably with many aspects of my work – Brian Wright, Daniel Killips, Nathan Kornbau, Ben Omell, Neil Murphy, Liming Zong, and Raoul Ouedraogo. This work would not have been possible without their assistance in the lab. Special acknowledgement is also due for fellow grad students – past and present – outside of my lab, who I have met throughout my time at MSU, for their companionship and valuable advice.

Lastly, I am overly grateful for my family, for their neverending love and encouragement.

TABLE OF CONTENTS

LIST OF TABLES x

LIST OF FIGURES xi

CHAPTER 1 : Introduction 1
1.1 Scope of Work 1
1.2 Problem Statement and Objectives 1
1.2.1 Magnetic RF Composites with Tailored Properties 1
1.2.2 Microwave Applicator Design 3

CHAPTER 2 : Introduction to Electromagnetic Properties and Materials 5
2.1 Maxwell's Equations 5
2.2 Electromagnetic Properties 6
2.2.1 Permittivity 6
2.2.2 Permeability 8
2.2.3 Homogenization and Effective Electromagnetic Properties 9
2.3 Materials and Applications 10
2.3.1 Radio Frequency Materials 10
2.3.2 Composites 12
2.3.3 Characterization Techniques 14
2.4 Electromagnetic Materials Design Challenges 15
2.4.1 Design Limits 15
2.4.2 Metamaterials and Composites 16
2.4.3 Previous Work 18
2.5 Objectives and Future Impact 19

CHAPTER 3 : Inclusions-based Magneto-dielectric Composites 21
3.1 Approach 21
3.2 Experimental Methods 23
3.2.1 Choice of Materials 23
3.2.2 Composite Synthesis 24
3.3 Characterization 26
3.3.1 Dispersion Quality 26
3.3.2 Effective Permittivity and Permeability 28
3.3.3 Thermal Analysis 34
3.4 Related Simulations 35
3.5 Conclusions 37

CHAPTER 4 : Composites with Frequency Selective Surface Layers 39
4.1 What is a Frequency Selective Surface (FSS)? 39
4.1.1 FSS Definition 39
4.1.2 FSS Applications 41
4.2 FSS Elements and Equivalent Circuit Theory 41

4.3 FSS Design Approach 44
4.3.1 FSS Element Design 44
4.3.2 Transmission and Reflection Characteristics 45
4.4 Square Loop FSS Layered Composites 51
4.4.1 FSS Array and Composite Geometry 51
4.4.2 Effects of Polymer Layer Characteristics 52
4.4.3 Effects of Element Size and Periodicity 60
4.4.4 FSS Composite in a Waveguide vs. Infinite FSS Composite 67
4.4.5 Alternative Element Geometries – Hexagonal Loop 71
4.4.6 Manufacturing Uncertainty Analysis 74
4.4.7 Angle of Incidence Dependence 79
4.4.8 Polarization Effects 81
4.5 Composites with Multiple FSS Layers 83
4.6 FSS Layered Composite Fabrication and Characterization 89
4.6.1 FSS Element Patterning 89
4.6.2 FSS Layered Composite Fabrication 93
4.6.3 FSS Composites Characterization in a Waveguide 94
4.7 Design Alternatives 97
4.7.1 Frequency Operation 97
4.7.2 Nanoparticle Reinforcement 100
4.8 Conclusions and Outlook 100

CHAPTER 5 : Microwave Applicator Design for Activated Carbon 102
5.1 Background 102
5.1.1 Gasoline Emissions Control and Activated Carbon 102
5.1.2 Microwave Heating of Activated Carbon 103
5.1.3 Microwave Mechanisms and Materials Interactions 104
5.2 Dielectric Characterization 106
5.2.1 Dielectric Properties, Measurement, and Microwave Effects 106
5.2.2 Dielectric Properties of Activated Carbon 108
5.3 Microwave Applicator Design 113
5.3.1 Design Rationale 113
5.3.2 Design Results 117
5.3.3 Bench-top System Construction 121
5.4 Microwave Applicator Performance 123
5.4.1 Experimental Set-up 123
5.4.2 Temperature Profile Measurements 123
5.4.3 Design Modifications 129
5.4.3.1 Change in Device Length 129
5.4.3.2 Addition of Shorting Plate and Insulation 130
5.4.3.3 Power Cycling 135
5.5 Modeling Microwave Heating 137
5.5.1 Energy Balance 137
5.5.2 Theoretical vs. Measured Temperature Profiles 142
5.5.3 Effect of Nusselt Number 144
5.6 Conclusions 144

CHAPTER 6 : Conclusions and Future Work **146**
6.1 Magneto-dielectric Composites 146
6.1.1 Summary of Materials Design Results 146
6.1.2 Future Impact and Outlook 148
6.2 Development of a Microwave Applicator for Activated Carbon 149
6.2.1 Summary of Applicator Design Results 149
6.2.2 Future Design Considerations 150

APPENDIX A: Extracting effective electromagnetic properties **151**

APPENDIX B: Modeling of microwave heating **154**

BIBLIOGRAPHY **157**

LIST OF TABLES

Table 4.1. Cases for infinite slabs with hypothetical permittivity, permeability and slab thickness for reflection and transmission analysis. 49

Table 4.2. Composite and FSS array conditions for varying total thickness. 53

Table 4.3. Composite and FSS array characteristics for varying polymer substrates..... 57

Table 4.4. FSS composite geometries corresponding to various FSS element sizes and periodicities. 60

Table 4.5. Hexagonal loop FSS array and composite dimensions..... 72

Table 4.6. Manufacturing uncertainty analysis cases for flaws in the FSS elements for Case T1 (Table 4.1). 75

Table 4.7. Multi-layer FSS composites with varying polymer layer thicknesses..... 84

Table 5.1. Dielectric constant, dielectric loss factor, and average standard error for activated carbon. 111

Table 5.2. Range of reflected power for varied power inputs..... 124

Table 5.3. Average reflected power for different power inputs for 9" microwave applicator with and without a shorting plate..... 133

LIST OF FIGURES

Figure 2.1. Permittivity vs. frequency (Hz) (adapted from [12]). 7

Figure 2.2. Homogenization and effective electromagnetic properties of composites... 10

Figure 2.3. Electromagnetic materials designed. 17

Figure 3.1. Design cycle approach – material choice, simulations/modeling, experimental validation. 22

Figure 3.2. Comparison of magnetic materials dipole arrangement. 24

Figure 3.3. FTIR results for Fe_3O_4 nanopowder – surface treatment analysis 27

Figure 3.5. Dielectric test fixture for characterization. 28

Figure 3.6. Magnetic test fixture for characterization. 29

Figure 3.7. Dielectric characteristics for iron oxide nanocomposites 30

Figure 3.8. Magnetic characteristics for iron oxide nanocomposites. 31

Figure 3.9. Effects of temperature and cure time on the dielectric properties for iron oxide nanocomposites (5 wt.% Fe_3O_4). 33

Figure 3.10. Thermal analysis of iron oxide nanocomposites. 35

Figure 3.11. Predicted permeability for composites comprised of infinite yttrium iron garnet (YIG) layers in a Teflon matrix. 36

Figure 3.12. Predicted permittivity and permeability for composites comprised of yttrium iron garnet (YIG) rods in a Teflon matrix. 36

Figure 4.1. Conceptual design for composites with frequency selective surface layers. 40

Figure 4.2. Typical FSS element types shown by groups 42

Figure 4.3. Complementary FSS arrays 43

Figure 4.4. Equivalent circuit theory applied to FSS arrays. 44

Figure 4.5. Incident plane wave on the surface of a dielectric slab. 46

Figure 4.6. Transmission power (%) vs. frequency (GHz) for varying slab thickness for hypothetical material ($\varepsilon'=2$, $\mu'=1$, no loss). 48

Figure 4.7. Transmission power behaviour for a slab of hypothetical material, corresponding to Table 4.1. 50

Figure 4.8. FSS layered composite layout. 52

Figure 4.9. Transmission characteristics for composites with varying thickness, corresponding to Table 4.2. 54

Figure 4.10. Effective permittivity and permeability vs. frequency (GHz) for varying composite thickness, corresponding to Table 4.2 55

Figure 4.11. Loss characteristics for varying composite thickness, corresponding to Table 4.2. 56

Figure 4.12. Transmission characteristics for composites with varying polymer layer materials, corresponding to Table 4.3 58

Figure 4.13. Effective permittivity and permeability vs. frequency (GHz) for varying polymer dielectric properties, corresponding to Table 4.3. 59

Figure 4.14. Transmission characteristics for FSS layered composite with varied element size, corresponding to Table 4.4. 61

Figure 4.15. Effective properties for FSS layered composites with varying element size, corresponding to Table 4.4. 62

Figure 4.16. Loss characteristics for FSS layered composite with varied element size, corresponding to Table 4.4. 63

Figure 4.17. Transmission data comparison for FSS composites with varied element size and periodicity, corresponding to Table 4.4. 65

Figure 4.18. Effective properties for FSS layered composites with varying element size and periodicity, corresponding to Table 4.4. 66

Figure 4.19. HFSS simulation geometry for the material within a waveguide. 67

Figure 4.20. Transmission vs. frequency (GHz) for an infinite FSS array, 3x3 FSS array, and 6x6 FSS array 68

Figure 4.21. Reflection and transmission behavior for an infinite FSS vs. an FSS in a waveguide. 69

Figure 4.22. Effective permittivity (ε'_{eff}) and permeability (μ'_{eff}) vs. frequency (GHz) for both an infinite FSS and FSS in a waveguide. 70

Figure 4.23. Hexagonal loop FSS elements geometry 71

Figure 4.24. Effective electromagnetic properties for varying hexagonal loop FSS array geometries, corresponding to Table 4.5 73

Figure 4.25. Effective permeability (μ'_{eff}) vs. frequency (GHz) for hexagonal loop and square loop FSS array layered composites. 74

Figure 4.26. Performance characteristics for various flawed FSS samples compared to the original case. 76

Figure 4.27. Transmission data for FSS layered composites with air bubbles within the matrix and at the interface of the FSS layer. 77

Figure 4.28. Effective electromagnetic properties for hexagon loop FSS composites with air bubbles within the polymer layers and at the interface. 78

Figure 4.29. Composite performance for varying scan angle for Case S2 with a polyethylene substrate (Table 4.4) 79

Figure 4.30. Composite performance for varying scan angle for Case S3 with an epoxy substrate (Table 4.4). 80

Figure 4.31. Transmission characteristics comparison for TE and TM polarizations. 82

Figure 4.32. Multi-layer FSS composite geometry 83

Figure 4.33. Transmission characteristics for multi-layer FSS composites. 85

Figure 4.34. Effective properties for multi-layer FSS composites of total thickness 30mm. 86

Figure 4.35. Effective properties for multi-layer FSS composites of total thickness 24mm. 87

Figure 4.36. Permeability loss tangent, μ''_{eff}/μ'_{eff}, for multi-layer FSS composites, corresponding to Table 4.7. 88

Figure 4.37. Photolithography process for patterned arrays. 90

Figure 4.38. Square loop slots and square loop silver elements etched on polyethylene films. 91

Figure 4.39. Square loop (top) and hexagonal loop (bottom) FSS elements patterned on an epoxy substrate (scale in mm) 92

Figure 4.40. Set-up for waveguide measurement of FSS layered composites. 94

Figure 4.41. Comparison between simulated and measured results for hexagonal loops FSS layered composite. 95

Figure 4.42. Comparison between simulated and measured results for square loop FSS layered composite 96

Figure 4.43. High frequency effective properties for square loop FSS composite (total thickness = 10mm) 98

Figure 4.44. High frequency effective properties for square loop FSS composite (total thickness = 20mm) 99

Figure 5.1. Activated carbon morphology: pellets, loose powder, and compressed powder disk 109

Figure 5.2. Dielectric properties for saturated and unsaturated activated carbon pellets as a function of temperature 110

Figure 5.3. Permittivity vs. frequency (MHz) for unsaturated activated carbon disks. 112

Figure 5.4. Design concept for transmission line heating device. 115

Figure 5.5. Microwave heating applicator bench top system set-up. 122

Figure 5.6. Outer conductor with ports for temperature measurement and slots for vapor flow 122

Figure 5.7. Microwave applicator bench-top system – experimental set-up. 123

Figure 5.8. Temperature (°C) vs. time (min) for varying power inputs measured 1" from the start of the transmission line. 125

Figure 5.9. Temperature (°C) vs. time (min) for varying lengths along the 18" applicator with 120 Watts of input power. 126

Figure 5.10. Temperature (°C) vs. time (min) comparisons for radial measurements for 18" microwave applicator, input power = 80 Watts. 127

Figure 5.11. Temperature (°C) vs. time (min) at location S1-a for varying temperature probe depth for the 18" microwave applicator, input power = 85 Watts. 127

Figure 5.12. Outgoing power (W) vs. time (s) for 18" microwave applicator with varying input power. 128

Figure 5.13. Revised (shortened) microwave heating device outer conductor with ports for temperature measurements and slots for vapor flow. 129

Figure 5.14. Temperature (°C) vs. time (min) for 9" microwave heating applicator with 80 Watts of input power. 130

Figure 5.15. % Power absorbed by carbon vs. time (min) for 9" microwave applicator for varying input power. 131

Figure 5.16. Temperature (°C) vs. time (min) for 9" microwave applicator with addition of a shorting plate with 100 Watts of input power. 132

Figure 5.17. Temperature (°C) vs. time (min) for 18" microwave applicator with and without insulation, with input power of 100 Watts. 134

Figure 5.18. Temperature (°C) vs. time (min) for 9" microwave applicator with insulation, with input power of 75 Watts 135

Figure 5.19. Temperature (°C) vs. time (min) for 9" microwave applicator with insulation and shorting plate, with cycling of power at the end of heating. 136

Figure 5.20. Temperature (°C) vs. time (min) for 9" microwave applicator with additional shorting plate and insulation, with cycling of power throughout heating time. 137

Figure 5.21. Energy balance diagram for microwave heating applicator system. 138

Figure 5.22. Shell balance used to solve the overall energy balance at a location, R from the inner conductor. 139

Figure 5.23. Comparison of temperature profiles (predicted vs. experimental) for 18" microwave heating applicator 143

Figure 5.24. Temperature (°C) vs. time (sec) for 100 Watts forward power and varying Nusselt number. 144

CHAPTER 1 : Introduction

1.1 Scope of Work

Electromagnetic interactions with materials dictate the performance of these materials for various applications ranging from wireless communications to energy transport. Understanding how these interactions are controlled by the material's dielectric and magnetic properties (permittivity and permeability, respectively) as described by Maxwell's equations was the central theme for this work. Both projects are based on these fundamental equations – first, designing materials to have specific properties for improved performance in radio frequency (RF) applications and secondly, designing a novel microwave applicator to heat activated carbon, a design that would be based on the carbon's dielectric properties.

1.2 Problem Statement and Objectives

1.2.1 Magnetic RF Composites with Tailored Properties

Wireless energy transport and wireless communications could be key technologies to addressing the several major challenges in the future – for instance, efficiently delivering reliable energy or developing an improved network of efficient sensor systems. Materials design and engineering can offer a means for improving performance for such systems, with new advanced materials development with better electromagnetic and mechanical properties. For this project, the goal was to design and

fabricate electromagnetic materials that would successfully address the key challenges associated with these technologies.

There are several challenges associated with electromagnetic materials design and application performance – including difficulties in size reduction, narrow bandwidth, and difficult impedance matching [1-6]. For example, to improve the performance of patch antennas, a high permittivity substrate for the antenna has been used for the antenna substrate; however, this can result in highly concentrated fields around the high permittivity region, as well as narrowband characteristics and low efficiency. Moreover, the high permittivity results in low impedance, causing difficulty in impedance matching the antenna. A solution to this problem would be to develop materials with an enhanced relative permeability, in addiction to an increased relative permittivity, resulting in a material with more moderate impedance and an improved bandwidth [1]. Additionally, it has been seen that an antenna patch with an enhanced permeability would allow for a wider bandwidth over the same antenna patch with permeability equal to unity because unlike permittivity, increased permeability does not reduce the patch bandwidth. This substrate will result in a patch resonant length that is reduced by the increased permeability; hence, a much shorter and smaller patch will have roughly the same bandwidth as the patch with an increased permittivity only [2].

From the standpoint of the engineer, the ability to tailor the material properties to meet the requirements for a specific application would be important. The current design challenges have lead to the development of advanced materials with specific electromagnetic properties at GHz frequencies. Magneto-dielectric materials are defined

as having enhanced dielectric and magnetic properties as well as low dielectric and magnetic loss.

Unfortunately, naturally occurring magneto-dielectric materials have high loss and are often non-magnetic for higher GHz frequencies [1-6]. One possible method to achieve this design is through the use of composite materials. The purpose of this research is to develop a means to design and fabricate materials that would be useful for these applications. The overall goal of this project was to design magneto-dielectric materials with magnetic permeability greater than 1, permittivity not much larger and preferably smaller, and low dielectric and magnetic loss for frequencies greater than 2 GHz. Specific objectives were as follows: i) fabricate and characterize polymer composites with magnetic inclusions to understand how the loading affects the dielectric and magnetic properties, ii) investigate using alternative geometries and periodic metallic array layers using FEM solvers to calculate the reflection and transmission, iii) fabricate and characterize test coupons to validate designs.

1.2.2 Microwave Applicator Design

Activated carbon is often used as an adsorbent for applications involving fuel emissions control. The primary raw material for activated carbon would be any organic material with high carbon content (i.e. wood, coal, coconut shell). The activated carbon has a very large surface area per unit volume, and the material is very porous allowing adsorption to take place. In order to increase efficiency, companies have been motivated to develop methods to regenerate the activated carbon - i.e. thermal regeneration in vehicles [7-8]. In hybrid vehicles, however, the gasoline engine is not running for large

fractions of time; thus, alternative measures must be considered for the heating of the activated carbon.

Using microwave energy as an alternate method to regenerate activated carbon and similar adsorbents has been investigated with promising results [7-9]. Microwave heating is primarily accomplished by coupling electromagnetic fields into the material via ohmic loss. This loss is often characterized by temperature and frequency dependent dielectric properties. Microwave radiation allows for the carbon to be recycled and reused a number of times, resulting in an increased surface area and subsequently a higher value for the carbon as an adsorbent.

The efficiency of microwave heating is based upon the patterns of the electromagnetic field within the cavity. In single, or dominant, mode cavities, the cavity is specifically designed to support one resonant mode. Because single mode cavities are on the order of around one wavelength, they are often designed specifically for the object that is to be heated. In fact, generally, these cavities have one area, or "hot spot," where microwave field strength is high. Multi-mode cavities are capable of sustaining a number of high-order modes at the same time [10]. Some applications require heating and regenerating large volumes of carbon with lower power inputs; moreover, developing new microwave heating methods would be important for eliminating the problem of "hot spots" found often in microwave cavity heating. The specific objectives for this project include the following: i) dielectric characterization of activated carbon, ii) design and construction of microwave applicator to heat activated carbon, iii) temperature profile measurements to evaluate system performance, and iv) modeling of the microwave heating within the applicator using an energy balance.

CHAPTER 2 : Introduction to Electromagnetic Properties and Materials

2.1 Maxwell's Equations

The basic laws governing electromagnetic wave propagation are Maxwell's Equations [10], which describe the relations and variations of the electric and magnetic fields, charges, and currents associated with electromagnetic waves. Maxwell's Equations can be written in either differential or integral form. The time harmonic form, shown as follows, will be used for this work.

$$\nabla \times \mathbf{E} = -j\omega \mathbf{B} \tag{2.1}$$

$$\nabla \times \mathbf{H} = \mathbf{J} + j\omega \mathbf{D} \tag{2.2}$$

$$\nabla \cdot \mathbf{D} = \rho \tag{2.3}$$

$$\nabla \cdot \mathbf{B} = 0 \tag{2.4}$$

where **E** is the electric field intensity, **H** is the magnetic field intensity, **D** is the electric displacement density or electric flux density, **B** is the magnetic flux density, **J** is the electric current density, and ρ is the charge density. **D** is defined as:

$$\mathbf{D} = \varepsilon_0 \mathbf{E} + \mathbf{P} \tag{2.5}$$

where ε_0 is the dielectric constant of free space, P is the volume density of polarization, the measure of the density of electric dipoles. B can be expressed as:

$$\mathbf{B} = \mu_0 (\mathbf{H} + \mathbf{M}) \tag{2.6}$$

where μ_0 is the magnetic permeability of free space, H is the magnetic field intensity, and M is the volume density of magnetization, the measure of the density of magnetic dipoles in the material. In a simple isotropic medium, the field quantities are related as follows:

$$\mathbf{D} = \varepsilon \mathbf{E} \tag{2.7}$$

$$\mathbf{B} = \mu \mathbf{H} \tag{2.8}$$

where ε is the dielectric constant, and μ is the magnetic permeability. These constitutive relationships show how the material's properties affect the electromagnetic response to the applied field or source.

In addition to the Maxwell's Equations, the Equation of Continuity holds due to the conservation of electric charge:

$$\nabla \cdot \mathrm{J} + \mathrm{j}\omega \rho = 0 \tag{2.9}$$

In the Maxwell's Equations, only two are independent. Usually Equations 2.1 and 2.2 are used with Equation 2.9 to solve for electromagnetic fields. The material properties, ε and μ, dictate how the material responds to the fields and, thereby, how it will perform in specific applications; the two properties which will be used throughout both projects in this thesis are permittivity and permeability.

2.2 Electromagnetic Properties

2.2.1 Permittivity

Permittivity is a physical quantity that describes how an electric field affects and is affected by a dielectric medium and is determined by the ability of a material to polarize in response to an applied electric field, and thereby to cancel, partially, the field inside the material [10-11]. Hence, permittivity characterizes a material's response to an electric field. Going back to basic electromagnetics, one can define an electric displacement field **D**, which represents how an electric field **E** will influence the

organization of electrical charges in the system, including charge migration and electric dipole reorientation; this relationship is shown in the constitutive equation (Equation 2.7).

The complex permittivity can be represented by an imaginary and non-imaginary component as seen in the equation below,

$$\varepsilon = \varepsilon' - i\varepsilon'' \tag{2.10}$$

where ε' is the dielectric constant and ε'' is the dielectric loss factor. The dielectric constant actually depends on temperature and frequency (when not lossless), and the dielectric loss factor measures the material's ability to absorb and store energy [4].

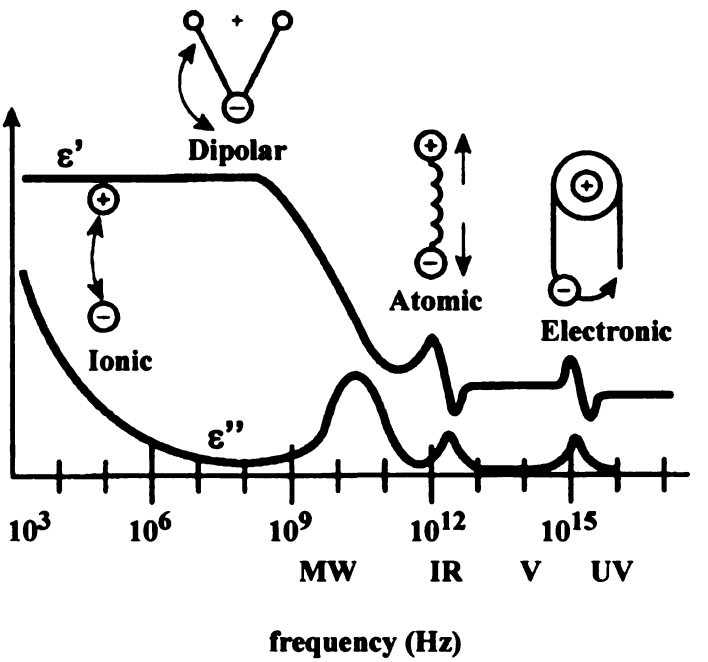

Figure 2.1. Permittivity vs. frequency (Hz) (adapted from [12]).

Figure 2.1 shows the dielectric properties as they are affected by frequency. Ionic conduction, dipolar relaxation, atomic polarization, and electronic polarization are the major mechanisms contributing to these effects on the permittivity. In the microwave region, the permittivity variation is mainly affected by dipolar relaxation. This is the region that is of importance for this research [10]. Further discussion of permittivity and the various polarization mechanisms can be found in Chapter 5, since these mechanisms are of significant importance for microwave applications.

2.2.2 Permeability

Permeability is the degree of magnetization of a material that responds to an applied magnetic field. Magnetic permeability is represented by the symbol μ. The complex permeability can be related to the magnetic field **H** and the magnetic displacement field **B** as shown in Equation 2.8. Similar to the complex permittivity, the complex permeability can also be represented by an imaginary and non-imaginary component:

$$\mu = \mu' - i\mu'' \tag{2.11}$$

where μ' is the permeability and μ'' is the magnetic loss factor [10-11].

The frequency dependence of magnetic materials is quite complicated and some underlying mechanisms are still not fully understood. Various physics phenomena dominate for the different frequency ranges. At very high frequencies, ferromagnetic resonance usually occurs. Magnetic effects can be the result of net nuclear spin, asymmetric electron orbital, and net electron spin [13]. Electrons have a spin-up or spin-down state, and an orbital is allowed to have only one of each spin state; if an orbital has

only one electron due to its spin, a net magnetic field will be produced. Also, the movement of the electron along its orbital can cause a net magnetic field; this behavior can be modeled as a magnetic moment. When the electron travels along the orbital, a current is produced due to the charge traveling in a loop, as shown by the "right hand rule." With more than one atom present, there can be coupling between different atoms, which makes predicting behavior more complex. Coupling that occurs between these atoms is due to their spins; these can be parallel or anti-parallel, resulting in a net magnetic moment or zero net magnetic moment, respectively [13].

In cases where the adjacent atoms have parallel moments, a domain with a net magnetization in the direction of the aligned moments is formed within the material. If the material is nonmagnetic, the domains are randomly aligned.

2.2.3 Homogenization and Effective Electromagnetic Properties

Throughout this work, two-phase composite materials were used, involving dielectric-dielectric and dielectric-magnetic mixtures. Since these materials are inhomogeneous, the permeability and permittivity throughout the material will vary. To represent these mixtures, homogenization of the composite is necessary to describe the material with an "effective" permeability and permittivity [14]. Examples of three different geometries are shown in Figure 2.3 – spheres, rods, and layers.

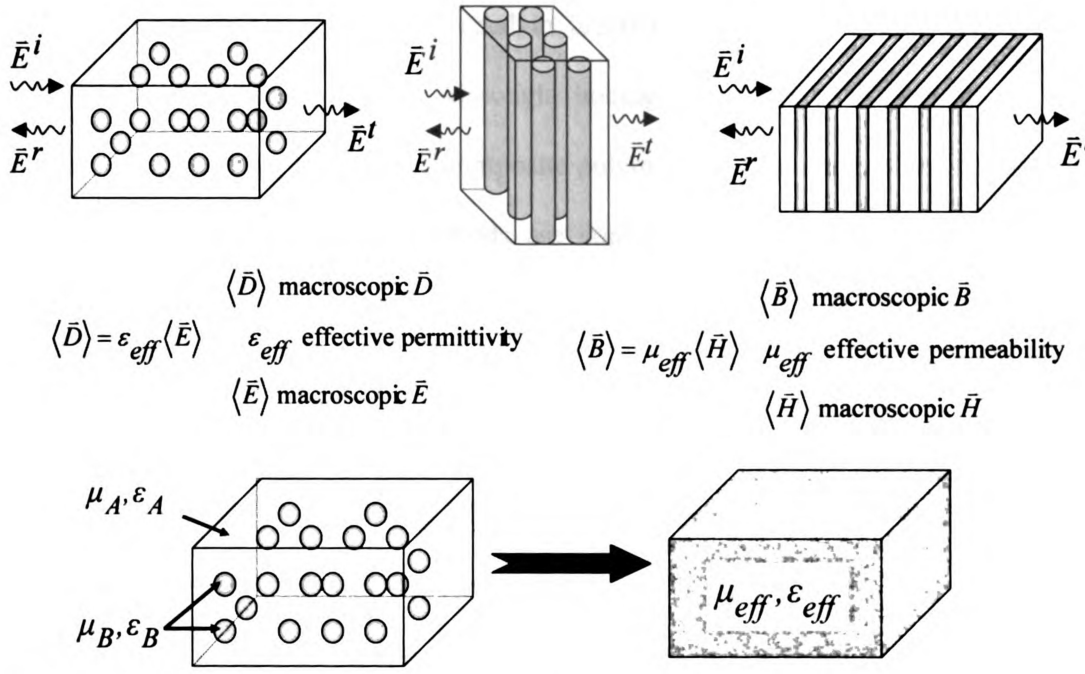

Figure 2.2. Homogenization and effective electromagnetic properties of composites.

As seen in Figure 2.2, to a wave, an inhomogeneous material can be homogenized so that to a wave, this material will have effective permittivity and permeability – ε_{eff} and μ_{eff}, respectively. This theory will be used for the majority of Chapter 4, where effective properties are extracted by using reflection and transmission coefficients and assuming the material is homogeneous.

2.3 Materials and Applications

2.3.1 Radio Frequency Materials

Homogeneous materials often used for microwave engineering applications include Teflon [15] and other polymers. Non-electrical properties, such as chemical resistance, thermal expansion, and thermal degradation often set a particular material

apart from others. Other materials used in practice are polyolefin (e.g. Tellite®) and polytetrafluoroethylene (PTFE). Although homogeneous materials are useful, the improved mechanical properties of composite polymers are important. Many commercial microwave-grade printed circuit boards are copper-clad laminates with a glass fiber reinforced polymer. For example, a material offered by Rogers is Teflon reinforced with glass microfibers [16]. This material is sold under the trade name, Duroid® and is in widespread use throughout the industry. Keene manufactures a material with woven glass reinforced Teflon [15]. Other materials are used in conjunction with glass reinforcement. For example, glass reinforced PTFE as well as homogeneous PTFE are commonly used materials by a number of manufacturers including Polyflon [15] and Arlon [18] among others. Cyan ester is used by Arlon and Allied Signal in some of their laminate products. Non-polymers, such as quartz, are also used in practice.

The above mentioned materials are generally stiff; however, flexible materials are also of great interest to the design community. For example, many conformal antennas rely on flexible materials. A common polymer for these applications is polyimide and a popular product by DuPont is sold under the trade name Kapton® [18]. Other vendors also sell flexible substrates, often also using Kapton. Rogers has published a good engineered materials selection document [19] useful for selecting the right material given desired properties. Flexible substrates have been achieved using other materials such as a thermoset polymer alloy (TPA). A summary web-site containing materials from a variety of sources is provided as a service by R&D Design [20].

2.3.2 Composites

More recently, work has been conducted to develop composites by tailoring shapes, composition, etc., in the hopes of correlating the size/shape with the effective magnetic permeability [21-23]. Likewise, work has also been dedicated to synthesis of conducting nanofibers and optimizing their properties [24-26]. Properties of interest are the electromagnetic response of materials at high frequencies. Several synthesis techniques exist and characterization of composites has been well studied [27-32].

In composites processing, properties which have been shown to undergo substantial improvements include the following: mechanical properties (strength and modulus), decreased permeability (barrier properties) to gases and water, thermal stability, flame retardancy, and electrical conductivity [27]. Polymer nanocomposites are constructed by achieving a stable dispersion of nanoparticles within the matrix, creating multiple layers which force gases and other materials to flow through the polymer in a "tortuous path" – hence improving the composite's barrier properties. Nano- and micro-sized reinforcements allow for lower loading levels than traditional fillers in order to achieve the optimum properties [27-28]. The permittivity reaches a maximum at certain volume fractions; hence, the percolation threshold is reached. For RF applications, however, higher loadings are required; yet nanocomposites offer better dispersive properties in these situations.

Mechanical properties are not the sole reason for using polymer composites for electromagnetic applications. The ability to tailor the bulk electric and magnetic properties of the material has important implications on RF design. Polymer composites, formed by mixing ceramic particles with a polymer base material, have been the subject

of considerable previous work [33-38]. Various mixing models exist for these systems [38-44]. Mixing models in common use include: Maxwell Garnett [38], Reynolds [39], Sihvola-Kong [38], Yamada [43] and Jayasundere [44]. These models are used for: spherical, arbitrary, ellipsoid, piezoceramic ellipsoid, and piezoceramic spherical inclusions, respectively. In addition to pure dielectric materials, mixing formula for magnetic materials have also been developed using the Clausius-Mosotti relation [45-46]. Previous work was dedicated to studying the classical mixing laws – Maxwell-Garnett, Bruggeman, and Coherent Potential – used to predict effective properties for the material. One important factor for calculating the effective permittivity of the material is the difference in the dielectric constant of the inclusion and matrix; for a small contrast, the mixing rules prove to be accurate. These mixing laws do not take into account particle-to-particle interaction; so as the volume fraction of inclusions increases, the formulas will not be very accurate for predicting the effective permittivity. In composites with a low volume fraction of inclusions and a small contrast in the dielectric constants for the two phases, the classical mixing laws can be used successfully for predicting effective permittivity.

However, attempts to use these mixing laws to predict permeability using the concept of duality between the electric and magnetic fields were unsuccessful and cannot be used as a tool for composite simulation and design. By duality, electrostatic and magnetostatic formulations can be said to obey the same conditions for a certain geometry (in this case, spheres) when subjected to the proper boundary conditions. Magnetism in itself is much more complex and the simple mixing laws do not account for this. Yet, some mixing laws work better for permeability predictions (Maxwell-

Garnet) since they focus more on the inclusions than the environment. These mixing laws are somewhat accurate for very low volume percents, when the material is barely (if at all) magnetic. When a magnetic inclusion is within a non-magnetic matrix, the inclusion has a larger effect on the permeability, and the particle to particle interaction must be handled more carefully; therefore, the homogenization approach of other mixing laws proves to be inaccurate. Overall, magnetic behavior of heterogeneous materials is not predicted well and the problem must be analyzed at the quantum level to yield a more precise model [46].

Materials selection will play a very large role in this project, since the final properties of the material are the primary focus. A ceramic (when a high dielectric constant or magnetic properties are desirable), a polymer (when low cost and/or flexibility is desired), or some polymer composite comprising a polymer matrix with suitable inclusions (typically glass fibers for strength) are typically used for RF materials.

2.3.3 Characterization Techniques

In the area of composites and materials research, fabrication and characterization are important to understand structure-property relationships which are essential for advanced materials design. The electromagnetic properties of these materials can be characterized with several techniques, including stripline applicators and waveguide applicators, use the measured guided wave transmission and reflection by a material sample before extracting effective ε and μ. Other measurement techniques, such as the free space arch range and the ASTM test cell can be used to directly measure the transmission and reflection properties of material samples. These properties can be

characterized as a function of frequency. For lower frequencies, 1MHz-1GHz, impedance analysis can be used with specific test fixtures can be used to measure capacitance or inductance through materials, to characterize ε and μ, respectively. Details of these characterization techniques as they apply to materials designed for this project will be discussed throughout this dissertation.

In addition to electromagnetic properties; tensile modulus, flexural modulus, impact strength, and toughness are often important material properties to characterize. Since thermosetting polymers will be used for fabrication, thermal analysis using differential scanning calorimetry (DSC) can be utilized to model the effects of reinforcement loading. This method is used to study thermal transitions in polymers such as glass transition, crystallization and melting. A sample pan and a reference pan are heated at the same rate, and the difference in heat flow between the pans is measured; this is plotted against temperature to determine the thermal transitions. For this work, DSC will be utilized to study the effects of particle loading on heats of reaction, cure initiation temperature, and cure peak temperature. To observe the dispersion quality of dopants or inclusions within the matrix, transmission electron microscopy (TEM) can be employed, after microtoming the samples and gold coating.

2.4 Electromagnetic Materials Design Challenges

2.4.1 Design Limits

Extensive efforts have been devoted to miniaturization of RF electronic systems and devices; however, there are still several challenges with materials design associated with creating power efficient antennas, filters, and other miniaturized electronic devices

[1-4]. Often, high dielectric, low loss materials are used to fabricate these components, resulting in high permittivity substrates that can have surface wave excitation, thereby leading to lower efficiency and pattern degradation, as well as difficulties in impedance matching. For example, antenna substrates have been reduced in size by using high permittivity materials, resulting in a highly concentrated field around the high permittivity region, which reduces the bandwidth and antenna efficiency. With increased impedance from the high permittivity, impedance matching becomes quite difficult [1].

This problem can be circumvented by designing magneto-dielectric materials, which are termed so due to their enhanced permittivity *and* permeability (both greater than one); however, these attempts are often limited by the physics of the materials. High permeability is difficult to achieve at high frequencies, without incurring loss. With these challenges in mind, the design of electromagnetic materials with improved properties has become an important area of research [1-6].

2.4.2 Metamaterials and Composites

Currently, there is much research dedicated to improving the electromagnetic properties of materials for a variety of applications beyond limits of conventional materials. Figure 2.3 illustrates several areas of research currently in electromagnetic materials – including left handed metamaterials, magneto-dielectrics, ferrites, and superconductors. The desired design space is shown in this figure, specifically highlighting magneto-dielectrics, with both permittivity and permeability increased.

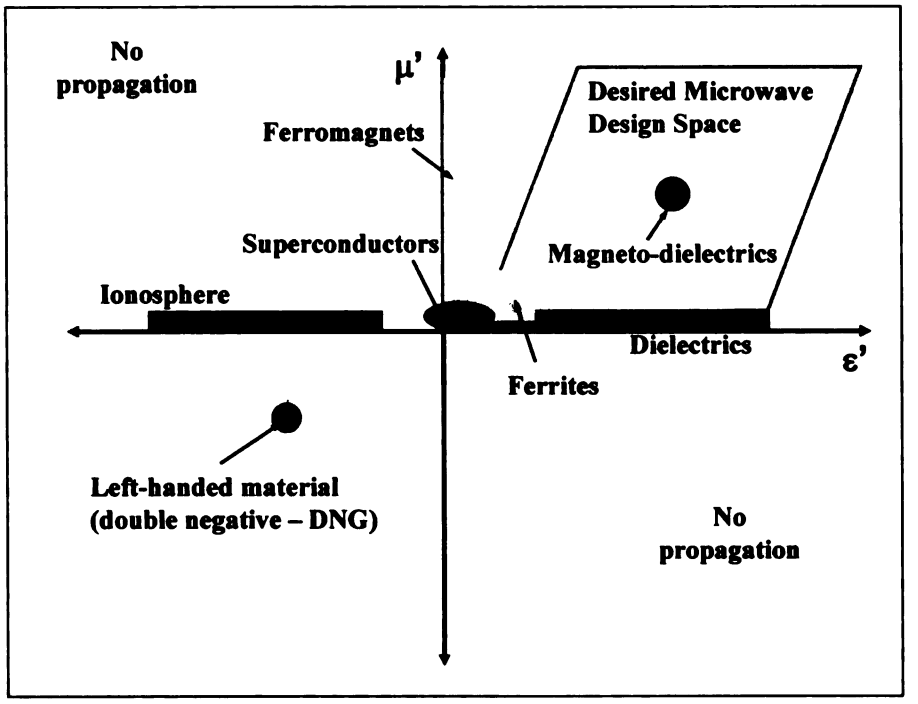

Figure 2.3. Electromagnetic materials designed.

As technology continues to improve and mature, it has become more challenging to satisfy the required material properties using conventional macroscopic composite materials. Metamaterials present a new class of composites that can be utilized to extend the capabilities of materials to meet requirements for the ever growing demand of new technologies and applications. The term "metamaterials" was first used by Prof. Rodger Walser of the University of Texas in Austin in 1999 and can be defined as macroscopic composites of periodic or non-periodic structure, designed to produce an optimized performance not available with natural material properties [48-49]. The dependence of metamaterials on their cellular architecture provides a great flexibility for controlling their properties. Three examples include chiral materials, left-handed materials, and photonic band-gap materials. Chiral materials have been given much attention due to

their potential for microwave applications – microwave absorbers, antennae, devices, etc. The introduction of chirality alters the scattering and absorption characteristics [48-49].

Macroscopic composites represent a highly researched branch of materials design and are often used for developing improved materials for a wide variety of applications. The design rules for these materials abide by the idea that the composite material properties are derived from the law of mixtures.

2.4.3 Previous Work

There has been significant work towards improving materials that are often limited by some of the challenges discussed previously. For example, the high permittivity materials which suffer from reduced bandwidth and efficiency have been improved by reducing the effective dielectric constant via perforations of the substrate or texturing of the dielectric substrate [1-4, 50-56]. Other work has involved creating materials of similar performance using complex systems of ceramic ferrites or artificial magnetic materials. However, these materials, albeit possessing an enhanced bandwidth, are still limited by difficult impedance matching.

Ferromagnetic inclusions within a polymeric host matrix have been the subject of subsequent research; besides an improved permittivity and permeability, these materials have a modified strength and stiffness as well as improved electrical and thermal conductivity. Such properties can be tuned based on the properties of the components and shape or orientation of the filler [4-5]. Although effective permittivity and permeability can be controlled for these materials, the bandwidth of performance is for frequencies lower than 1 GHz, due to the fact that magnetic materials are often non-

magnetic (μ=1) and lossy for higher frequencies. This increased loss is due to eddy currents in these materials and presents a significant problem [4-5].

2.5 Objectives and Future Impact

The objective of this project was to achieve the ability to tailor the material properties based on the application. These designs need to have the wide-range capabilities to be used for different applications; most important is to develop a methodology that will be flexible to the changing technologies and applications.

Potential applications and devices associated with these novel materials would include components for wireless devices (i.e. circulators and isolators), sensors, or even devices for energy transport – like, for example, wide angle impedance matching (WAIM) stacks often used as radomes. Reflection is dependent on the impedance mismatch between the material and free space. For normally incident waves, reflection is zero for cases when $\mu = \varepsilon$; but for non-normal incidence, reflection is governed by the product of μ and ε. For the largest possible scan volume, the product should be as close to unity as possible. The material designs for this work would have relative permeability (μ) very close to ε (around 2), which would result in the optimum scan volume.

To overcome the limits in bandwidth *and* impedance matching, an alternative approach presented here would be to design magneto-dielectric composites with and enhanced *and* balanced combination of μ and ε. In this way, the more moderate impedance can allow for easier impedance matching. Therefore, the objective of this work can be defined as follows: to design a material with permeability greater than unity,

a permittivity that is not much greater (and preferably smaller) than permeability, with low loss at frequencies greater than 1GHz.

Two approaches were utilized to reach the objective. Chapter 3 of this dissertation will describe the initial approach to the solution, by using conventional macroscopic composites; however, the performance of these materials was limited by the underlying physics, which prompted a new, revised approach. Chapter 4 outlines this new approach using periodic arrays of metallic structures layered within a polymer to create a metamaterial composite capable of meeting the original objective. Structure-property relationships will be developed to understand the sensitivities of material geometries for both approaches. The desired outcome of this work would be to develop designs that offer wide flexibility for the engineer.

CHAPTER 3 : Inclusions-based Magneto-dielectric Composites

3.1 Approach

The goal of this work was to develop broadband, low loss magneto-dielectric with non-trivial relative permeability ($\mu_r \geq 2$); a relative permittivity that is not much larger, and preferably smaller, than the permeability; and very low loss. To meet this design goal, the approach was formulated to include three major aspects of work: materials selection, simulations and modeling, and fabrication with characterization.

The overall approach followed the theme shown in Figure 3.1. The three branches of work formed a continuous cycle – first the selection of materials or geometries, secondly the modeling of the composite to predict the final properties, and lastly the fabrication and characterization of test coupons to validate the design. Based on the results from the characterization, the materials and geometry may be revised; therefore, the approach is a constant cycle of experimentation, modeling, and characterization.

The preliminary approach to meeting the design goal was to use polymer nanocomposites with ferrimagnetic inclusions, in hopes that simply mixing high permeability reinforcement material into the polymer would enhance the properties to the desired extent. Specifically, this initial work involved synthesis of iron oxide composites, the primary focus being to examine the effects of the inclusions on the overall properties for the composite.

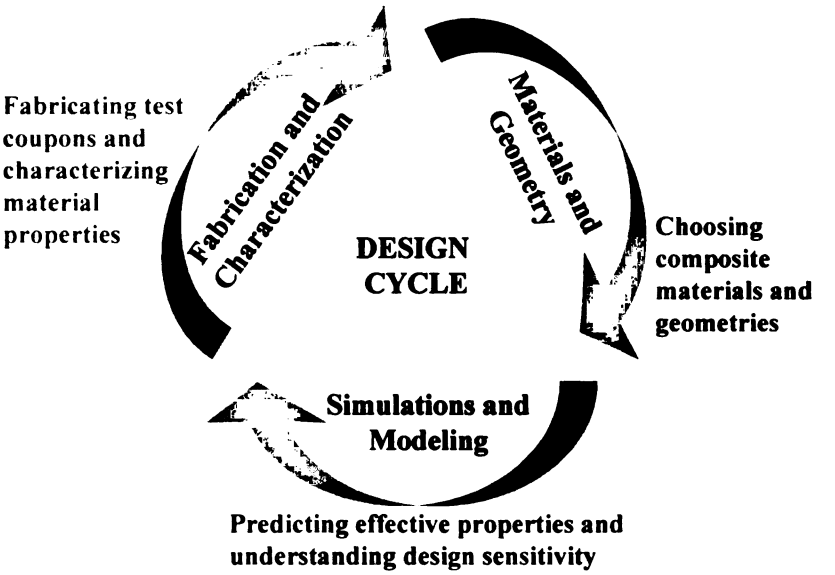

Figure 3.1. Design cycle approach – material choice, simulations/modeling, experimental validation.

For the initial inclusions-based composites, various weight percent of appropriately chosen reinforcement material were added to an epoxy matrix. The material properties were characterized depending on the sample type, to measure ε and μ; a waveguide would be used to measure reflection and transmission for higher frequencies, while an impedance analyzer would be used to directly measure ε and μ for lower frequencies (less than 1 GHz). In addition to electromagnetic properties, DSC was used to model the effects of extent of cure on the electromagnetic performance of the composite. Because thermosetting polymer was used as the matrix, the inclusions/dopants affect the cure characteristics; DSC was utilized to study the effects of particle loading on heats of reaction, cure initiation temperature, and cure peak temperature. To observe the dispersion quality of dopants or inclusions within the

matrix, transmission electron microscopy (TEM) was employed, after microtoming the samples and gold coating.

3.2 Experimental Methods

3.2.1 Choice of Materials

Magnetic materials can be divided into two major categories: paramagnetic and diamagnetic materials. Diamagnetic materials have a relative permeability less than 1; in the absence of an applied field, the orbital and moments cancel, leaving the atoms with no net magnetic moment. Paramagnetic materials have net moments that align with the applied field and are divided into three categories – ferromagnetic, antiferromagnetic and ferrimagnetic materials.

For a ferrite like iron oxide, for example, the spin moments of the eight Fe^{3+} atoms at the two sites are opposite and cancel, so that the eight Fe^{2+} atoms will determine the overall magnetism. Such an arrangement is characteristic of a ferrimagnetic material; while ferromagnetic materials – like nickel and iron – have all the dipoles aligned to create the net magnetism, antiferromagnetic materials have the dipoles arranged in such a way that all the charges cancel (see Figure 3.2). Above a certain temperature – the Curie temperature – thermal agitation is sufficient enough to overcome the coupling, and ferromagnetism can disappear [57].

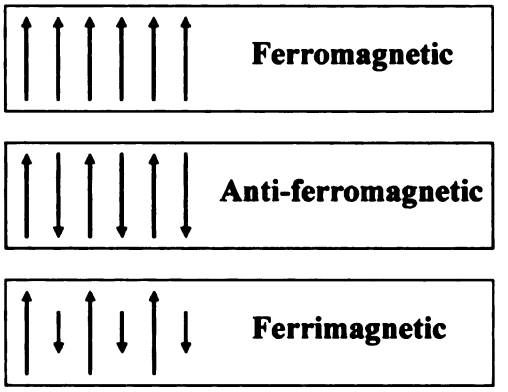

Figure 3.2. Comparison of magnetic materials dipole arrangement.

When considering choice materials for the reinforcement material for these composites, a ferrimagnetic material would be ideal. Metal oxides would be preferred due to the lower conductivity – resulting in no eddy currents and thereby, lower magnetic loss. Ferrites are essentially mixed crystals of various metallic oxides and consist of oxygen ions in a closely packed structure with cations fit into the spaces [57]. Ideally, ferrites are non-conductors, and hence the power loss is low at high frequencies. The ability to maintain magnetic properties at high frequencies with low loss is a major benefit for using these materials.

3.2.2 Composite Synthesis

Several synthesis techniques exist, and characterization of nanocomposites has been well studied [28-32, 58]. Diglycidyl ether of bisphenol-F (DGEBF), supplied by Dow, was cured with diaminodiphenyl sulfone (DDS), supplied by TCI America, as the curing agent. The weight percent of the filler was varied from 5 to 40 weight percent. Iron oxide nanopowder of spherical morphology, supplied by Nanostructured and

Amorphous Materials, Inc., was selected as the filler. The average size of the nanoparticles was around 30 nm.

Surface treatments used to improve the dispersive quality of the metal oxide nanoparticles include oleic acid as well as silane coupling agent. There are two major challenges with surface treatments: (i) the inclusions have to be surface-functionalized in such a way that a linkage between the inorganic inclusion and the organic matrix is stably established and (ii) the surface-functionalized inclusions should be homogeneously dispersed into the organic matrix [27-29]. The iron oxide nanopowder in this study was treated using a 1% solution of Glycidoxypropyltrimethoxysilane (epoxy functional Z-6040 silane from Dow). It was later found that silane treatment for high weight percent loadings (past 10%) were not effective, as fine dispersion is not attainable at high loadings. Sedimentation occurs because the density of the iron oxide is so much higher than the epoxy matrix; such a problem has been noted in other aspects of composite processing [31].

The iron oxide nanopowder was dispersed in the epoxy using ultrasonication and the curing agent was added by a stoichiometric ratio. The composites were cured in an oven for 2 hours at 146°C. Different shaped samples (required for electromagnetic characterization) were achieved by properly shaped molds made of Teflon or silicone; the electromagnetic characterization requirements will be discussed in the following section.

3.3 Characterization

3.3.1 Dispersion Quality

To improve the dispersion of the iron oxide, surface modification was employed to treat the iron oxide. The iron oxide was treated with the epoxy functional silane (Z-6040 silane, Dow) with two different techniques – one of these techniques involved several rounds of washing the nanoparticles after treatment. In general, the role of surface treatment agents is to increase the hydrophobicity of iron oxide particles and their adhesion to the polymer matrix. Furthermore, the steric stabilization of these surface modifiers also provides entropic repulsion necessary for overcoming the short-range van der Waals attraction that would otherwise cause irreversible particle aggregation [58]. Fourier transform infrared spectroscopy (FTIR) was used to characterize the effect of the surface modification (Figure 3.3). The transmittance was measured with wavelength for the powder directly, without making KBr pellets. Some adsorption peaks of C–H stretching vibration between 3300 and 3200 cm^{-1} and carbonyl absorption peaks around 1650 cm^{-1} were found that were not present in iron oxide, indicating that the modifiers were possibly absorbed on the surface of the iron oxide [58]. Additional analysis with other characterization techniques could be used to further verify that the silane coated the nanoparticles.

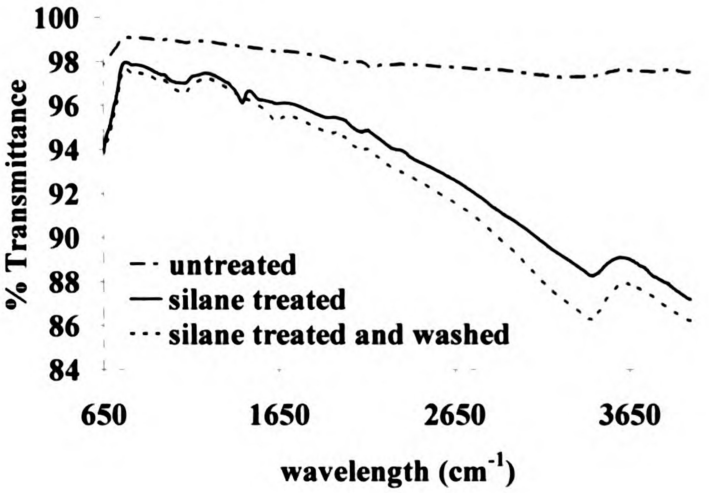

Figure 3.3. FTIR results for Fe_3O_4 nanopowder – surface treatment analysis.

Figure 3.4 shows the TEM image of a microtomed sample of a 10wt% iron oxide composite. The iron oxide was dispersed in clumps for the higher weight percent loadings, as sedimentation occurred for these mixtures due to the large difference in density between the reinforcement material and the matrix.

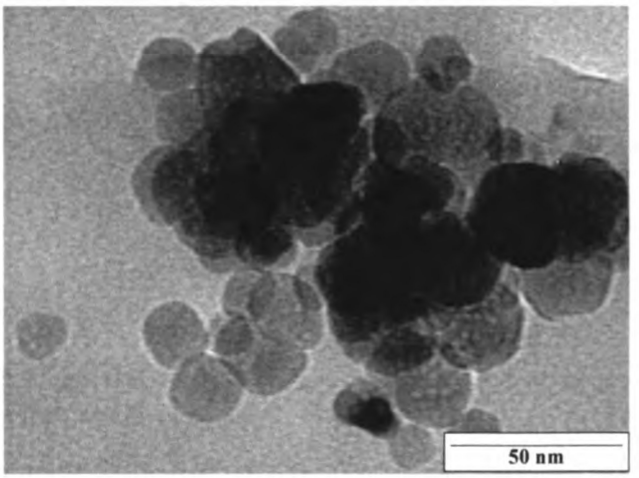

Figure 3.4. TEM image of 10wt% iron oxide nanocomposite

3.3.2 Effective Permittivity and Permeability

An HP Agilent E4991A Impedance Analyzer was used to characterize the electromagnetic properties of the materials. The 16453A Dielectric Text Fixture was employed to measure the effective permittivity [59]. The dielectric test fixture measures the admittance of the sample while held between two electrodes within the fixture as seen in Figure 3.5 from 1MHz to 1GHz. The conductance (related to the dielectric loss) and the capacitance between the electrodes are measured, and the real and imaginary parts of the permittivity can then be calculated, using these measured values.

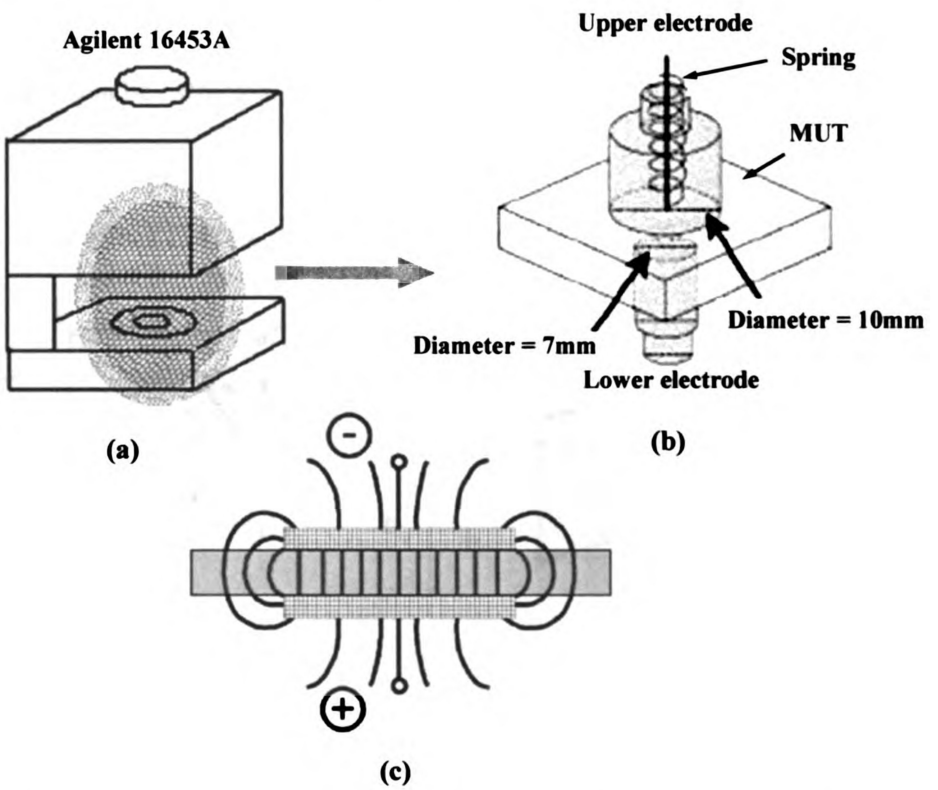

Figure 3.5. Dielectric test fixture for characterization. (a) Agilent 16453A Dielectric test fixture, (b) Test fixture electrodes, and (c) Electric field lines between electrodes (edited from [59]).

Similarly, the 16454A Magnetic Test Fixture can be employed to measure the effective permeability. This test fixture measures the inductance in a toroidal shaped sample as seen in Figure 3.7 from 1MHz to 1GHz. As shown in Figure 3.7, h_0 is the height of the fixture, a is the diameter of the inner conductor, and e is the diameter of the fixture. The measurements b and c represent the inner and outer radii of the sample. The inductance is created from current flowing upwards through the center conductor and then outward and down the walls of the fixture. A magnetic flux is generated by this current and is in the direction normal to the surface created by that loop. The inductance is measured, and the complex impedance is calculated; from the complex impedance, the complex permeability can be extracted.

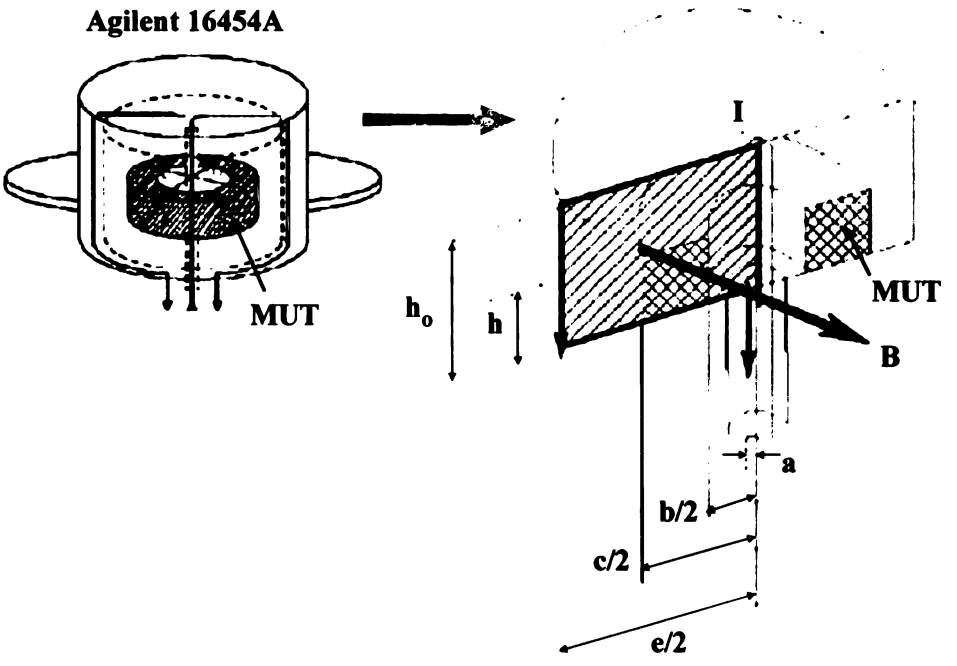

Figure 3.6. Magnetic test fixture for characterization. *Left*: Agilent 16454A Magnetic test fixture and *Right*: Current flowing through the sample within the test fixture (edited from [59]).

The electromagnetic properties were measured over a frequency range from 1MHz to 1GHz for the iron oxide nanocomposites (as a function of weight percent iron oxide).

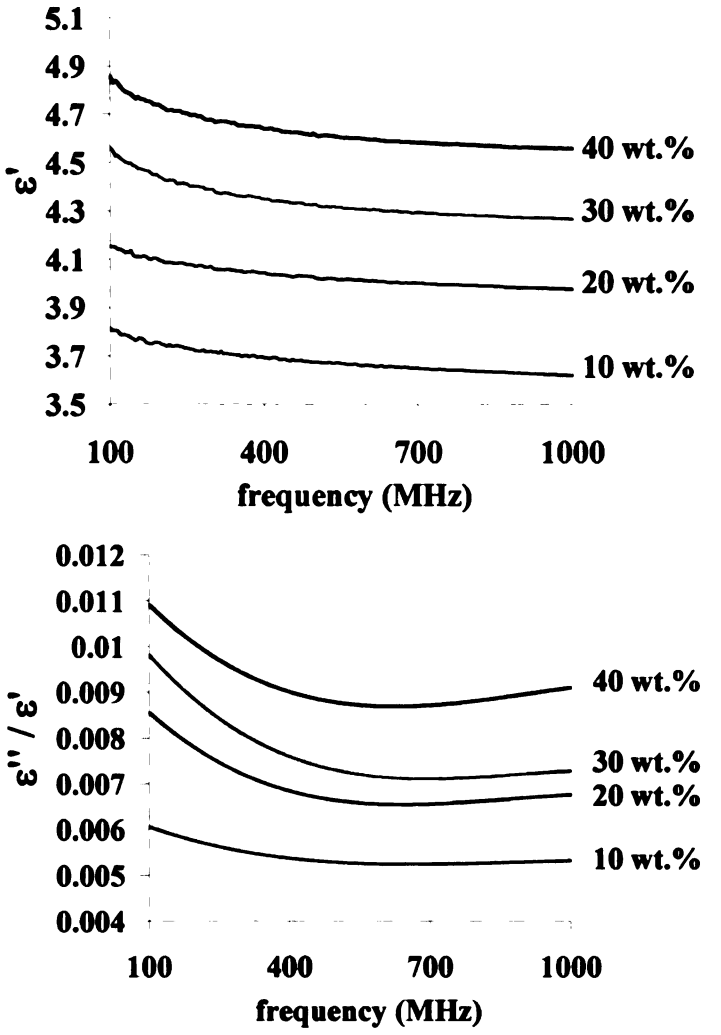

Figure 3.7. Dielectric characteristics for iron oxide nanocomposites. *Top*: Dielectric constant, ε', vs. frequency (MHz) for varied wt. percent iron oxide and *Bottom*: Dielectric loss tangent, ε''/ε', vs. frequency (MHz) for varying wt. percent iron oxide.

As seen in Figure 3.7, the dielectric constant increased with higher loadings of the inclusion material. The permittivity (ε') remained relatively constant with frequency – due to the low loss of the material. The loss tangent (the ratio of the imaginary and real

parts of the permittivity) remained at or below 0.01, indicating the material is reasonably lossless. Similarly, an analysis was performed for the permeability (Figure 3.8). The same trends were noted for the magnetic properties of the material.

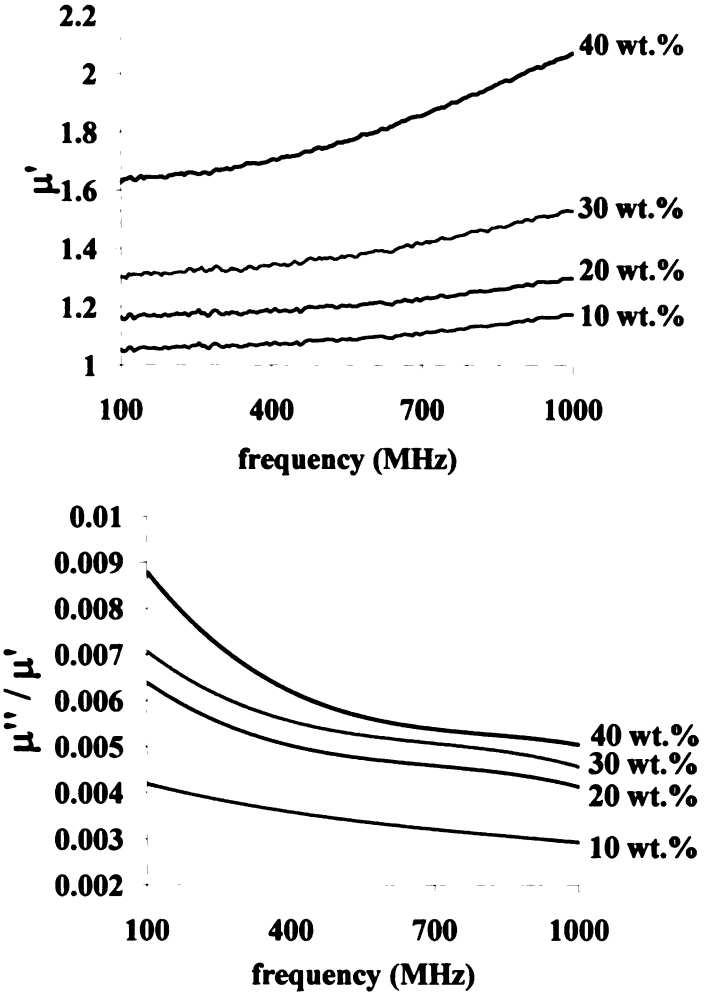

Figure 3.8. Magnetic characteristics for iron oxide nanocomposites. *Top*: Permeability, μ', vs. frequency (MHz) for varied wt. percent iron oxide and *Bottom*: Magnetic loss tangent, μ''/μ', vs. frequency (MHz) for varying wt. percent iron oxide.

When analyzing the electric and magnetic characteristics of the material, it would be expected that both permittivity and permeability increase as the amount of iron oxide increased. Figures 3.7 and 3.8 show this trend, although the permeability does not

increase as much as permittivity. This shows that simple mixing of randomly distributed particles will not increase the magnetic properties to the extent necessary (while still having low loss). The random distribution of spheres will not result in a net magnetization because there is no alignment in the dipoles. External biasing, as well as non-spherical inclusions, would be necessary to increase the permeability significantly.

The material should be relatively lossless for RF applications. The loss tangent of the permeability and permittivity are both below 0.01. In addition, the permittivity and permeability are relatively constant with frequency. These results lead to the conclusion that the materials are relatively lossless.

The permittivity and permeability are also affected by the temperature as well as extent of cure. A low-power swept-frequency diagnostic system (details of the experimental equipment can be found in literature [60]) was used to measure the shift frequency and half-power bandwidth for heated samples at different extents of cure. Each sample was cured for varying time periods, and these measurements were taken during free convective cooling of the samples. Inversion methods were used to convert these measurements to the dielectric constant and loss factor. Figure 3.9 illustrates the observed trends for temperature effects on the dielectric constant and loss tangent, respectively at 2.45 GHz.

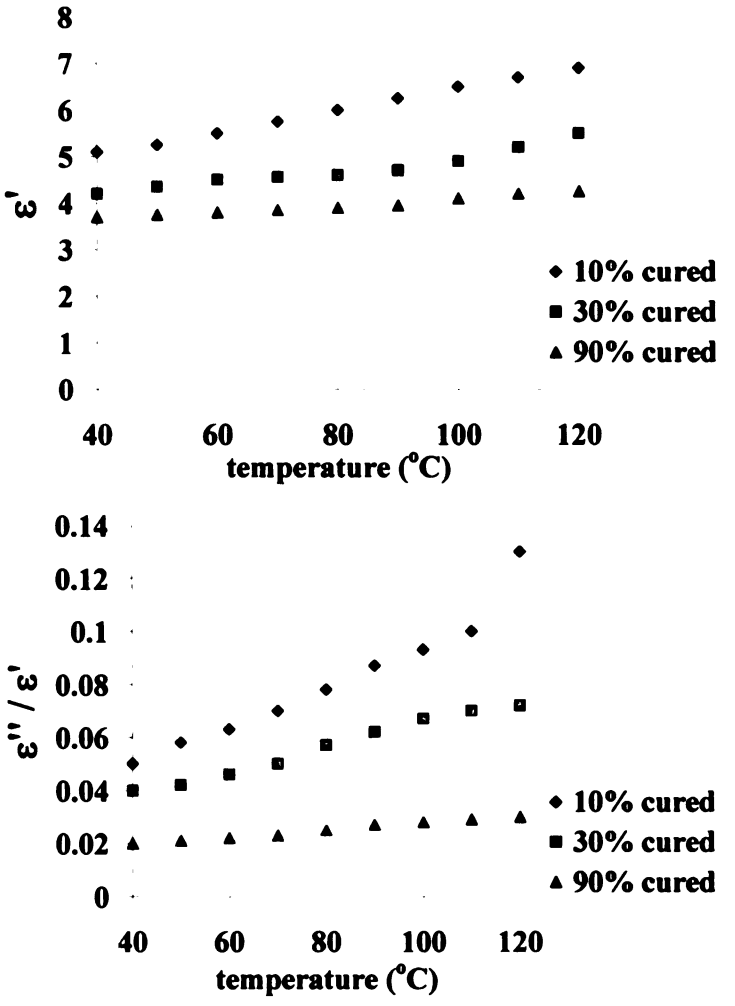

Figure 3.9. Effects of temperature and cure time on the dielectric properties for iron oxide nanocomposites (5 wt.% Fe_3O_4). *Top*: Dielectric constant, ε', vs. temperature (°C) and *Bottom*: Dielectric loss tangent, ε''/ε', vs. temperature (°C) for varying cure %.

Initial results indicated that the dielectric properties increased with temperature and decreased with extent of cure – a trend that can be related to the fact that the dipolar groups in the reactants decrease in number during the curing process, while the viscosity increases. Although the dielectric properties at the high temperatures are high as desired,

the loss tangent would be too high. The material is more lossy for lower extents of cure and higher temperatures.

3.3.3 Thermal Analysis

The effects of the iron oxide on the cure reaction were analyzed with the DSC (Figure 3.10). DSC was run on the resin suspensions with the iron oxide nanopowder, with loading varying from 0 to 8 weight percent. The temperature was ramped from room temperature to 300 °C at varied heating rates.

The heat of reaction decreased with increased loading of iron oxide, a trend that can be attributed to the decreased content of epoxy in the samples. The peak cure temperature increased with higher loadings of iron oxide, perhaps because the nanoparticles accelerate the cure reaction. The heating is more local when there are more iron oxide nanoparticles, hence leading to a lower peak cure temperature.

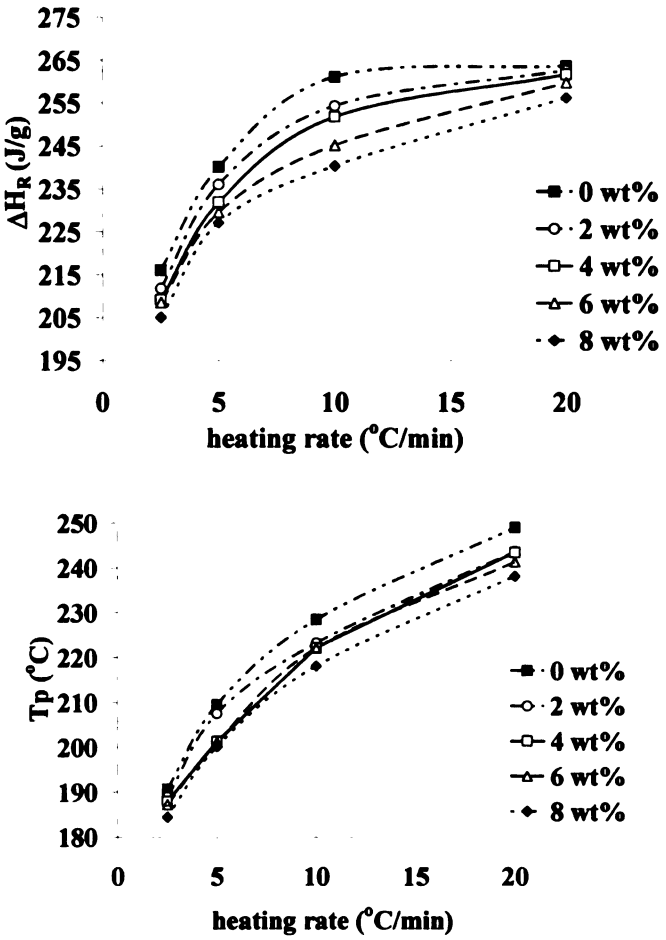

Figure 3.10. Thermal analysis of iron oxide nanocomposites. (a) Heat of reaction (J/g) vs. heating rate (°C/min) and (b) Cure peak temperature (°C) vs. heating rate (°C/min) for varied particle loadings.

3.4 Related Simulations

Simulation and modeling work related to the experimental work discussed in this chapter were conducted [61], in order to develop mixing models for extracting effective medium properties for magneto-dielectric composites [61]. The numerical approach involved computing reflection and transmission and using algorithms for extracting

effective permittivity and permeability. Two cases from this study are shown here – (i) a composite comprised of a set of layers and (ii) a composite comprised of cylindrical rods (Figure 3.12 and 3.13).

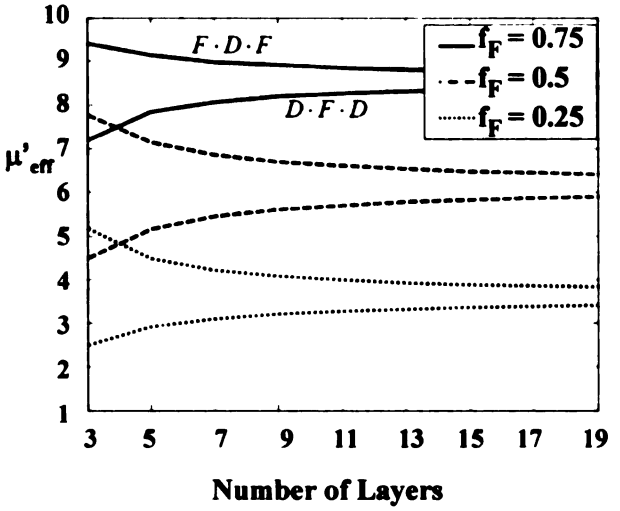

Figure 3.11. Predicted permeability for composites comprised of infinite yttrium iron garnet (YIG) layers in a Teflon matrix. Effective permeability for composites comprising of alternate layers of YIG (F) and Teflon (D) [61].

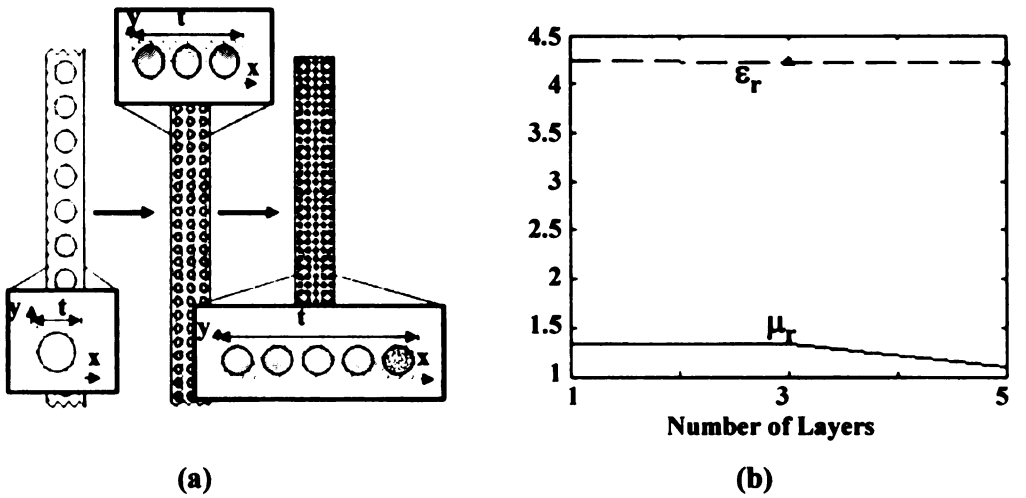

Figure 3.12. Predicted permittivity and permeability for composites comprised of yttrium iron garnet (YIG) rods in a Teflon matrix. (a) Periodic configuration analyzed and (b) Effective relative permittivity and permeability as a function of the number of cylinder layers [61].

As illustrated in Figure 3.11, both permittivity and permeability were enhanced with the infinite YIG layers for large volume percents of YIG. However, the studies on two-dimensional YIG cylinders that were arranged in a periodic lattice led to different conclusions. By comparison, the response from the geometry in Figure 3.12 – scattering from a finite slab comprised of the cylinders of YIG that are repeated in a periodic manner – was not as promising as Figure 3.11, since the permeability did not increase to the same extent as permittivity increased.

The results from simulations and experimental work have lead to similar conclusions – simple mixing of the samples did not appear to be a successful approach to achieving the desired final properties.

3.5 Conclusions

Both preliminary experimental work and related simulations and modeling [61] resulted in similar conclusions that simply relying on the incorporation of ferrimagnetic inclusions into a polymer or dielectric substrate would not sufficiently enhance the composite's effective properties. The experimental work focused on iron oxide nanocomposites showed that in order to achieve the desired magnetic properties, the volume fraction required would have to be 40% or higher. This behavior can be attributed to the geometry of the inclusions, which does not allow for a large magnetization in the composite; therefore, the permeability is near unity and the material is non-magnetic. Moreover, the spherical ferrimagnetic particles used in this study have a demagnetization factor of 1/3, meaning that they must be very tightly packed in order to result in a significant increase in permeability. Not only would very high volume

fractions result in brittle composites with magnetic particles that would be very difficult to disperse, but the weight of this composite would become not much less than using the ferrite in bulk. Also, for these composites with tightly packed (high volume fraction) inclusions and great contrast in the dielectric constant for the two phases, predictions using the classical mixing laws would not be accurate.

This initial experimental work prompted the need to approach the problem differently. Chapter 4 will highlight the secondary approach to designing the magneto-dielectric composites utilizing the idea of periodic arrays of metallic patches, which can be designed to act as "inductive" inclusions, thereby enhancing the properties for the material.

CHAPTER 4 : Composites with Frequency Selective Surface Layers

Previous results – both modeling and experimental – prompted a methodology shift in terms of how to design magneto-dielectric materials, if robust performance is to be expected at higher frequencies. Simple composites with magnetic reinforcement materials, a common approach, proved to be unsuccessful, as noted in previous work. An alternative approach was pursued, where a polymer matrix would be layered with periodically distributed shapes, or frequency selective surfaces. By designing these periodic arrays to act as "inductive inclusions," a low mass density material with controlled loss and enhanced permeability over a specific range of frequencies was successfully designed.

4.1 What is a Frequency Selective Surface (FSS)?

4.1.1 FSS Definition

A frequency selective surface (FSS), or spatial filter, is formed by arrays (often periodic due to simpler manufacturability) of metallic elements atop a substrate (a polymer or other dielectric material). The frequency-filtering property of the FSS comes from the planar periodic structure; the elements reflect the incident microwave for a specific frequency range. This property is dependent on the element shapes, periodicity, and dielectric property of the substrate. The periodic surface is composed of identical elements which are arranged in a 1D or 2D array. This periodic array can be excited by an incident plane wave or by individual generators connected to each element. The design of the frequency selective surface is highly dependent on the desired reflection

and transmission characteristics as well as the desired bandwidth for varying angle of incidence [62-63].

Figure 4.1 shows the design concept for these composites where the surfaces at the layer interfaces are composed of periodic metallic elements. An incident wave to these layers will cause an induced current in each element, which will act as capacitors or inductors (depending on their shape). These currents result in a scattered field. Therefore, since the properties of the composite are dependent on these elements, the design of the frequency selective surface is ultimately dependent on the desired reflection and transmission characteristics as well as the desired bandwidth.

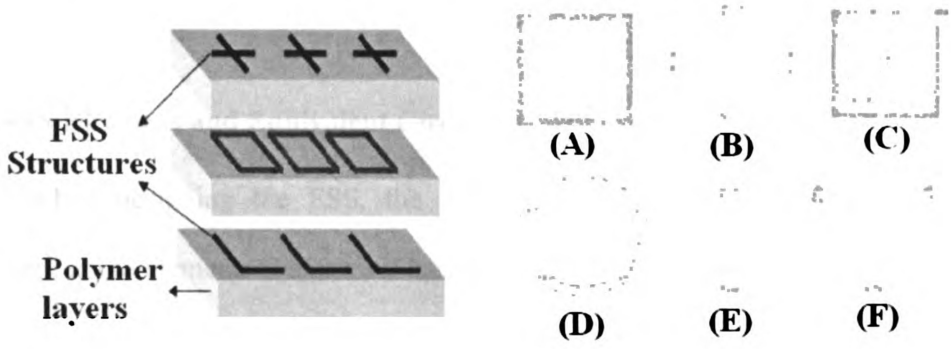

Figure 4.1. Conceptual design for composites with frequency selective surface layers. Layers are composed of periodic elements as shown on the right: (A) square loop, (B) cross, (C) spiral, (D) circular loop, (E) dipole, (F) three legged cross. The layers are located at the interfaces between the polymer layers.

Due to the intricacy in the existing frequency selective surface designs – their dimensions, sensitivity to angle of incidence, and operational bandwidth – these materials are often limited in their functionality; in this regard, there is a growing demand to improve their performance.

4.1.2 FSS Applications

When exposed to the electromagnetic radiation, an FSS acts just like a filtering material allowing some frequency bands to be transmitted while allowing others to be reflected. In fact, a common application for FSS structures is for use in radomes, which are often used to reduce radar cross section of an antenna system for frequencies that remain outside the bandwidth of operational frequencies, an application which has great potential for military use and stealth technologies [62-63]. In addition to radomes and band-stop filters, FSS structures and materials can be used as dichroic sub-reflectors and main reflectors or even absorbers [64-68].

4.2 FSS Elements and Equivalent Circuit Theory

When designing the FSS, the proper choice of element may be the most important; some elements are narrow banded, while others have the ability to be varied by the design. The polymer layers between the FSS layer(s) will have a great effect on the FSS performance, specifically with the bandwidth variation with angle of incidence. The element spacing will also affect the bandwidth and performance of the composite.

The operational mechanisms for conventional FSSs can be explained by resonance; for instance, a periodic array of metal patches, when in contact with a plane wave, will resonate at frequencies where the length of the elements is a multiple of the resonant length $\lambda/2$. Because each of these elements has a phase delay, the scattered fields from the individual elements add up. A major issue with FSS designs is the strong dependence of the frequency response with respect to element dimensions and angle of incidence of the wave [54-56, 62-63].

Three major categories of FSS arrangements are shown below in Figure 4.2: 1) the center connected or N-poles – i.e. dipoles, three legged elements, spirals, and Jerusalem crosses, 2) the loop types – i.e. square loops, three and four legged loaded elements, circular loops, and hexagonal loops, and 3) solid interior or plates. Additionally, a combination of any of these types can be used, resulting in infinite possibilities for FSS elements. Munk has outlined simulation results for FSS geometries from each of these categories, evaluating the strengths and weaknesses of each shape for specific applications [62].

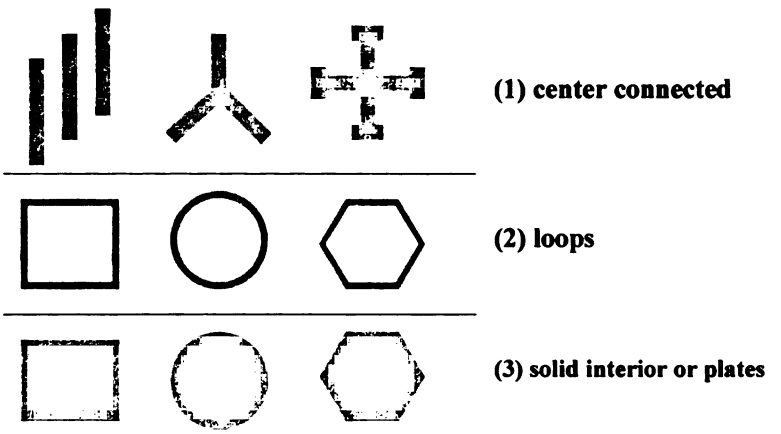

Figure 4.2. Typical FSS element types shown by groups: (1) center-connected or N-poles – dipoles, three-legged element, and Jerusalem cross, (2) loops – square, circular, and hexagonal, and (3) solid interior or plates – square, circular, and hexagonal.

FSS elements generally fall into two groups: patch-type and aperture-type elements. Figure 4.3 below shows complementary FSS arrays – patch and aperture type elements. The patch elements in Figure 4.3 (a), when excited by a plane wave, will transmit the wave at low frequencies and reflect the wave at higher frequencies, thereby a capacitive response. The complementary aperture-type element FSS array instead shows an inductive response as a high-frequency filter.

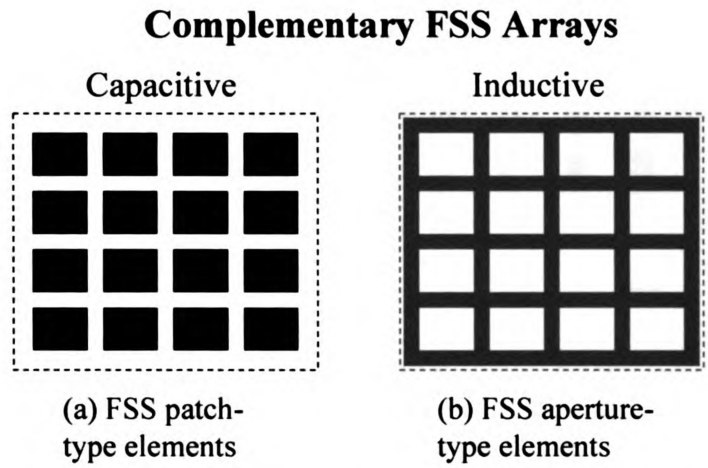

Figure 4.3. Complementary FSS arrays: (a) patch-type elements result in a capacitive response and (b) aperture-type elements result in an inductive response.

This highlights just one aspect of the flexibility of using this approach for magneto-dielectric materials design, as both inductive and capacitive structures can be used together to create the specific transmission or reflection corresponding to the specific electromagnetic properties.

In general, to predict how an FSS will perform, an equivalent circuit model is often used. For example, consider the following two FSS geometries: a periodic surface of infinitely long metallic strips and a periodic surface of finite length metallic dipoles (Figure 4.4). While the long metallic strips are inductors, the finite length strips have a series of capacitances associated with the gaps between the elements, resulting in the equivalent circuit of a series LC circuit as shown [62-63].

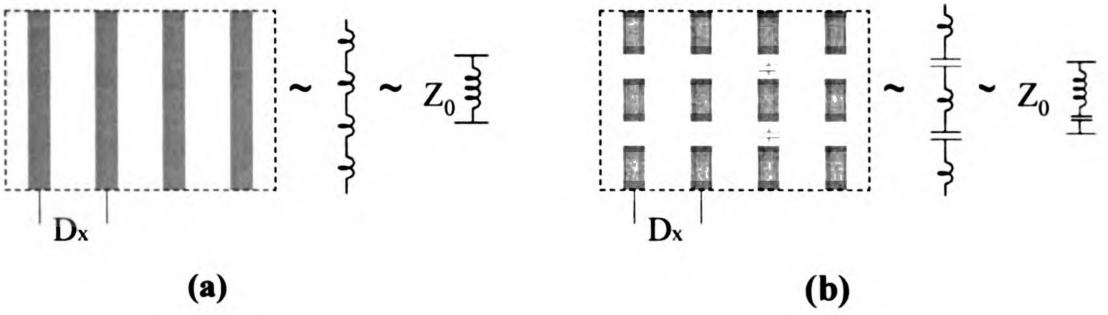

Figure 4.4. Equivalent circuit theory applied to FSS arrays. (a): Periodic FSS geometry of infinite metallic strips with the corresponding equivalent circuit. (b): Periodic FSS geometry of finite metallic strips with the corresponding circuit.

4.3 FSS Design Approach

Several parameters and their effect on the overall characteristics are not well understood; some of these being the pattern, the thickness of the layers, the polymer in between the metallic layers, the means to construct circuit elements, etc. Although this type of composite would be frequency sensitive, its bandwidth can be widened by manipulating the dipole size and separation. This represents another aspect of the design flexibility of this methodology. The approach to designing the composites included two parts – 1) appropriate choice of FSS element and substrate properties and 2) simulation of the FSS composite. After the preliminary designs were chosen, fabrication of the composite was necessary to characterize and validate the response.

4.3.1 FSS Element Design

The element shape and dimension has the most significant effect in the response; however, the way the elements are arranged as well as the characteristics of the substrate are major parts of the design work. For the results presented in this work, square loops

and hexagonal loops (Figure 4.2 – group 2) were chosen as the FSS elements as they will create an inductive response – thereby increasing the magnetic permeability. Elements were designed to be much smaller than a wavelength to create capacitive gaps and inductive traces; moreover, the inductive traces could be spaced closely together to create a larger mutual magnetic coupling, and hence a more enhanced inductive effect – higher permeability.

4.3.2 Transmission and Reflection Characteristics

The effects of variation in FSS element shape, size, periodicity, and polymer layer characteristics on the resulting properties of interest – permittivity and permeability – were the primary focus of initial simulations. Since well-developed mixing laws cannot e used for predictions of these composite properties, alternative full-wave simulations were necessary. Ansoft Designer and Ansoft HFSS were software used for simulation of the composite geometries. These software packages use method of moments and finite element methods, respectively, to solve electromagnetics problems; the geometries for the composites are meshed adaptively for a range of frequencies. Since the size of the unit cell is much smaller than a wavelength ($<\lambda/10$), a wave in the material would be dominantly characterized by refractive phenomena instead of scattering or diffraction phenomena. Therefore, the electromagnetic properties of the material are determined by permittivity and permeability. The reflection and transmission characteristics were calculated using this software; using the theory of homogenization, the effective electromagnetic properties were extracted from the reflection and transmission (S_{11} and

S_{21}, respectively). Please refer to Appendix A for the details of the MATLAB code used to extract the effective properties.

Figure 4.5 shows a slab of finite thickness, d, and permittivity and permeability (ε and μ). Based on the slab characteristics (thickness and material properties) as well as the plane wave, some of the incident field will be transmitted and some reflected. Regions 1 and 3 are free space, while Region 2 represents the material with unknown properties.

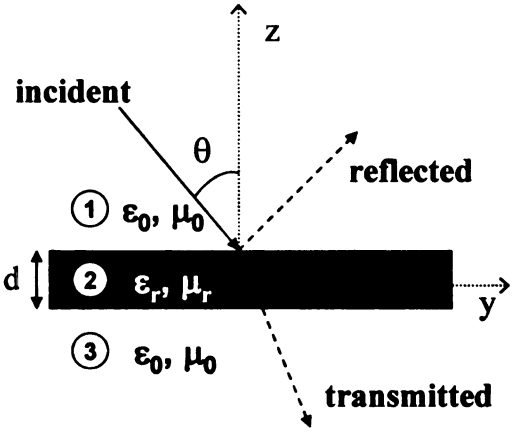

Figure 4.5. Incident plane wave on the surface of a dielectric slab. An incident plane wave hits the surface of a finite slab of thickness, d, with permittivity and permeability (ε_r and μ_r). The wave will be transmitted and reflected based on the slab material properties and thickness and angle of incidence of the plane wave, θ.

For this material, reflection and transmission coefficients for a normally incident transverse electromagnetic (TEM) wave can be represented with S parameters, S_{11} and S_{21}. The impedance, η, is related to the effective permeability and permittivity (μ and ε) of the slab material. The wave number, k, in the equations below is related to the plane wave characteristics (polarization and angle of incidence), frequency (f), and the slab

material properties. For each region, the electric and magnetic field intensity can be calculated by the following equations.

Region 1:

$$\mathbf{E}_1 = \hat{x}E_0^i e^{-jk_0 z} + \hat{x}E_0^r e^{-jk_0 z} \tag{4.1}$$

$$\mathbf{H}_1 = \hat{y}\frac{E_0^i}{\eta_0}e^{-jk_0 z} + \hat{y}\frac{E_0^r}{\eta_0}e^{-jk_0 z} \tag{4.2}$$

$$k_0 = \omega_0\sqrt{\varepsilon_0\mu_0} \tag{4.3}$$

$$\eta_0 = \sqrt{\frac{\mu_0}{\varepsilon_0}} \tag{4.4}$$

Region 2:

$$\mathbf{E}_2 = \hat{x}E_2^+ e^{-jk_2 z} + \hat{x}E_2^- e^{-jk_2 z} \tag{4.5}$$

$$\mathbf{H}_1 = \hat{y}\frac{E_2^+}{\eta_2}e^{-jk_2 z} + \hat{y}\frac{E_2^-}{\eta_2}e^{-jk_2 z} \tag{4.6}$$

$$k_2 = \omega\sqrt{\varepsilon_2\mu_2} = k_2 = \omega\sqrt{\varepsilon_0\varepsilon_r\mu_0\mu_r} = k_0\sqrt{\varepsilon_r\mu_r} \tag{4.7}$$

$$\eta_2 = \sqrt{\frac{\mu_0\mu_r}{\varepsilon_0\varepsilon_r}} = \eta_0\sqrt{\frac{\mu_r}{\varepsilon_r}} \tag{4.8}$$

Region 3:

$$\mathbf{E}_3 = \hat{x}E_3 e^{-jk_0 z} \tag{4.9}$$

$$\mathbf{H}_3 = \hat{y}\frac{E_3}{\eta_0}e^{-jk_0 z} \tag{4.10}$$

By applying boundary conditions at the two interfaces (at z = 0 and z = d), the reflection and transmission coefficients (S_{11} and S_{21}) can be written.

$$S_{11} = \frac{E_0^r}{E_0^i} = \frac{(1-\beta^2)\Gamma_{12}}{1-\Gamma_{12}^2\,\beta^2} \tag{4.11}$$

$$S_{21} = \frac{E_3}{E_0^i} = \frac{(1-\Gamma_{12}^2)\,\beta}{1-\Gamma_{12}^2\,\beta^2} \tag{4.12}$$

$$\Gamma_{12} = \frac{\eta_2 - \eta_0}{\eta_2 + \eta_0} = \frac{\sqrt{\frac{\mu_r}{\varepsilon_r}} - 1}{\sqrt{\frac{\mu_r}{\varepsilon_r}} + 1} \tag{4.13}$$

$$\beta = e^{-j\omega\sqrt{\mu_r \varepsilon_r}\,d} \tag{4.14}$$

The material properties, ε_r and μ_r, can be calculated using these equations (Appendix A). For a simple slab of a homogenous polymer ($\varepsilon' = 2$, $\mu' = 1$) with a normally incident plane wave, the reflection and transmission data was calculated (Figure 4.6).

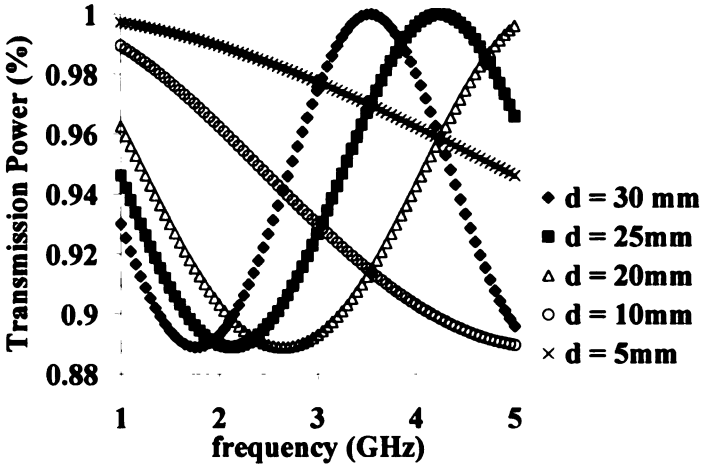

Figure 4.6. Transmission power (%) vs. frequency (GHz) for varying slab thickness for hypothetical material ($\varepsilon' = 2$, $\mu' = 1$, no loss).

As the thickness of the slab increased, the period between resonant frequencies became shorter, resulting in a shift in resonance; the transmission power remained very close to 1

for this range of frequencies. The reflection and transmission characteristics for the ideal magneto-dielectric material (with the permittivity and permeability of interest for this work) were calculated, to better understand how the refection and transmission change with material properties. Table 4.1 shows a list of cases with hypothetical permittivity and permeability and slab thickness.

Table 4.1. Cases for infinite slabs with hypothetical permittivity, permeability and slab thickness for reflection and transmission analysis.

Case	d (mm)	ε'	ε''	μ'	μ''
1	25	2	0	1	0
2	25	2	0	1.5	0
3	25	2	0	1.8	0
4	25	2	0	2.2	0
4a	20	2	0	2.2	0
4b	10	2	0	2.2	0
4c	5	2	0	2.2	0

Two different comparisons were highlighted for this study – first, the permeability was increased with a constant permittivity and secondly, the slab thickness was changed for the case where permeability was slightly greater than permittivity (the objective properties for this work). As the permeability increased, the resonant frequency shifts as well as the transmission power; the transmission power at the resonant frequency was higher for cases with an increased permeability. In fact, for the case where permeability was slightly greater than permittivity (Case 4), the transmission was nearly 100% for this span of frequencies, and remains so for varied slab thickness. This can be expected since the material has an inductive response (high transmission) as μ is

increased. The same trend noted in Figure 4.6 for the original case ($\varepsilon' = 2$, $\mu' = 1$, no loss) was seen for Case 4 as the slab thickness was changed.

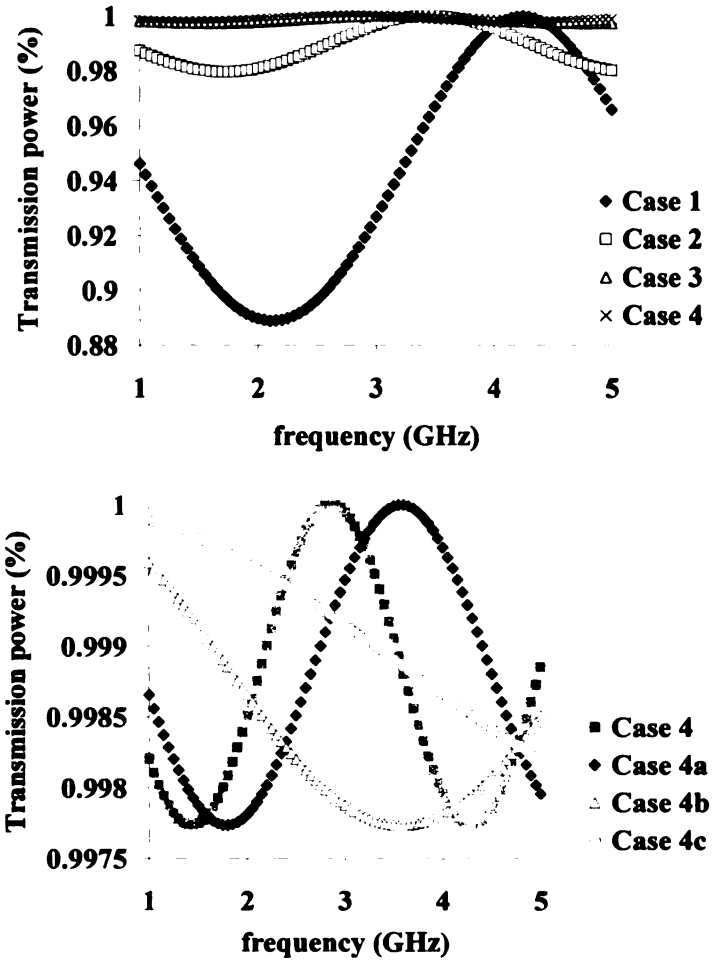

Figure 4.7. Transmission power behaviour for a slab of hypothetical material, corresponding to Table 4.1. Top: Transmission power (%) vs. frequency (GHz) for varying permeability and Bottom: Transmission power (%) vs. frequency (GHz) for varying slab thickness.

By implementing the frequency selective surfaces in the polyethylene slab, the reflection and transmission data can be tailored to resonate at the desired range of frequencies. This

change in the reflection and transmission spectrum correlates to enhanced permittivity and permeability for the composite.

4.4 Square Loop FSS Layered Composites

4.4.1 FSS Array and Composite Geometry

For this work, the square loop FSS element was chosen as it was expected to result in an inductive response due to the nature of the loop. The geometries for the 1 FSS layer composite, the FSS array, and the square loop unit cell are shown in Figure 4.8. For modeling purposes, the material for the square loop was silver, and the polymer layers were polyethylene ($\varepsilon' = 2.5$), although the polymer material was varied for later cases for analysis.

The dimensions and periodicity of the square loop were varied, as well as the features of the polymer layers – thickness and dielectric properties. The reflection and transmission from the geometry was used to extract the effective properties; with the ultimate goal being to achieve a permeability greater than 1, a permittivity not much greater (and preferably smaller) than the permeability, and very low loss.

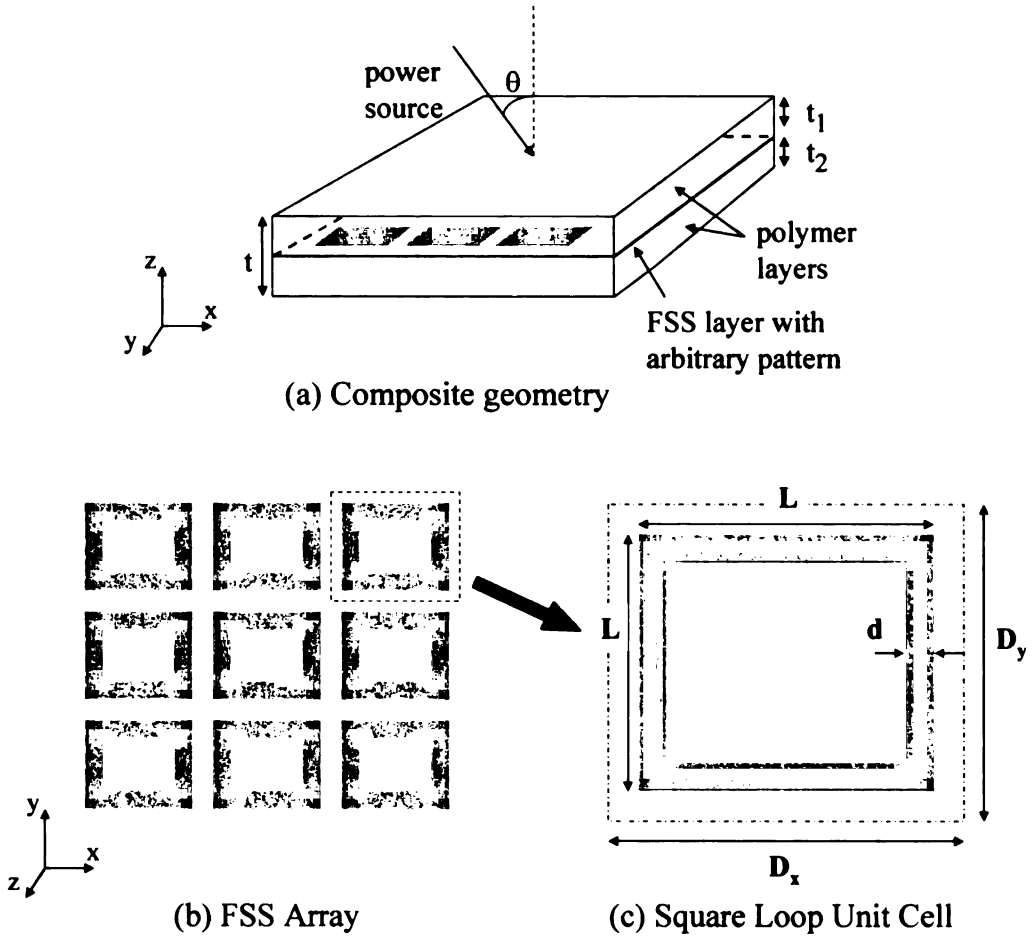

Figure 4.8. FSS layered composite layout. (a) 1-layer FSS composite geometry, (b) FSS array layout, and (c) unit cell for the square loop FSS elements.

4.4.2 Effects of Polymer Layer Characteristics

The polymer or dielectric layers that sandwich the FSS layer(s) had a great effect on the performance of the composite. By changing the thickness and dielectric properties of the polymer layer, their effects on the overall performance were analyzed. For the analysis of polymer layer thickness effects, Table 4.2 shows the dimensions of the square loop elements and unit cell as well as the slab thickness.

Table 4.2. Composite and FSS array conditions for varying total thickness. Total thickness (t) was varied while the square loop layout and size as well as polymer material (polyethyelene) were kept constant.

Case	L (mm)	d (mm)	D_x (mm)	D_y (mm)	t (cm)	$\varepsilon_{polymer}$
T1	5	0.5	5.5	5.5	3.6	2.25-0.001j
T2	5	0.5	5.5	5.5	3	2.25-0.001j
T3	5	0.5	5.5	5.5	2.6	2.25-0.001j
T4	5	0.5	5.5	5.5	2.4	2.25-0.001j

The total thickness of the composite was varied by changing the thickness of the outer sandwiching polypropylene layers; for each case, the thickness of the outer layers were equal ($t_1 = t_2$ in Figure 4.8). The square loops were modeled as silver traces on the polyethylene surface. The initial simulations were carried out for an infinite FSS array (infinite in x and y direction).

The transmission and reflection characteristics can be plotted as a function of frequency; the transmission (S21) magnitude and phase are shown as a function of frequency in Figure 4.9. Using the theory of homogenization, the effective electromagnetic properties can be extracted for these composites. The effective permittivity and permeability (real parts) vs. frequency can be found in Figure 4.10.

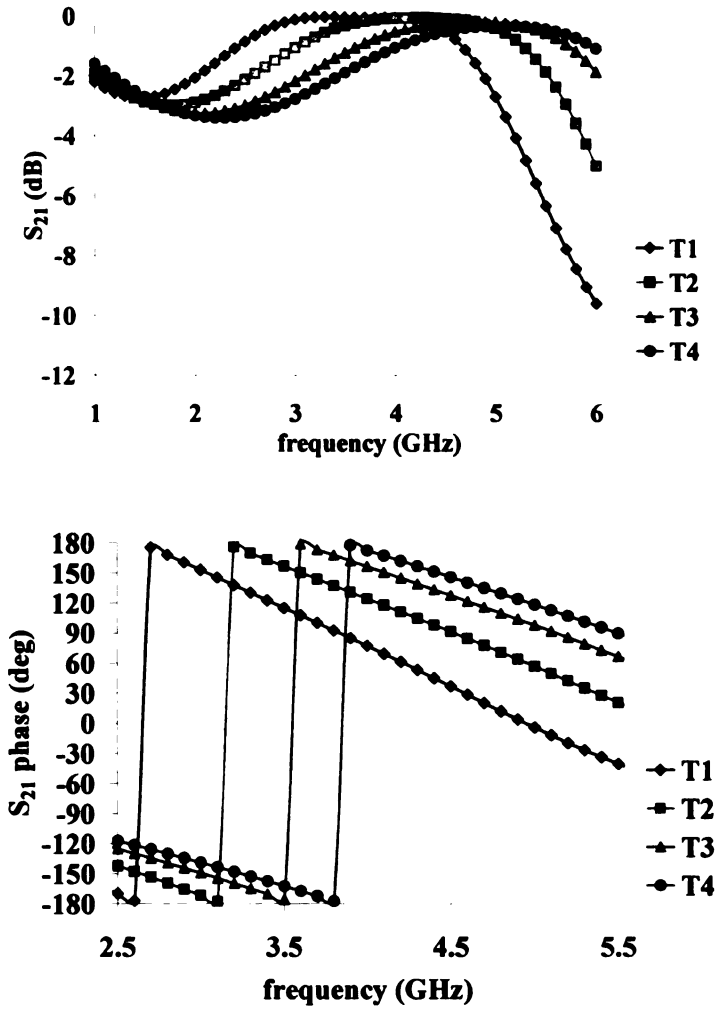

Figure 4.9. Transmission characteristics for composites with varying thickness, corresponding to Table 4.2. *Top*: S_{21} (dB) vs. frequency (GHz) and *Bottom*: S_{21} phase (degrees) vs. frequency (GHz).

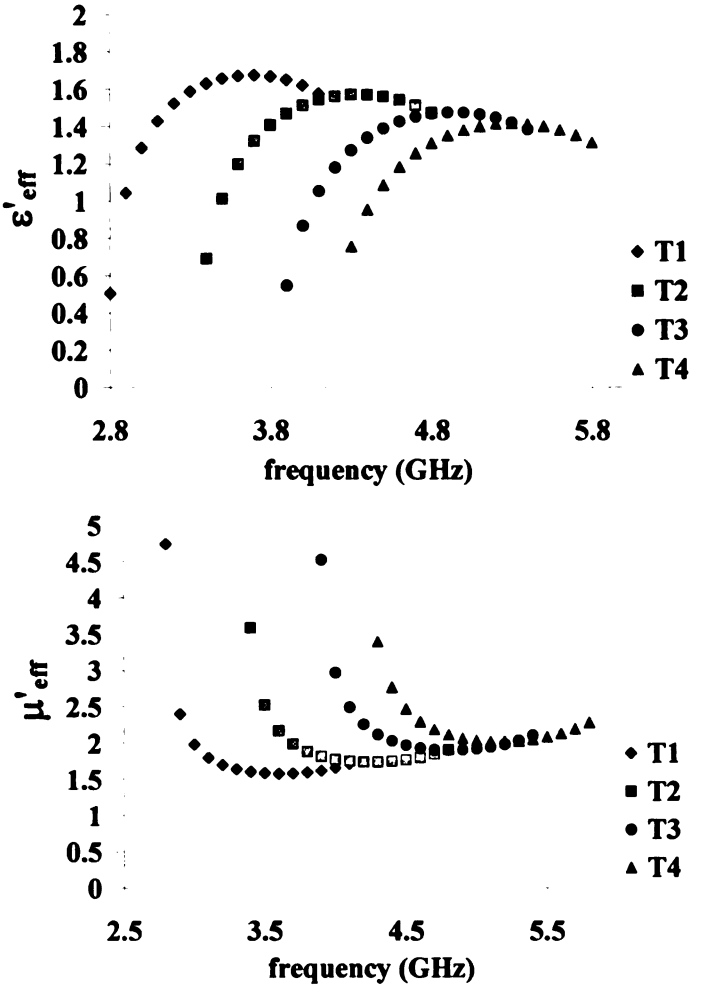

Figure 4.10. Effective permittivity and permeability vs. frequency (GHz) for varying composite thickness, corresponding to Table 4.2. *Top*: Effective permittivity (ε'_{eff}) vs. frequency (GHz) and *Bottom*: Effective permeability (μ'_{eff}) vs. frequency (GHz).

Additionally, the loss remained very low for these cases; Figure 4.11 shows the loss tangent for both permittivity and permeability for these cases.

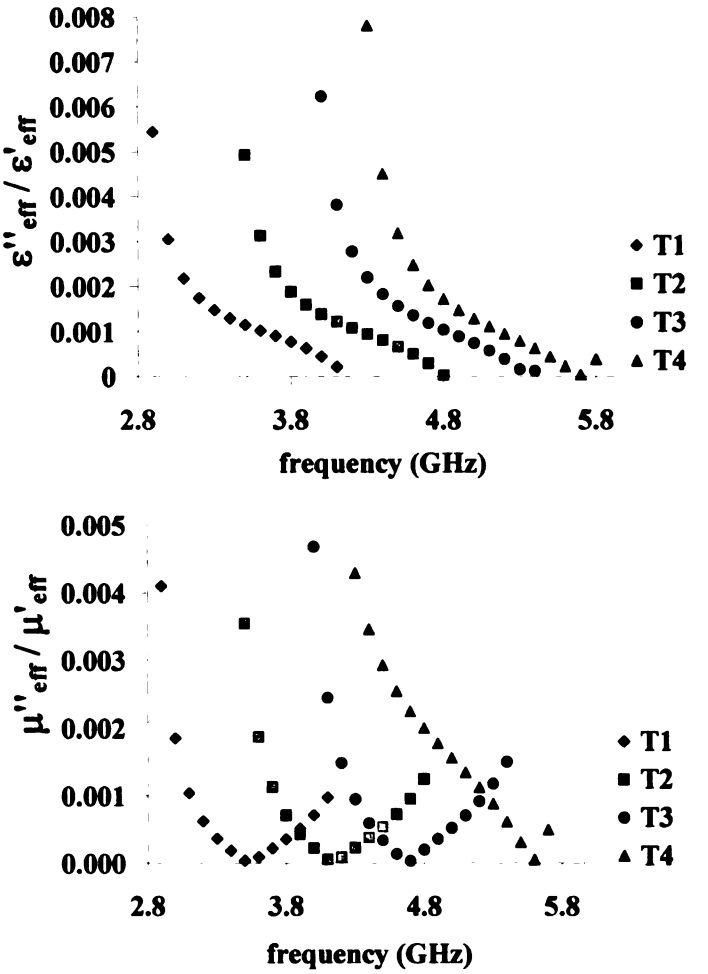

Figure 4.11. Loss characteristics for varying composite thickness, corresponding to Table 4.2. Top: Permittivity loss tangent ($\varepsilon''_{eff} / \varepsilon'_{eff}$) vs. frequency (GHz) and Bottom: Permeability loss tangent (μ''_{eff} / μ'_{eff}) vs. frequency (GHz).

The original objective for the effective properties was reached for each of these cases. Relative permeability ranged from 1.5-3 while relative permittivity ranged from 1-2 for the frequency range from 3-6 GHz. Moreover, the loss tangent was very low for both permittivity and permeability (approximately 10^{-3}). As the thickness of the composite

increased, the response shifted in frequency; this can be attributed to the strong dependence of frequency to the wavelength.

Another interesting variation to the composite structure would be to change the dielectric properties of the polymer substrate layers. Simulations were carried out with a basic epoxy (ε = 3.6-0.0003j) and Rogers RT/duroid 6006 (ε = 6.15-0.0019j) as the polymer layers. Table 4.3 shows the composite and FSS geometries for this analysis.

Table 4.3. Composite and FSS array characteristics for varying polymer substrates. Total thickness (t) was kept constant, along with square loop layout and size, while the material for the polymer layers was varied.

Case	L (mm)	d (mm)	D_x (mm)	D_y (mm)	t (cm)	$\varepsilon_{polymer}$
T2	5	0.5	5.5	5.5	3	2.25-0.001j
T2-a	5	0.5	5.5	5.5	3	3.6-0.0003j
T2-b	5	0.5	5.5	5.5	3	6.15-0.0019j

By comparing the original Case T2 to Cases T2-a and T2-b (as the polymer dielectric constant increases), we can see how the dielectric properties of the polymer layers affect the composite performance. Figure 4.12 shows the transmission characteristics for these cases.

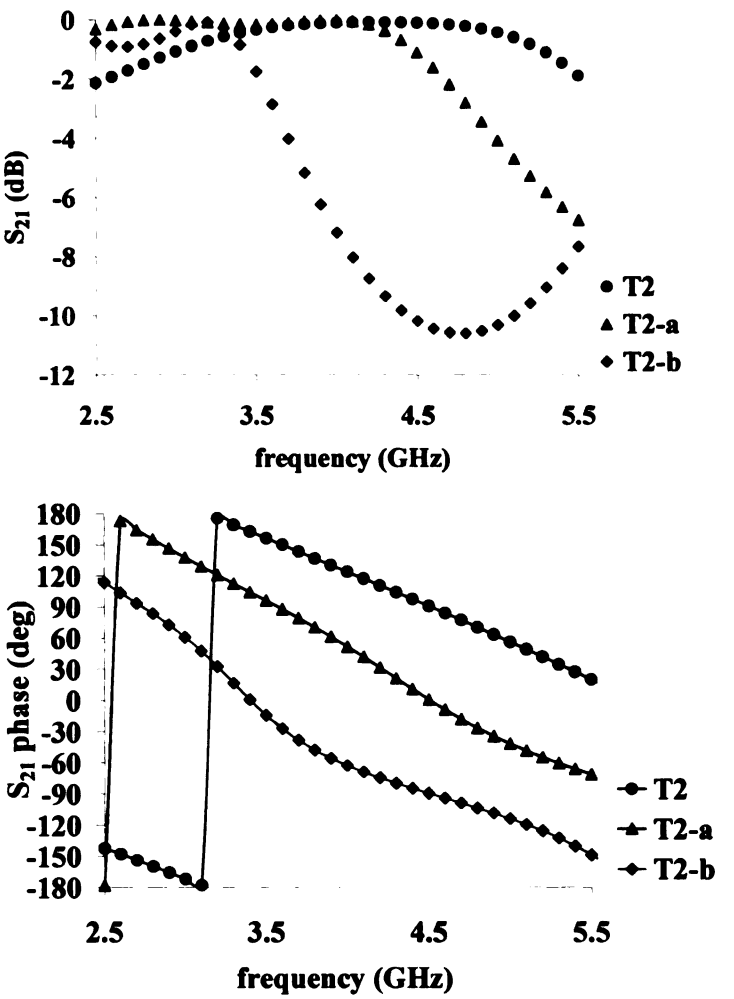

Figure 4.12. Transmission characteristics for composites with varying polymer layer materials, corresponding to Table 4.3. Top: S_{21} (dB) vs. frequency (GHz) and Bottom: S_{21} phase (degrees) vs. frequency (GHz).

The effective properties for the same cases are plotted in Figure 4.13. When analyzing just Cases T2-a vs. T2, for example, one can see that by increasing the dielectric constant of the polymer layers, the bandwidth shifts to lower frequencies. This is an important design tool, in that the thickness of the composite can be decreased if the polymer layer dielectric properties were increased.

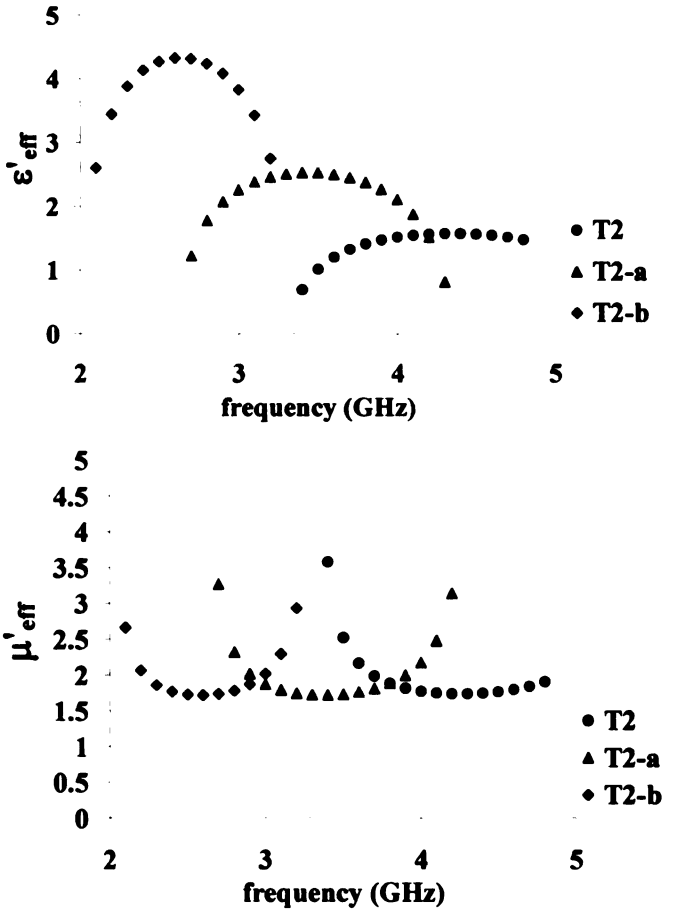

Figure 4.13. Effective permittivity and permeability vs. frequency (GHz) for varying polymer dielectric properties, corresponding to Table 4.3. *Top*: Effective permittivity (ε'_{eff}) vs. frequency (GHz) and *Bottom*: Effective permeability (μ'_{eff}) vs. frequency (GHz).

It is important to note that the permeability remained in the same range when the dielectric properties were changed, but only shifted in frequency; however, the permittivity increased for the cases with the higher dielectric property polymer layer. This can be expected, since the substrate itself had an enhanced permittivity.

Additionally, the loss tangents followed a similar trend with a shift in frequency bandwidth.

4.4.3 Effects of Element Size and Periodicity

In addition to understanding how the substrate properties and slab thickness affect the behavior of the FSS composite, the effect of FSS element size and periodicity was also analyzed. Table 4.4 shows the list of geometries corresponding to this study.

Table 4.4. FSS composite geometries corresponding to various FSS element sizes and periodicities.

Case	L (mm)	d (mm)	D_x (mm)	D_y (mm)	t (cm)	$\varepsilon_{polymer}$
S1	4	0.5	4.5	4.5	3	3.6-0.0003j
S2	5	0.5	5.5	5.5	3	3.6-0.0003j
S3	7	0.75	7.5	7.5	3	3.6-0.0003j
S4	8	1	8.5	8.5	3	3.6-0.0003j
P1	4	0.5	5	5	3	3.6-0.0003j
P2	5	0.5	6	6	3	3.6-0.0003j
P3	7	0.75	8	8	3	3.6-0.0003j
P4	8	1	9	9	3	3.6-0.0003j

The square loop FSS element was again used for simulations as shown in Section 4.4.1; epoxy was chosen for the polymer layers, since fabrication would involve using epoxy resin for the sandwiching layers. For the comparisons shown here, the total thickness of the composite was kept constant at 3cm (t_1=t_2). These simulations for this analysis were for an infinite FSS array. When just comparing the effect of changing the size of the square loops, Cases S1-S4 can be compared; for these cases, the distance between

elements was kept constant at 1mm. Figure 4.14 shows the transmission characteristics for these cases.

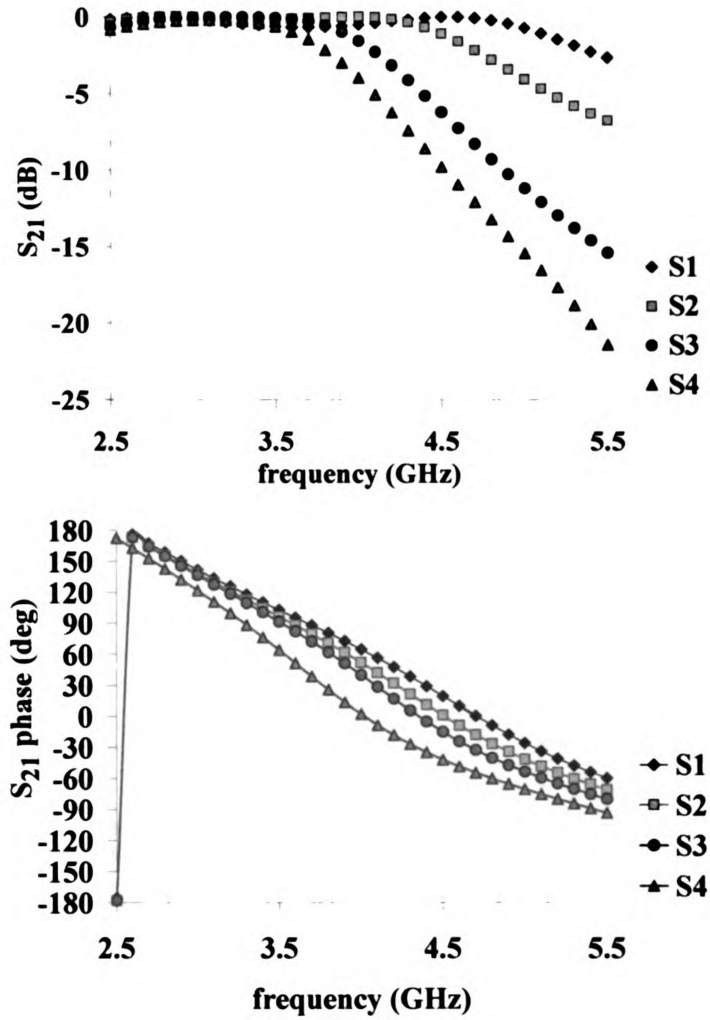

Figure 4.14. Transmission characteristics for FSS layered composite with varied element size, corresponding to Table 4.4. *Top*: Transmission magnitude, S21 (dB), vs. frequency (GHz) and *Bottom*: Transmission phase, S21 phase (deg), vs. frequency (GHz).

Similar to the approach shown in the previous section, the effective permittivity and permeability can be extracted from the reflection and transmission of the plane wave through the composite; these are shown in Figure 4.15.

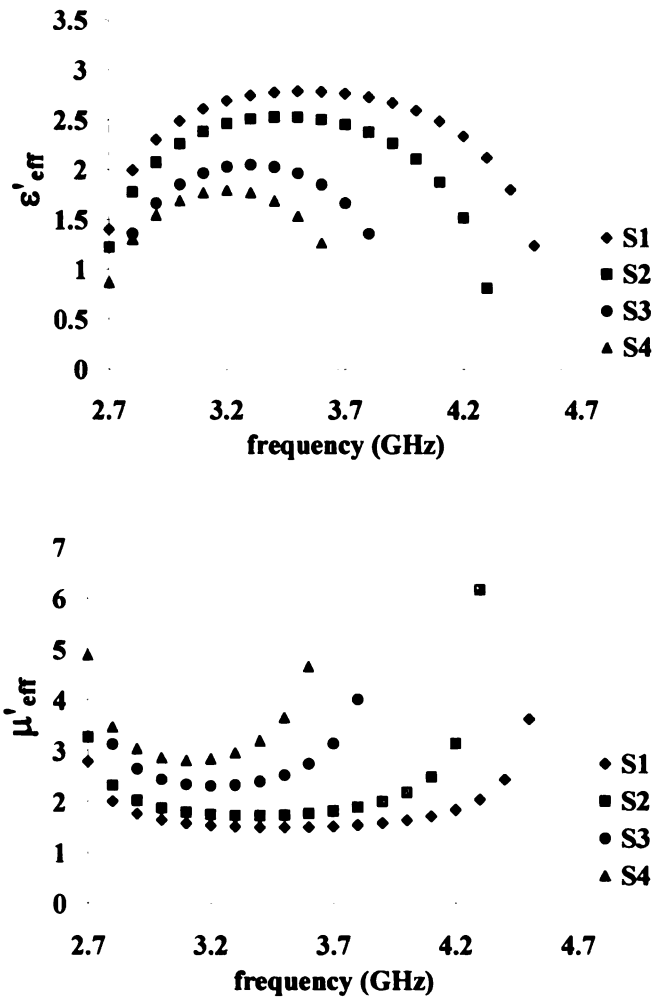

Figure 4.15. Effective properties for FSS layered composites with varying element size, corresponding to Table 4.4. *Top*: Effective permittivity (ε'_{eff}) vs. frequency (GHz) and *Bottom*: Effective permeability (μ'_{eff}) vs. frequency (GHz).

Figure 4.16 highlights the loss for these cases; this behavior followed similar trends as noted in the previous section.

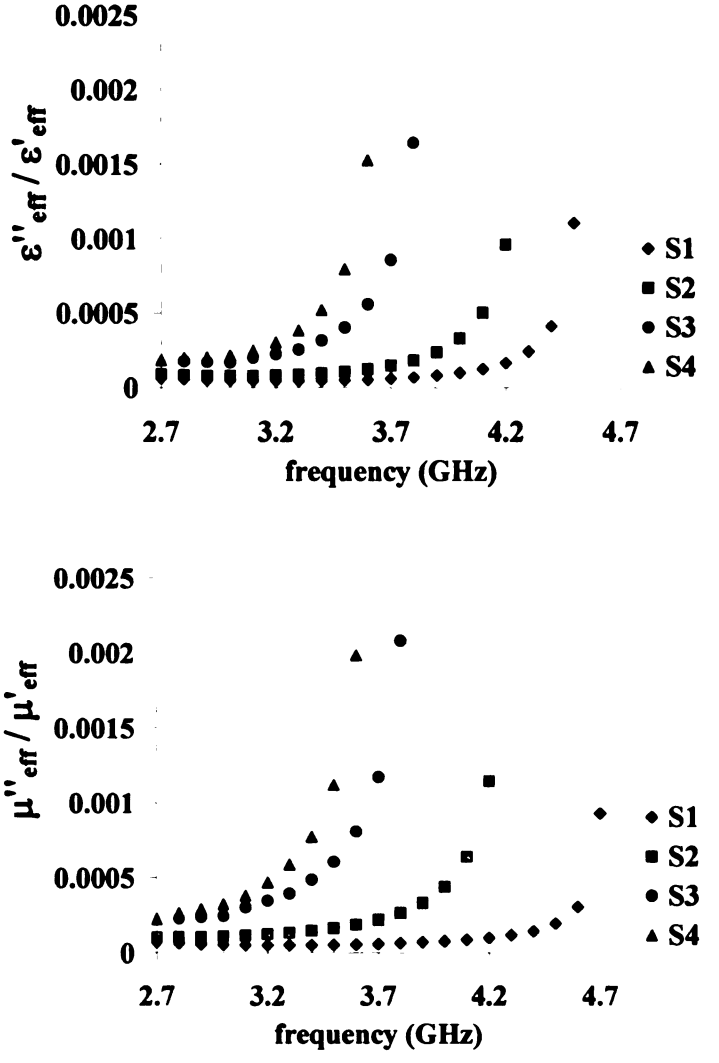

Figure 4.16. Loss characteristics for FSS layered composite with varied element size, corresponding to Table 4.4. *Top*: Effective dielectric loss tangent ($\varepsilon'_{eff}/\varepsilon''_{eff}$) vs. frequency (GHz) and *Bottom*: Effective permeability loss tangent (μ'_{eff}/μ''_{eff}) vs. frequency (GHz).

When comparing these cases, it was noted that the effective permeability increased while the effective permittivity decreased as the element size was increased. This can be attributed to the increased area of metal leading to an increased inductance.

Moreover, because the size of the elements increased while the distance between them remained the same, the capacitance was lower for the larger elements, leading to the lower effective permittivity.

Although there was an increase in permeability, which would be ideal for the design goals for this thesis, the bandwidth was decreased. As the element size increased the bandwidth is reduced, which can be a disadvantage for several applications. From the design standpoint, it would be important to find a point where the permeability is enhanced and the bandwidth is still sufficient.

There was a slight shift in transmission magnitude as the square loop elements were spaced closer together. The effective properties changed in magnitude as a result of a tighter packing ratio, as seen in Figure 4.18. As the square loop elements were packed closer together, the mutual coupling between the elements becomes stronger, thereby creating a stronger response as an inductive trace. This can be used to the advantage of the designer; to pack elements very tightly (to the limit of manufacturability) to achieve the greatest enhancement of permeability, a property of great importance for magneto-dielectrics.

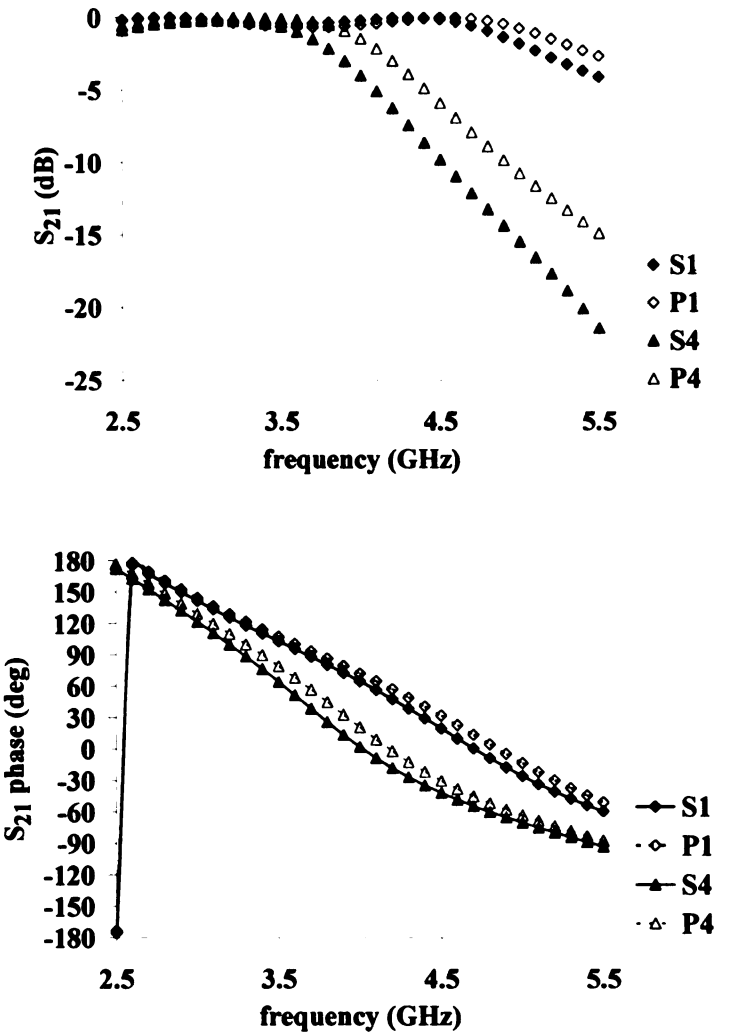

Figure 4.17. Transmission data comparison for FSS composites with varied element size and periodicity, corresponding to Table 4.4. *Top*: Transmission magnitude, S_{21}(dB), vs. frequency (GHz) and *Bottom*: Transmission phase, S_{21} phase (deg), vs. frequency (GHz)

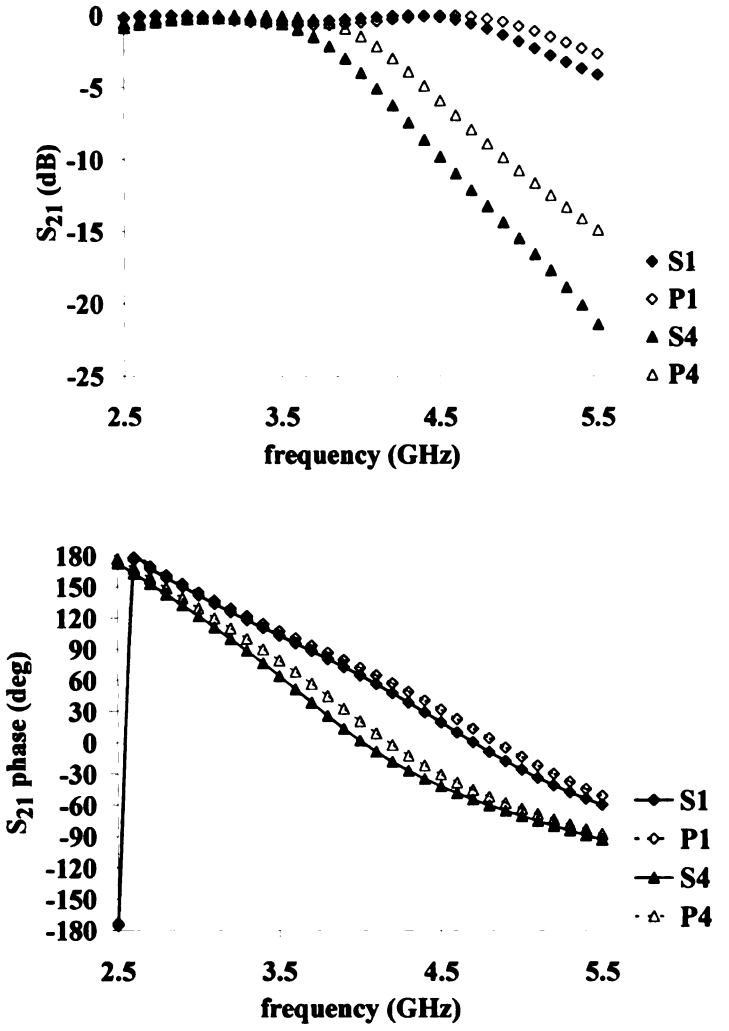

Figure 4.17. Transmission data comparison for FSS composites with varied element size and periodicity, corresponding to Table 4.4. *Top*: Transmission magnitude, S_{21}(dB), vs. frequency (GHz) and *Bottom*: Transmission phase, S_{21} phase (deg), vs. frequency (GHz)

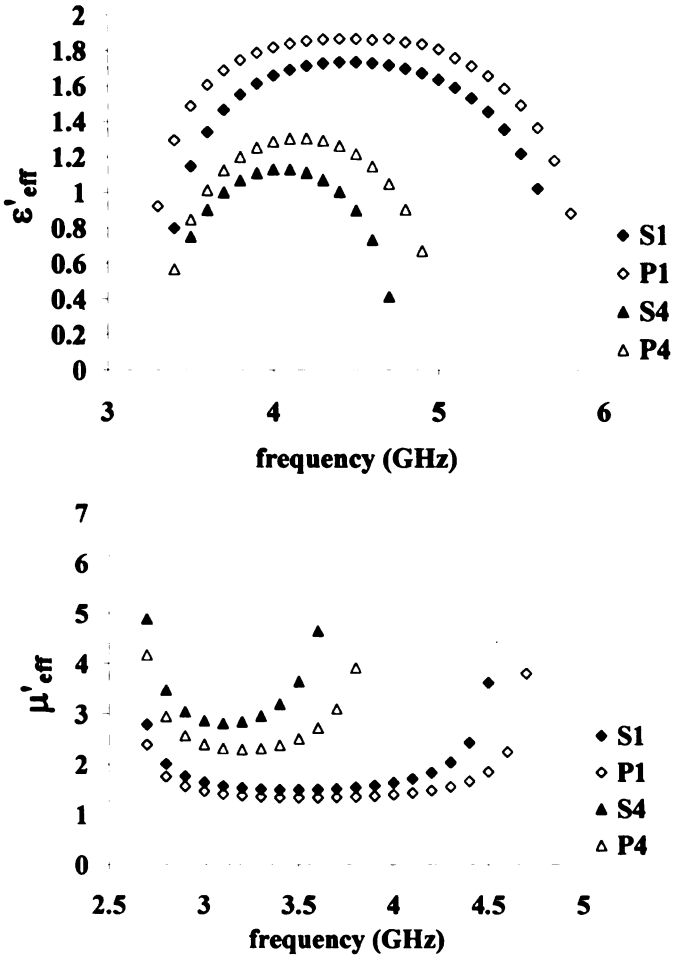

Figure 4.18. Effective properties for FSS layered composites with varying element size and periodicity, corresponding to Table 4.4. *Top*: Effective permittivity (ε'_{eff}) vs. frequency (GHz) and *Bottom*: Effective permeability (μ'_{eff}) vs. frequency (GHz).

4.4.4 FSS Composite in a Waveguide vs. Infinite FSS Composite

Until this point, all the simulation results discussed were for cases with an infinite FSS array between the polymer layers. When samples are fabricated for characterization, a waveguide will be used to measure the reflection and transmission through the composite over a specific range of frequencies. The size of the waveguide will be standard based on the frequency band for measurement. Therefore, this characterization technique will impose a design constraint; it was necessary to determine how many periods would be required to mimic the same behavior noted for an infinite FSS layer.

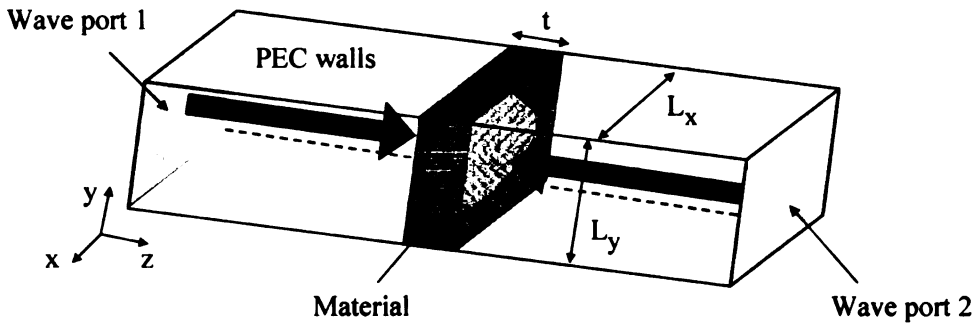

Figure 4.19. HFSS simulation geometry for the material within a waveguide.

Ansoft HFSS was used to mesh the composite geometry for the case of a composite material within a waveguide, the same way the material will eventually be characterized - see Figure 4.19. The material would be at the center of the perfect electrically conducting (PEC) waveguide; where the distance between the material and the waveports would be based on the wavelength ($\lambda/4$). For simulation purposes, a plane wave is de-embedded to hit the material at normal incidence.

For an FSS with arbitrary shaped elements (square plates for the example below), one would expect that the behavior of the FSS would match the infinite case with more periods, as seen in Figure 4.20.

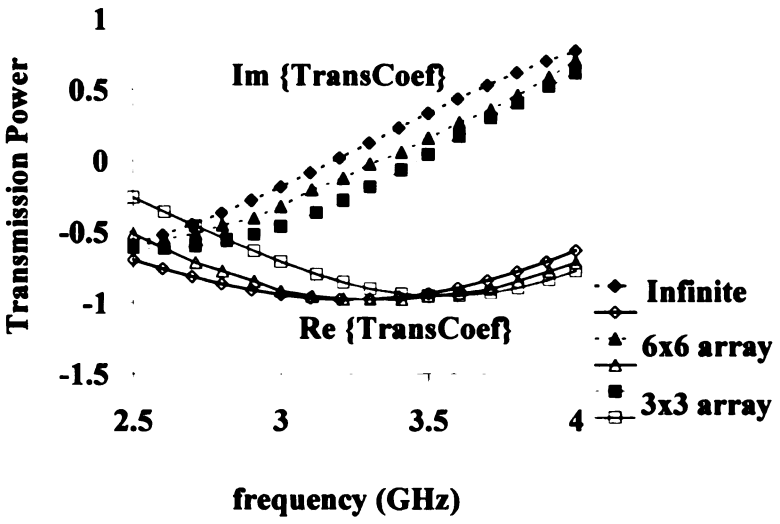

Figure 4.20. Transmission vs. frequency (GHz) for an infinite FSS array, 3x3 FSS array, and 6x6 FSS array

For this case, with a 6x6 FSS array, the transmission properties almost matched the infinite case. A simulation was carried out for composites with a square loop FSS layer, Case T1 in Table 4.2, in an S-band waveguide. A standard S-band waveguide is 72x34mm; with the FSS geometry shown in Table 4.2, the FSS array was a 13x6 array of square loops.

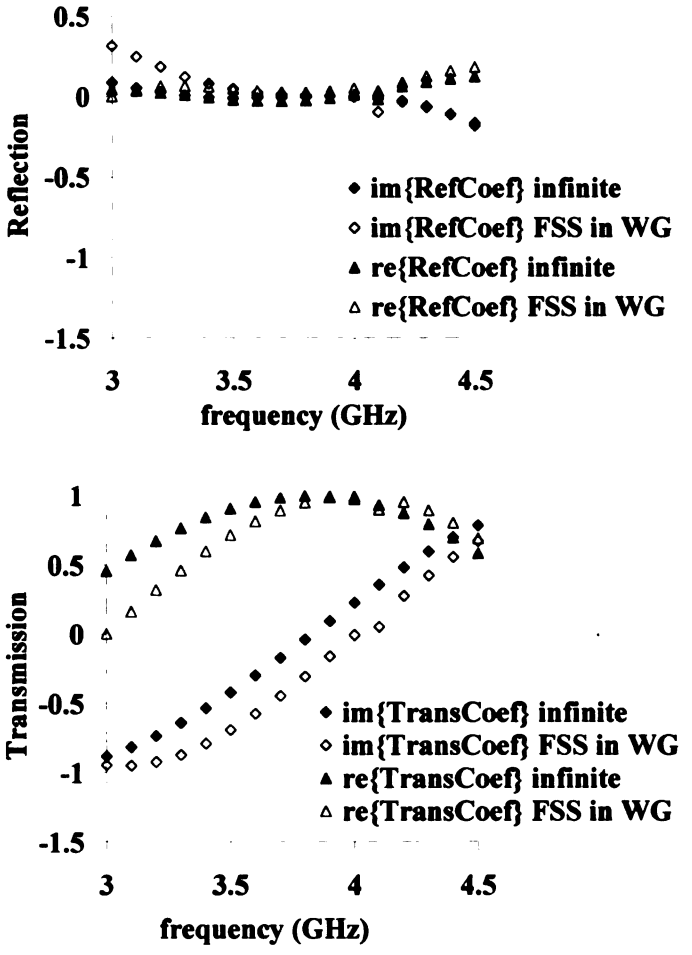

Figure 4.21. Reflection and transmission behavior for an infinite FSS vs. an FSS in a waveguide. *Top*: Reflection vs. frequency (GHz) and *Bottom*: Transmission vs. frequency (GHz).

The transmission and reflection data correlated well to the infinite case, indicating the effective properties would follow a similar trend (Figure 4.22).

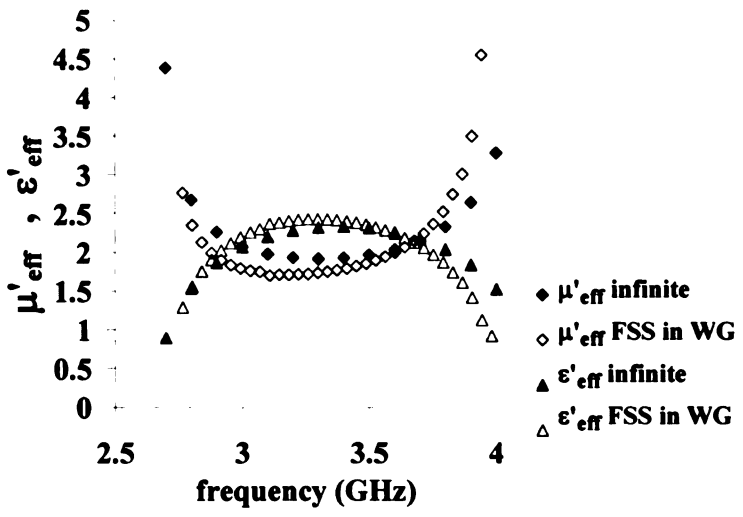

Figure 4.22. Effective permittivity (ε'_{eff}) and permeability (μ'_{eff}) vs. frequency (GHz) for both an infinite FSS and FSS in a waveguide.

The effective permeability and permittivity were compared for the case with an infinite FSS array layer and the 13x6 element FSS array for the composite in a waveguide. The bandwidth was shifted and slightly reduced for the case of the FSS in a waveguide. This analysis verified that the number of periods that would fit in the S-band waveguide would be sufficient to duplicate the behavior previously modeled for the infinite FSS array; the results of this study were important as they have an impact on the fabrication and characterization limits.

4.4.5 Alternative Element Geometries – Hexagonal Loop

As mentioned in the previous section, when the FSS square loop elements were placed closer together on the array, there was a greater mutual inductance, and a more enhanced permeability. To take advantage of this feature, it would be beneficial to choose an element that is capable of the tightest packing density – hexagons. Hexagonal loops (Figure 4.23) were modeled since they have the tightest possible packing density; Ansoft HFSS was used to model these materials in a waveguide using the technique discussed previously.

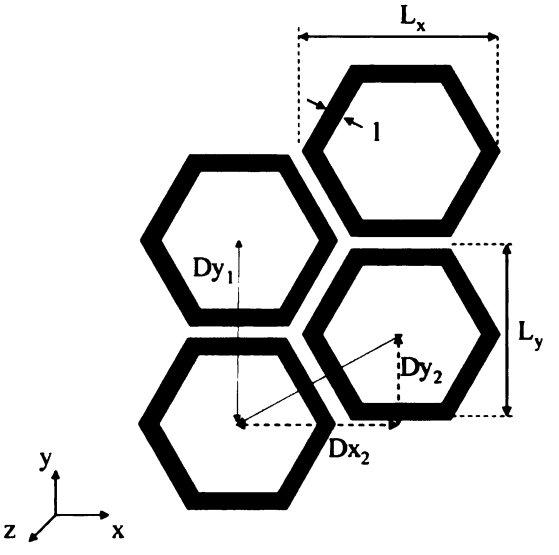

Figure 4.23. Hexagonal loop FSS elements geometry.

The conditions for the hexagonal loop FSS layered composites can be found in Table 4.5; an S-band waveguide was used for the simulations for these cases.

Table 4.5. Hexagonal loop FSS array and composite dimensions.

Case	L_x (mm)	L_y (mm)	d (mm)	D_{y1} (mm)	D_{x2} (mm)	D_{y2} (mm)	t (cm)	$\varepsilon_{polymer}$
H1	5	4.33	0.5	5.33	4.75	2.67	3.6	2.25-0.001j
H2	5	4.33	0.5	5.33	4.75	2.67	3	2.25-0.001j
H1-a	7	6.06	0.75	7.06	6.25	3.53	3.6	2.25-0.001j
H2-a	7	6.06	0.75	7.06	6.25	3.53	3	2.25-0.001j

The size of the hexagonal loops was varied as well as the thickness of the composite, similar to the study previously discussed for square loops. The permittivity and permeability followed a similar trend as seen for square loop FSS elements; the bandwidth shifted as the thickness of the composite was changed. Figure 4.24 shows the effective permittivity and permeability as a function of frequency for these cases.

To understand whether the greater mutual inductance resulted in a more enhanced permeability, Cases H2-a can be compared to Case S3 (Table 4.4, except for a finite FSS in a waveguide, for comparison purposes); a comparison of the effective properties for these cases can be found in Figure 4.25. The effective permeability was greater for the hexagonal loops when compared to the same size square loops, due to the fact that a tighter packing ratio resulted in the greater inductive response.

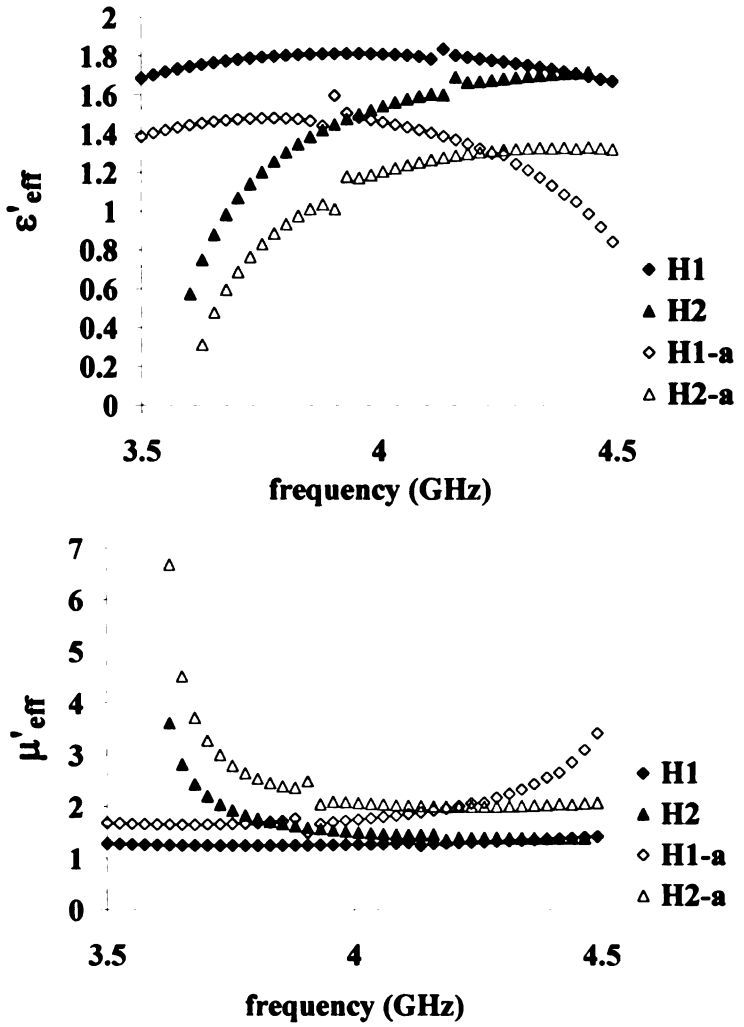

Figure 4.24. Effective electromagnetic properties for varying hexagonal loop FSS array geometries, corresponding to Table 4.5. *Top*: Effective permittivity, ε'_{eff}, vs. frequency (GHz) and *Bottom*: Effective permeability, μ'_{eff}, vs. frequency (GHz).

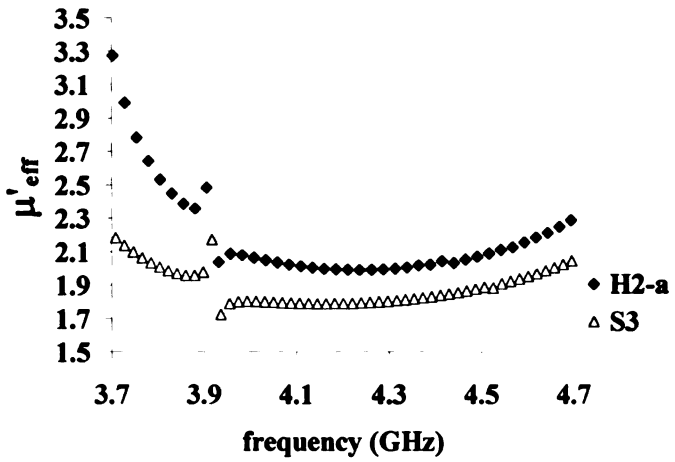

Figure 4.25. Effective permeability (μ'_{eff}) vs. frequency (GHz) for hexagonal loop and square loop FSS array layered composites.

4.4.6 Manufacturing Uncertainty Analysis

When the FSS layered composites are eventually fabricated, it can be assumed that there will always be structural flaws – whether the elements are not perfectly etched or if there are voids or inadequate contact at the interface between layers. Before fabrication of the composites proceeded, simulations were carried out in order to understand how flaws to the composite construction would affect the performance of the material – specifically the electromagnetic properties, since they are the basis of the design. Table 4.6 shows a list of cases where flaws were present in the square loop FSS elements for the composite geometry for Case T1 (shown in Table 4.2).

Table 4.6. Manufacturing uncertainty analysis cases for flaws in the FSS elements for Case T1 (Table 4.1).

Case	FSS Element Flaws
a	Rounded corners on outside of loop
b	4 small tears in square loop
c	Rounded outer and inner corners of loop
d	8 small tears in square loop
e	Rounded outer and inner corners with minor tear in loop
f	8 small tears and rounded edges with uneven periodicity

The performance of the composite was minimally affected by the element flaws; rounded corners seemed to have a greater effect than tears in the square loop. Besides flaws in the element quality, there could also be defects in the composite structure. Pockets of air at the interface between layers are highly probable and could affect the composite performance. Simulations were carried out to understand how voids within the composite can affect the properties.

Ansoft HFSS was used for this study; air bubbles were added to the composite geometry and randomly spaced in the polymer layers and at the interface between the FSS layer and the polymer. The volume percent of the air bubbles was varied, and these cases were compared to the hexagonal loop Case H1.

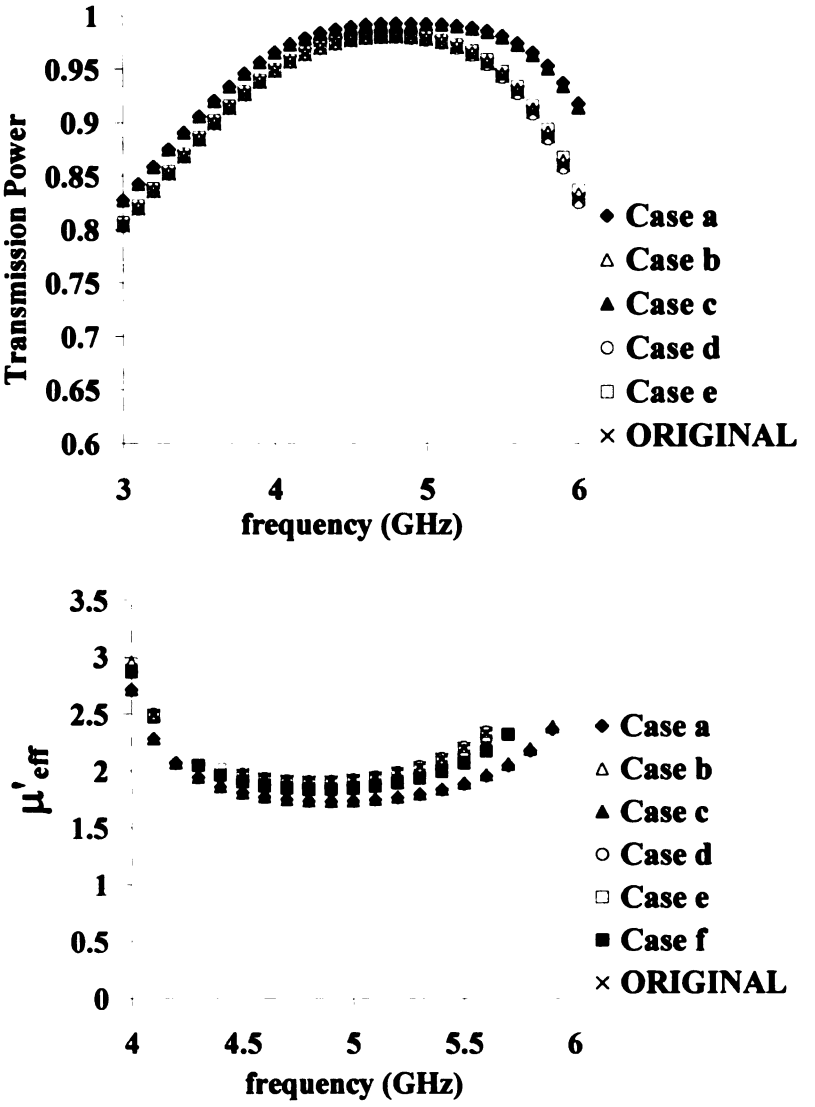

Figure 4.26. Performance characteristics for various flawed FSS samples compared to the original case. *Top*: Transmission power vs. frequency (GHz) and *Bottom*: Effective permeability (μ'_{eff}) vs. frequency (GHz).

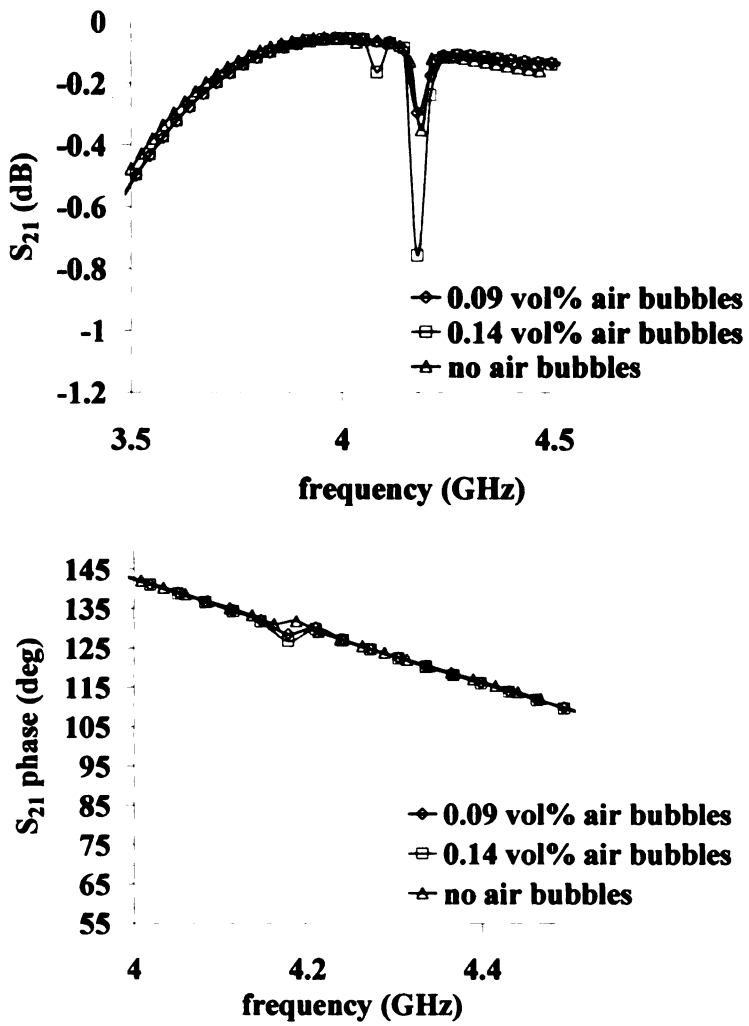

Figure 4.27. Transmission data for FSS layered composites with air bubbles within the matrix and at the interface of the FSS layer. *Top*: Transmission magnitude, S_{21} (dB), vs. frequency (GHz) and *Bottom*: Transmission phase, S_{21} phase (deg), vs. frequency (GHz).

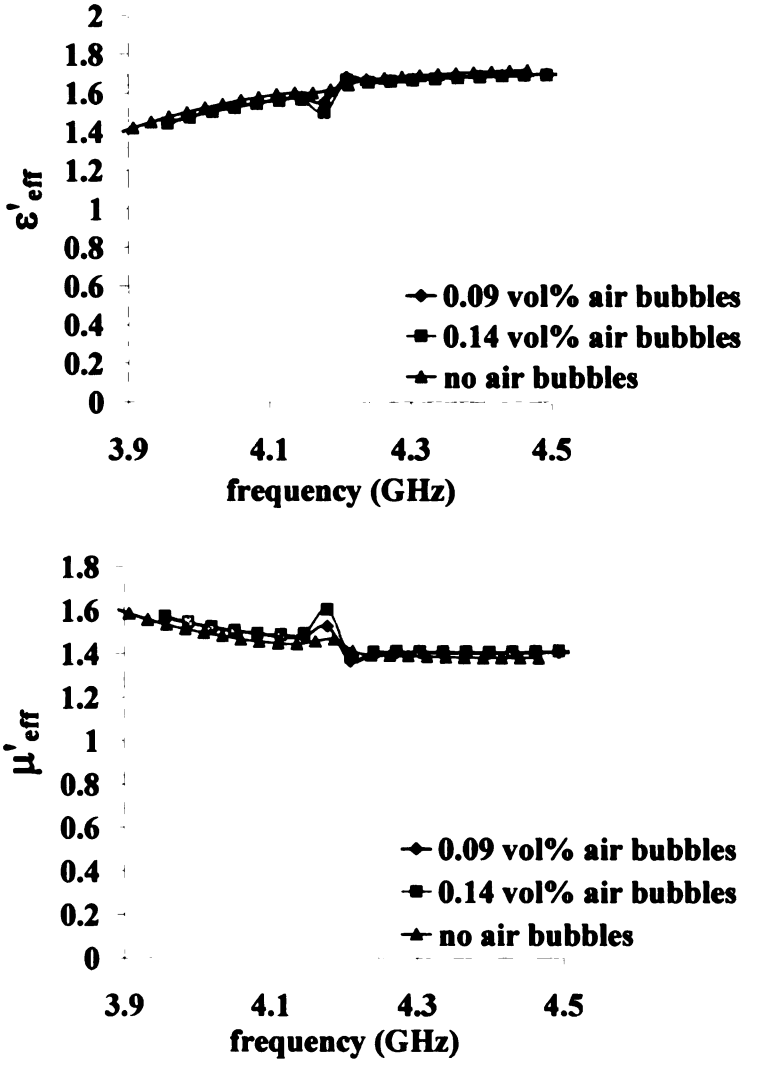

Figure 4.28. Effective electromagnetic properties for hexagon loop FSS composites with air bubbles within the polymer layers and at the interface. Top: Effective permittivity, ε'_{eff}, vs. frequency (GHz) and Bottom: Effective permeability, μ'_{eff}, vs. frequency (GHz).

The air bubbles had a very small effect on the overall effective properties; this could be due to the relative thickness of the sample. For very thin composites, air bubbles will have a greater effect on the performance of the material.

4.4.7 Angle of Incidence Dependence

The previous cases discussed thus far were all simulations for a normally incident power source to the surface of the material. Frequency selective surfaces are known to have a strong scan angle dependence; to lessen this dependence, smaller FSS elements (<λ/12) were used since the scan angle dependence would decrease for such cases.

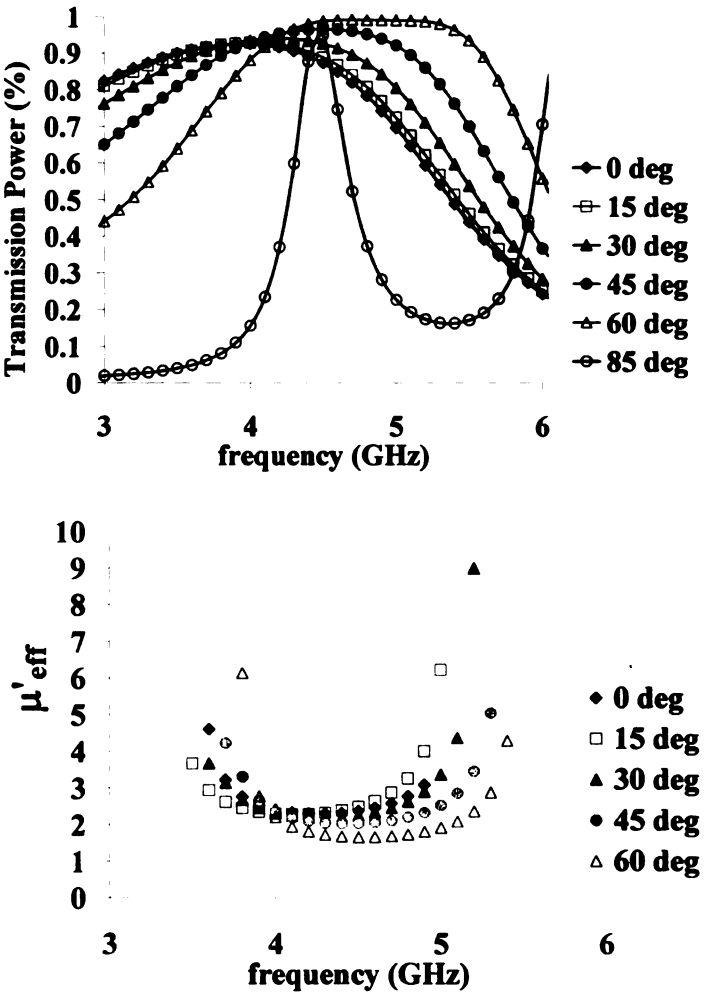

Figure 4.29. Composite performance for varying scan angle for Case S2 with a polyethylene substrate (Table 4.4). Top: Transmission power vs. frequency (GHz) for varying angle of incidence and Bottom: Effective permeability, μ'_{eff}, vs. frequency (GHz) for varying angle of incidence for Case S2 (Table 4.4).

Two separate cases were modeled to understand the angle of incidence dependence for the effective properties of these materials and how this dependence is affected by the size of the FSS element and frequency. The first case shown was Case S2 from Table 4.4 with polyethylene polymer layers; the transmission power and permeability are shown as a function of frequency for varying angle of incidence in Figure 4.29. As the frequency increased, there was a slight change in effective permeability.

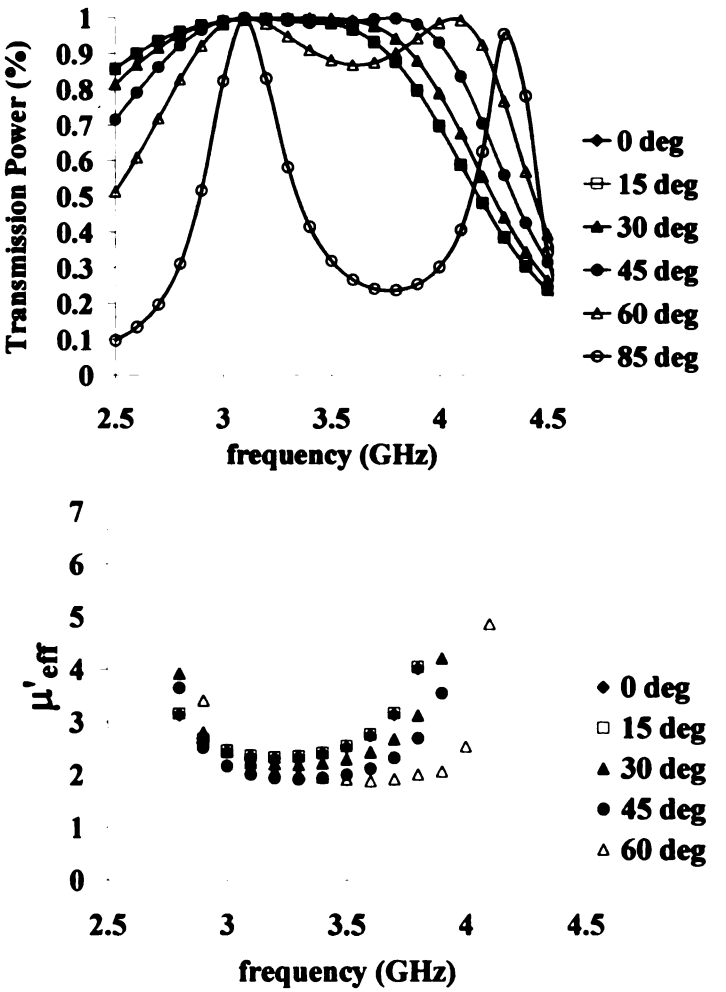

Figure 4.30. Composite performance for varying scan angle for Case S3 with an epoxy substrate (Table 4.4). *Top*: Transmission power vs. frequency (GHz) for varying angle of incidence and *Bottom*: Effective permeability, μ'_{eff}, vs. frequency (GHz) for varying angle of incidence for Case S3 (Table 4.4).

A similar trend was noted for Case S3 from Table 4.4 (with the epoxy as the polymer layers) as shown in Figure 4.30. Although there was a slight dependence on angle of incidence, the permeability and permittivity were within the original goal for angles of incidence from 0-60 degrees. However, this slight dependence on angle of incidence represents a cautionary tale since, for homogenous materials, permittivity and permeability should be constant with scan angle.

4.4.8 Polarization Effects

The modeling results thus far were shown for TE polarization; however, it was also important to evaluate the dependency on polarization. A comparison was made between TE and TM polarizations for cases modeled previously. The FSS geometry for Cases S2 and S3 (in Table 4.4) were modeled and compared for both TE and TM polarizations. As shown in Figure 4.31, there was minimal change in the transmission and reflection characteristics for these cases.

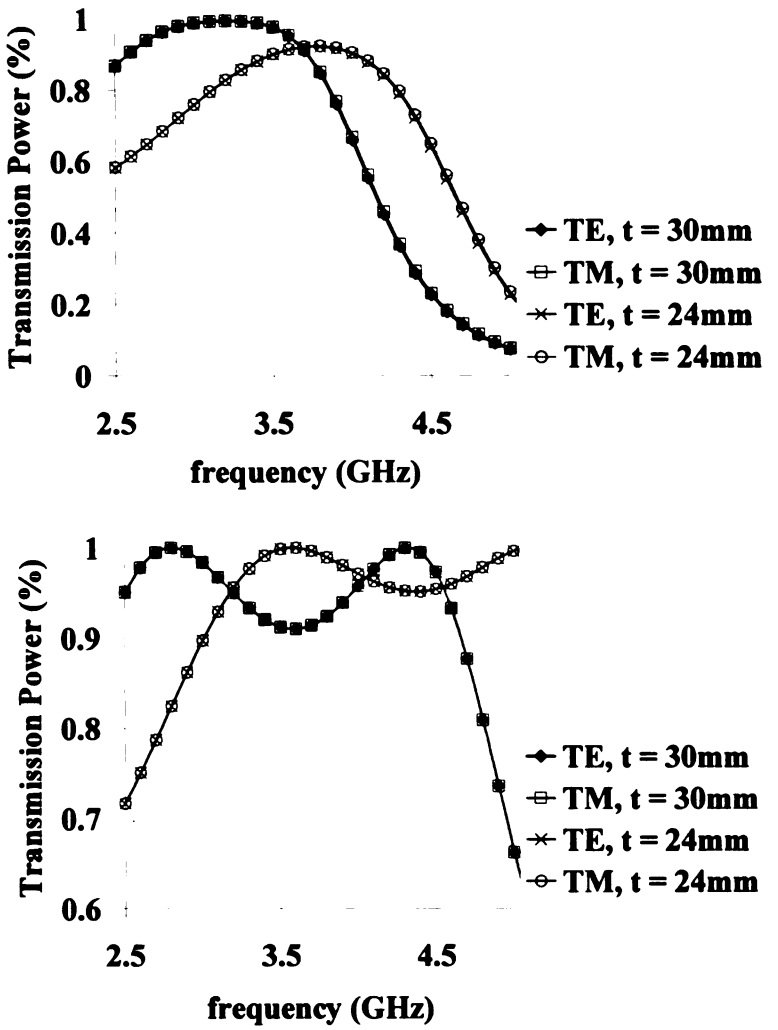

Figure 4.31. Transmission characteristics comparison for TE and TM polarizations. *Top*: Transmission power (%) vs. frequency (GHz) for Case S3 from Table 4.4 and *Bottom:* Transmission power (%) vs. frequency (GHz) for Case S2 from Table 4.4.

Because the reflection and transmission characteristics are independent of polarization, the effective properties would follow the same trend.

4.5 Composites with Multiple FSS Layers

The FSS layered composites modeled in the previous sections were for one layer FSS composites with varying element size, geometry, and distribution; as well as varying polymer layer materials and thicknesses. Multiple FSS layers can be layered to create a multi-layer composite with possibly better permittivity and permeability than those materials with one layer (Figure 4.32). Additionally, different shapes one each layer can act complementary to each other to achieve performance at different frequencies.

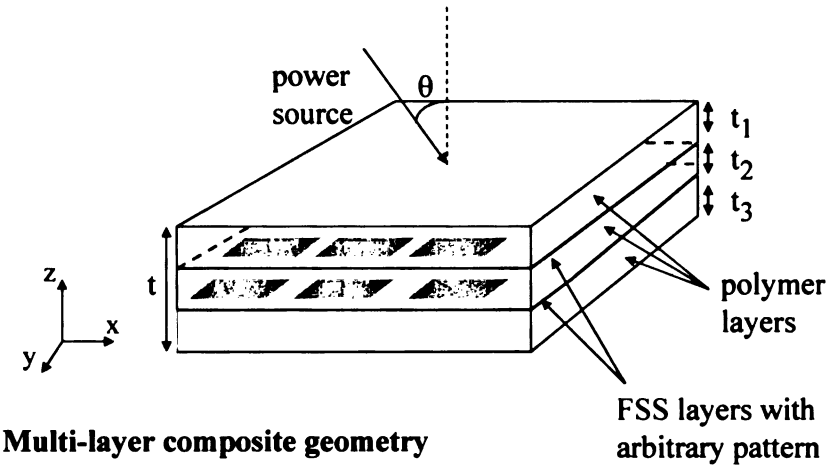

Figure 4.32. Multi-layer FSS composite geometry. The example shown here is for a composite with two FSS layers sandwiched within three polymer layers.

Two layer FSS composites were modeled to understand how the spacing between layers affected the composite properties and bandwidth, as compared to a single layer composite with the same element size and periodicity. The elements for the FSS layers were square loops with dimensions shown in Table 4.4 as Case S3. The thicknesses between the two FSS layers were varied and are seen in Table 4.7.

Table 4.7. Multi-layer FSS composites with varying polymer layer thicknesses.

Case	t_1 (mm)	t_2 (mm)	t_3 (mm)	t (mm)
M1	10	10	10	30
M2	12	6	12	30
M3	14	2	14	30
M1-a	8	8	8	24
M2-a	10	4	10	24
M3-a	11	2	11	24

The transmission characteristics were compared for each case for the total slab thickness of 30mm and 24mm, respectively, and these cases were compared to the single FSS case of the same thickness with the same FSS elements. Figure 4.33 shows the transmission power vs. frequency for these cases.

For Cases M1 and M1-a, when the layers between the two FSS arrays were spaced evenly, there was a grater deviation in transmission power from the single FSS case. This can be expected, since the closer spaced FSS layers would behave more closely to one single layer FSS. Since the two FSS arrays are spaced so closely, they behaved more like one layer of "thicker" FSS elements.

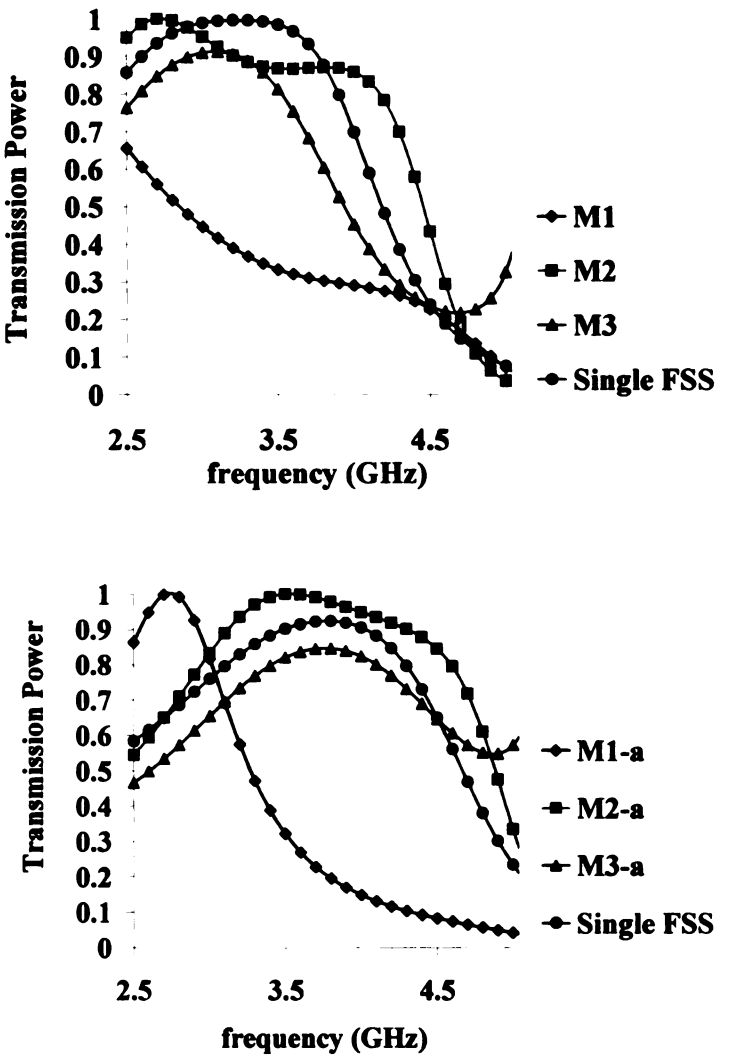

Figure 4.33. Transmission characteristics for multi-layer FSS composites.

The extracted effective permeability and permittivity for these cases are found in Figures 4.34 and 4.35 for the cases of multi-layer FSS composite of thicknesses 30 and 24 mm, respectively.

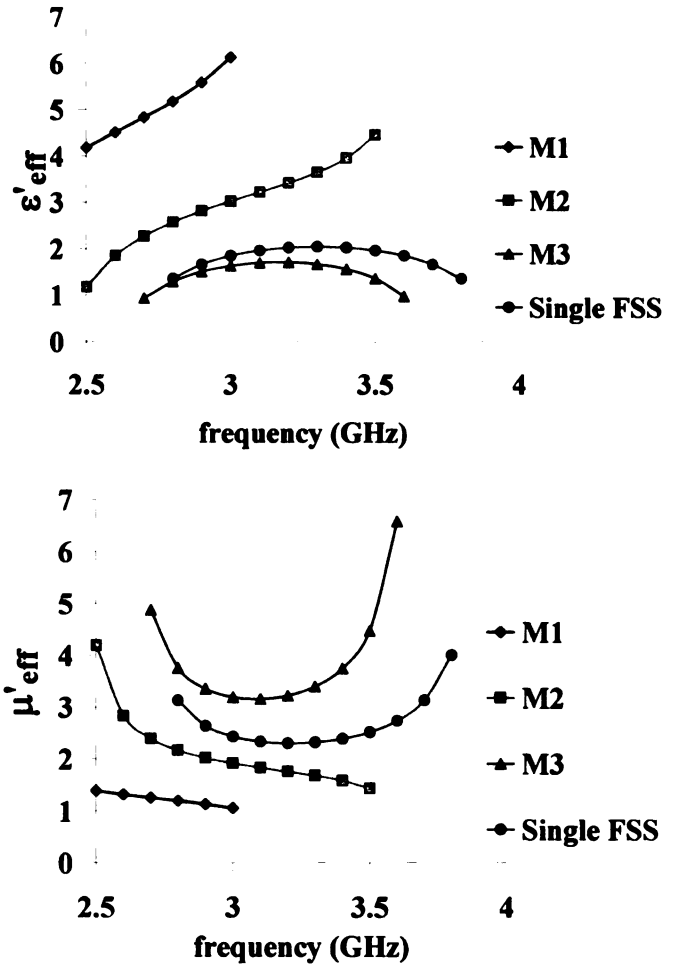

Figure 4.34. Effective properties for multi-layer FSS composites of total thickness 30mm. *Top*: Effective permittivity, ε'_{eff}, vs. frequency (GHz) and *Bottom*: Effective permeability, μ'_{eff}, vs. frequency (GHz).

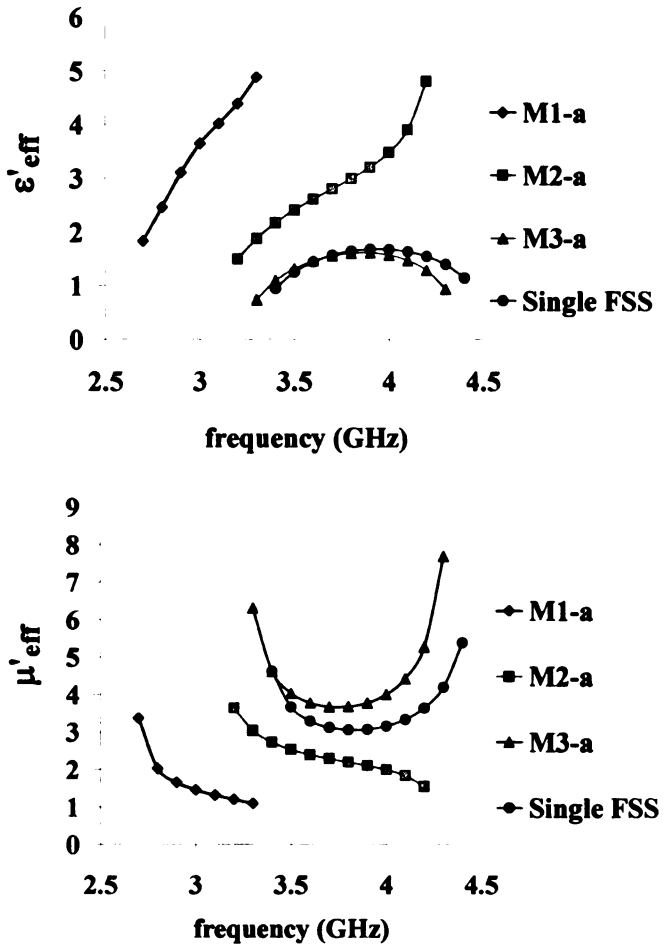

Figure 4.35. Effective properties for multi-layer FSS composites of total thickness 24mm. *Top*: Effective permittivity, ε'_{eff}, vs. frequency (GHz) and *Bottom*: Effective permeability, μ'_{eff}, vs. frequency (GHz).

For the cases with the two FSS layers spaced very close together, the effective permeability increased while the effective permittivity decreased. The reasoning for this is very similar to the reasoning behind the increase in effective permeability for very closely spaced elements on the FSS array. There is a greater mutual inductance and hence a greater permeability when the square loops are spaced closely in the z-direction, as well as in the y and x directions.

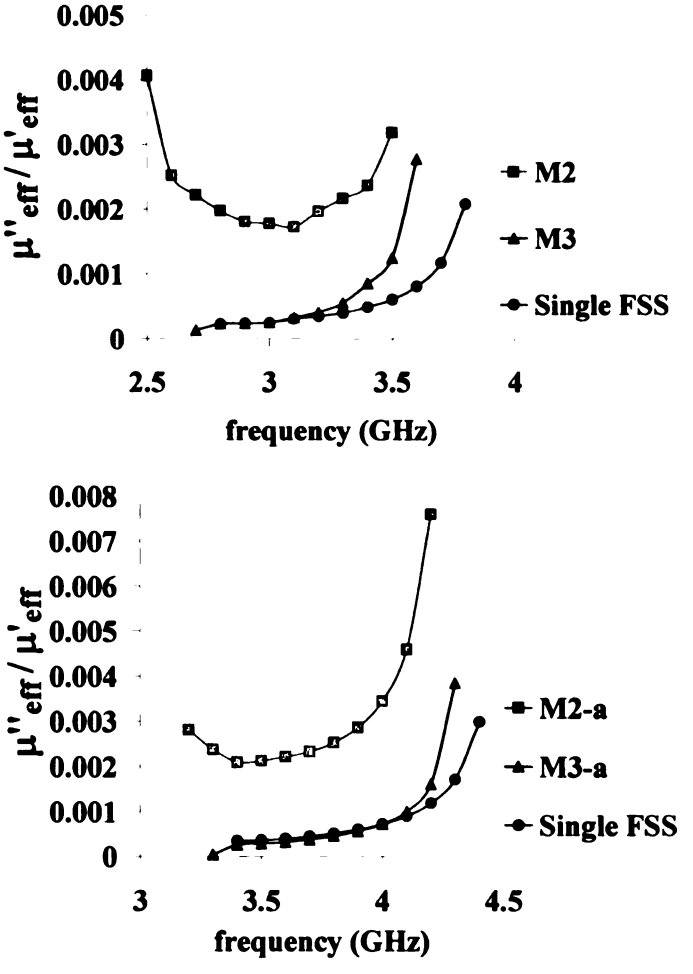

Figure 4.36. Permeability loss tangent, μ''_{eff}/μ'_{eff}, for multi-layer FSS composites, corresponding to Table 4.7.

The loss characteristics for the multi-layered samples can be found in Figure 4.36, which highlights the permeability loss tangents for the cases in Table 4.7. For all the multiple layer composites, the loss tangent was higher when compared to the single FSS. When comparing the various multi-layer composite configurations, loss was lower for the composites with closely spaced FSS layers.

4.6 FSS Layered Composite Fabrication and Characterization

Composites were fabricated with layers of periodic metallic arrays to incorporate the idea of frequency selective surfaces into the magneto-dielectric design. The fabrication and characterization efforts were divided into three elements: i) patterning the FSS arrays, ii) making the sandwiched FSS composite, and iii) characterizing the reflection and transmission for the composite.

4.6.1 FSS Element Patterning

Some techniques that can be used to achieve the patterning necessary for the FSS array fabrication include contact printing, photolithography, or machining shapes. For the materials and geometries for the composites modeled so far, photolithography was chosen as it was the simplest fabrication technique. Two different approaches were utilized for the fabrication process: the first was to pattern thin polyethylene films and sandwich them between the outer epoxy polymer layers using layer by layer curing under vacuum, while the second was to pattern the elements directly on the first layer of epoxy and then cast the subsequent second or third layers atop the first. For both the approaches, the same technique was used to pattern the FSS elements. The photolithography process is a well known and widely used process; this method is highlighted in Figure 4.37 [69].

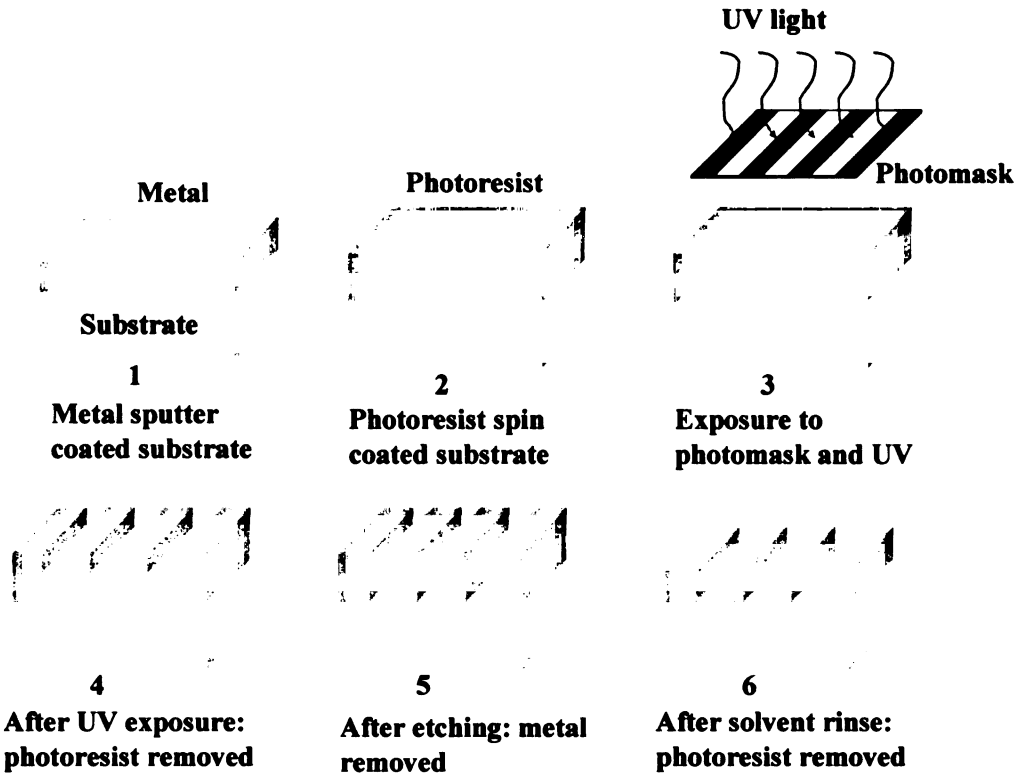

Figure 4.37. Photolithography process for patterned arrays.

In step 1, a layer of silver was coated on the substrate (either the polyethylene film or epoxy layer) using a magnetron sputtering device. The thickness of the silver was kept at approximately 100 nm for each sample. The sample, now consisting of a metal film on a polymer substrate, was placed on a spinner; positive photoresist was applied in step 2, while the sample was spun at high speed, resulting in a uniform thin film of photoresist on the sample surface. During step 3, a mask of ink on transparency or metal on glass was placed flush against the sample which is then exposed to UV light. The light can penetrate the glass only in the places where ink was present, exposing the positive photoresist to UV in these places. The sample was placed in a developer solution in step 4, which washed away the photoresist in the places where it was exposed to the UV light.

The rest of the photoresist remained in place to protect the metal film from the etchant. The sample was placed in a metal etchant solution during step 5. The etchant can only reach the metal that was not covered by photoresist; therefore, this metal was removed and the rest remains. The etchant chosen to remove silver was a potassium iodide/iodine solution which was known to remove silver easily. At this point the pattern on the mask has been etched into the metal film. Lastly in step 6, the remaining photoresist was removed by placing the sample in a solvent solution. The sample was cleaned thoroughly with de-ionized water [69]. Figure 4.38 shows an example of the square loop elements and square loop slot elements etched on a polyethylene film.

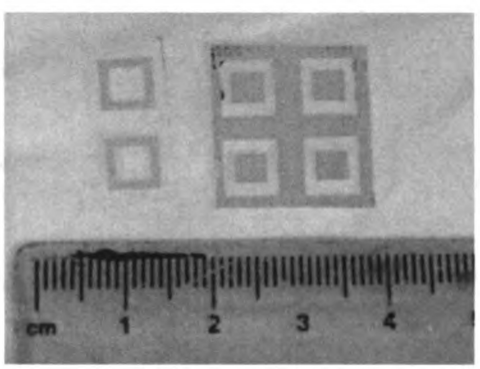

Figure 4.38. Square loop slots and square loop silver elements etched on polyethylene films.

Similarly, the square loop and hexagonal elements were etched on a silver coated epoxy substrate layer and can be seen in Figure 4.38.

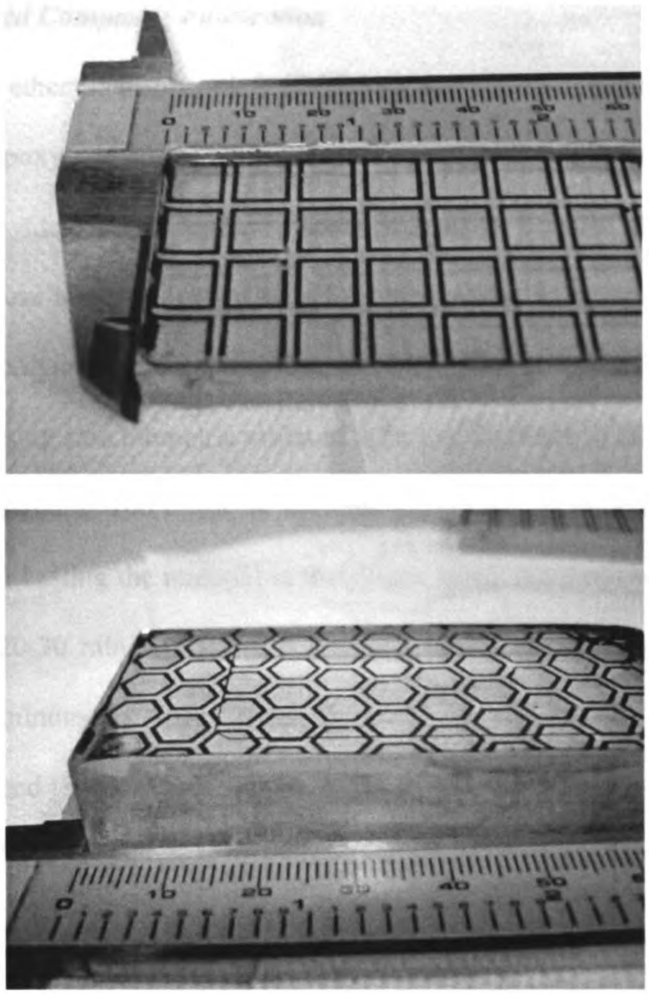

Figure 4.39. Square loop (top) and hexagonal loop (bottom) FSS elements patterned on an epoxy substrate (scale in mm).

By patterning the FSS elements directly on the first epoxy layer, problems that would conventionally arise in the sandwiching/layering process can be eliminated. The FSS layer would have excellent contact with the polymer layers and would lay horizontally aligned to the substrate.

4.6.2 FSS Layered Composite Fabrication

Diglycidyl ether of bisphenol A (DGEBA) and diaminodiphenyl sulfone (DDS) were used as the epoxy and curing agent, respectively, for the polymer layers of the FSS sandwiched composites. This epoxy system was used because the laboratory had previously used these materials extensively for other works, so the knowledge base was strong. For the polymer layering process, DGEBA was mixed with the appropriate amount of DDS (using stoichiometric ratios of 2.79:1 of DGEBA to DDS, by mass). The mixture was de-gassed at 100°C for 30 minutes to remove air bubbles from the epoxy before curing; after casting the material in the silicon mold, the mold and epoxy were de-gassed again for 20-30 minutes before curing at 146°C. The total length of cure was approximately 90 minutes for fully cured layers.

As described earlier, two approaches were used to fabricate the layered composite. For the first approach, the patterned polyethylene film was placed on the partially cured DGEBA/DDS layer with compression under vacuum for 30 minutes before the following DGEBA/DDS layer was cast and cured. Problems with this approach arose; it was very difficult to keep the FSS film horizontal (180°), and there was poor contact between the film and the epoxy interface. Due to these difficulties, the second approach was favored for composite fabrication.

The fully cured epoxy layer was coated with silver and patterned using the technique described earlier (see Figure 4.38). This layer was then placed in the mold and de-gassed with the epoxy mixture for 30 minutes before curing the secondary layer to create the final FSS sandwiched composite. Samples were void-free and the interface allowed for good contact between the FSS and epoxy since it was coated directly on the

surface. The final composite was polished using a sanding machine so corners had a smooth finish.

4.6.3 FSS Composites Characterization in a Waveguide

The fabricated FSS composite samples were tested in a calibrated WR-90 S-parameter measurement setup shown in Figure 4.40.

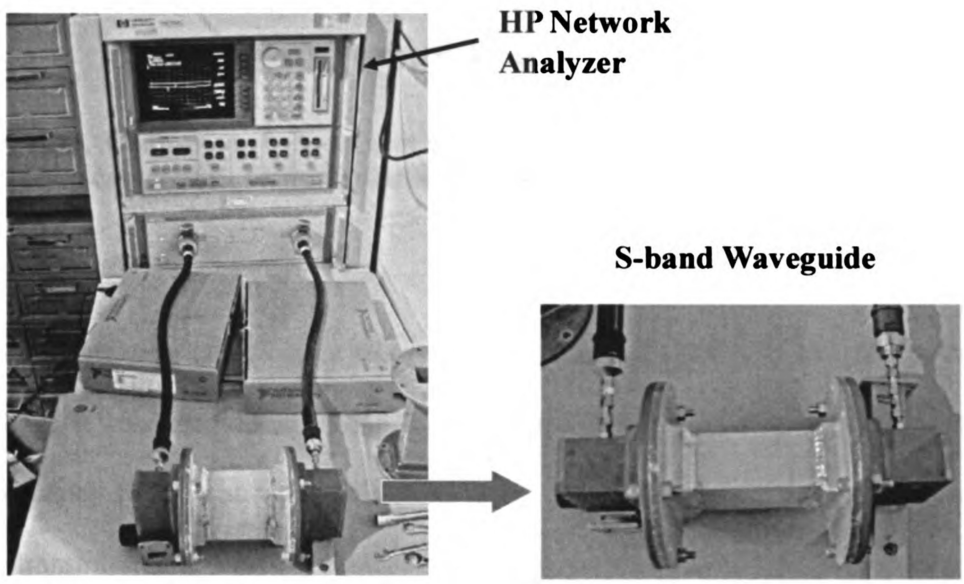

Figure 4.40. Set-up for waveguide measurement of FSS layered composites.

The waveguide was a standard size S-band waveguide (2.4-4.0GHz) with dimensions of 7.2x3.4 cm. The S-parameters were measured during a frequency sweep and were compared to simulated results. For the case H2 (hexagonal loops in Table 4.5), with epoxy as the polymer layers (total thickness = 3cm), the transmission characteristics are shown in Figure 4.41.

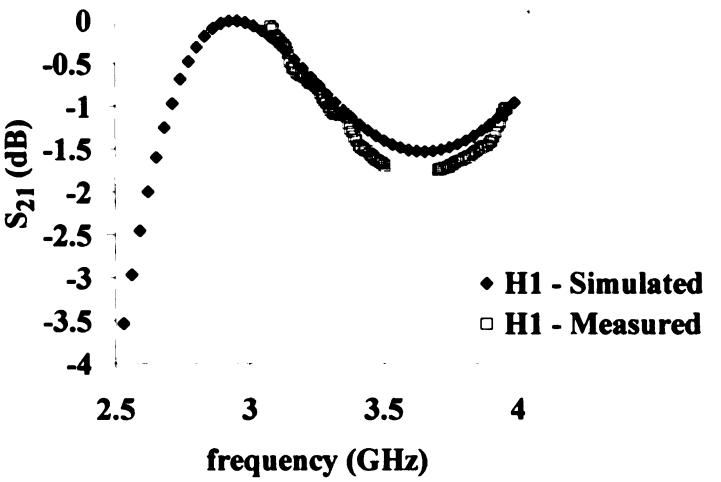

Figure 4.41. Comparison between simulated and measured results for hexagonal loops FSS layered composite. Transmission magnitude, S_{21} (dB), vs. frequency (GHz).

Measurements were taken over a frequency range of 2.4-4GHz, with 801 data points for sampling. It was noted during calibration and measurement that there were two points on the frequency sweep with uncharacteristic peaks – around 2.8 and 3.5 GHz. These spikes in the transmission and reflection spectrum created portions of the frequency sweep that were not usable for comparison to simulated data. For this reason, the portions from 3-3.5 GHz are shown here for comparison. Some points beyond 3.7GHz were also used for comparison (as seen in Figure 4.41). These spikes in the spectrum could be due to instrumentation error, specifically from the two chargers connected to the network analyzer which can degrade in accuracy over long time periods. There could also be a slight mismatch in reflection, causing the spikes at the corresponding frequencies.

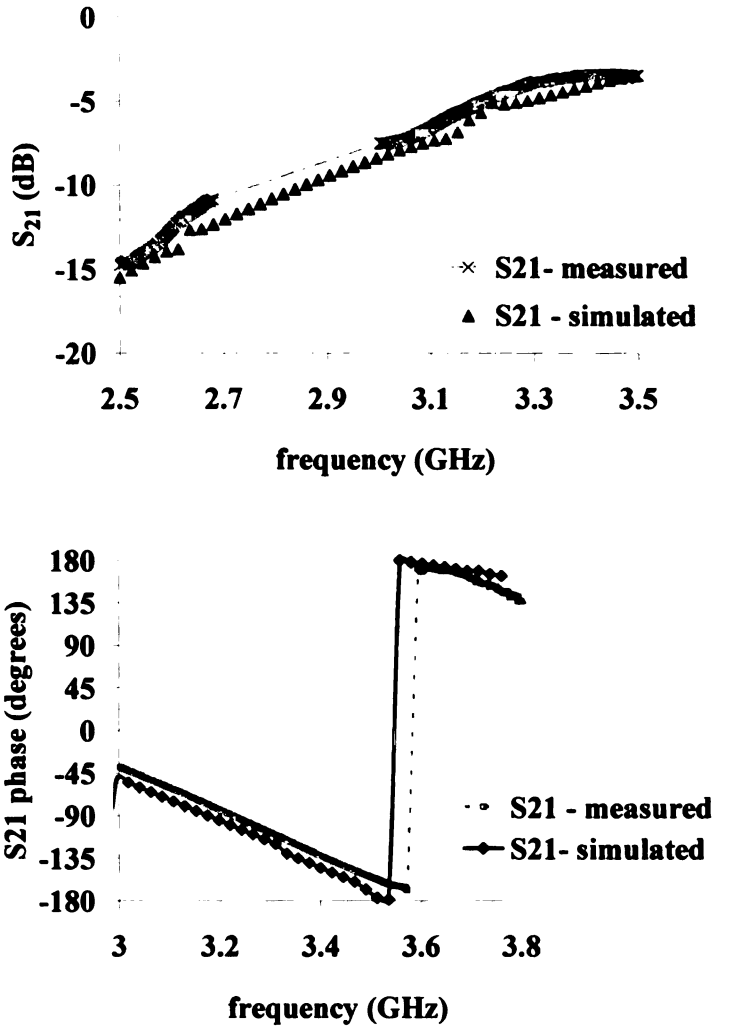

Figure 4.42. Comparison between simulated and measured results for square loop FSS layered composite. *Top*: S_{21} (dB) vs. frequency (GHz) and *Bottom*: S_{21} phase (degrees) vs. frequency (GHz) for Case S3 (Table 4.4).

The measured portions of the reflection and transmission correlated fairly well to the simulated results. The noted discrepancy could be due to the samples which were partially cracked when placed into the waveguide; also centering the samples within the device could be inaccurate, leading to shifts in frequency response.

4.7 Design Alternatives

4.7.1 High Frequency Operation

The original objective for final properties was achieved using a simple FSS layered composite design; however, for applications of these materials, optimization would be necessary. The thickness of the material can be reduced by adding multiple layers or changing the dielectric properties of the polymer material. If the thickness of the material was reduced while still using epoxy as the material for the polymer, the performance could be enhanced over a higher frequency bandwidth, since wavelength depends on frequency. Two cases were analyzed in order to illustrate this effect. Case S1 from Table 4.4 was modeled with the thickness reduced to 20mm and 10mm. Figure 4.43 and Figure 4.44 show the effective properties for both cases.

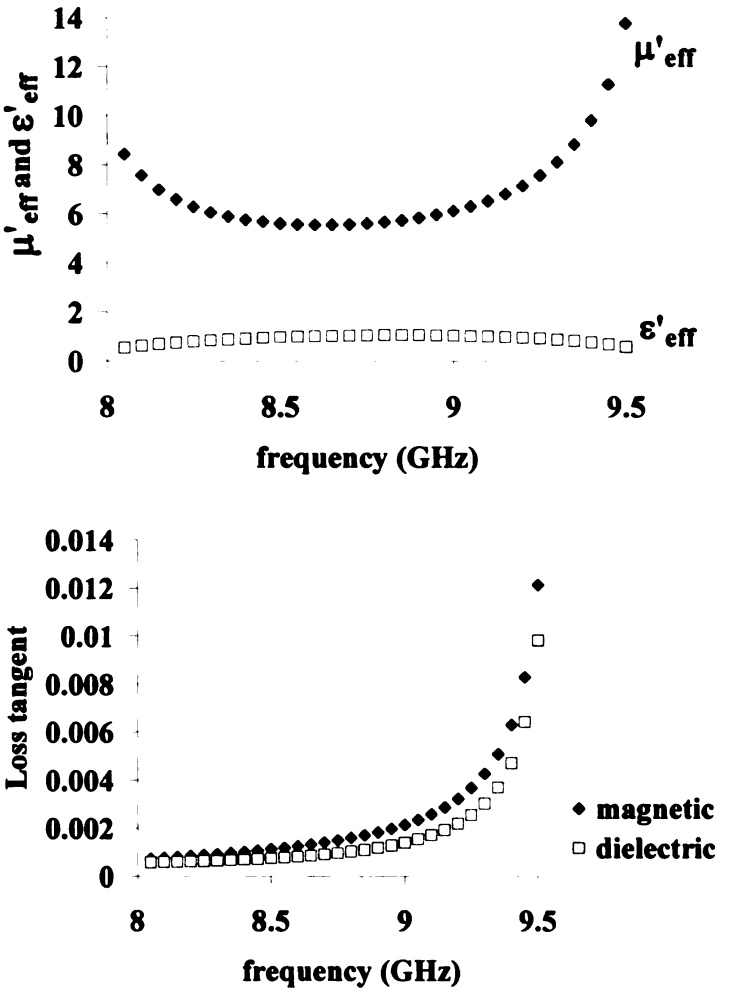

Figure 4.43. High frequency effective properties for square loop FSS composite (total thickness = 10mm). *Top*: Effective permittivity and permeability, ε'_{eff} and μ'_{eff}, vs. frequency (GHz) and *Bottom*: Magnetic and dielectric loss tangent vs. frequency (GHz).

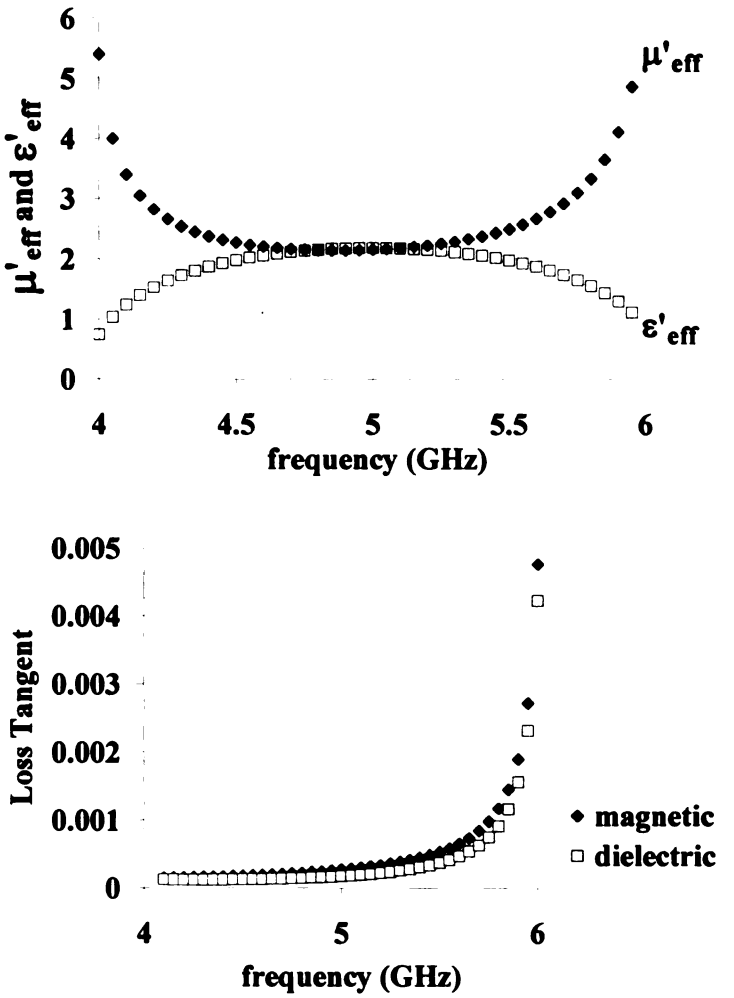

Figure 4.44. High frequency effective properties for square loop FSS composite (total thickness = 20mm). *Top*: Effective permittivity and permeability, ε'_{eff} and μ'_{eff}, vs. frequency (GHz) and *Bottom*: Magnetic and dielectric loss tangent vs. frequency (GHz).

Even with one layer of square loop elements, it was noted that permeability was increased at higher frequencies for thinner composites. Fabricated samples would be analyzed in an F-band waveguide (for 20mm samples) capable of measurements up to 6GHz.

4.7.2 Nanoparticle Reinforcement

The bandwidth of operation could be further improved by incorporating some of the ideas discussed in Chapter 3. For instance, at low frequencies, the permeability could be enhanced by using a mixture of magnetic particles (rods, flakes, etc), at low concentrations, to ensure an easily achieved uniform dispersion; whereas, at higher frequencies, the FSS arrays can be used to further enhance the permeability. The goal here would be to co-design the layers in such a way that they would behave complementary to each other to cooperatively meet the design objective, ultimately improving the bandwidth and performance.

4.8 Conclusions and Outlook

Frequency selective surface layers were successfully designed to act as "inductive inclusions" within a polymer matrix, thereby resulting in an engineered, artificial magnetic material with controlled properties at frequencies greater than 2.5 GHz. The novelty of these designs is that the permeability and permittivity are enhanced *to the same extent*, with permittivity less than permeability in some cases, which greatly improves the ease of impedance matching.

Structure-property relationships were developed for FSS elements and characteristics of the composite geometry to relate the effective properties. Composites were fabricated and characterized in a waveguide to compare the reflection and transmission behavior. The approach presented in this chapter was successful in reaching the original objective; however, before these designs can be implemented in specific

applications, further work would be required. In addition to optimization, design alternatives could be considered (as shown in Section 4.7) in order to apply these designs to an actual application.

CHAPTER 5 : Microwave Applicator Design for Activated Carbon

5.1 Background

5.1.1 Gasoline Emissions Control and Activated Carbon

Emissions from a vehicle include hydrocarbons, nitrogen oxide, carbon dioxide, and carbon monoxide. These emissions can be controlled in various ways; one such technique involves capturing the evaporated vented vapors and eliminating them. Vapors from the fuel tank inside the vehicle are channeled through canisters that have an adsorbent (i.e. activated carbon). After the adsorption process within the canister, the vapors desorb from the adsorbent while the engine is running and are burned as they are drawn into the engine [70].

Activated carbon is often used as an adsorbent for these applications involving fuel emissions. The primary raw material for activated carbon would be any organic material with high carbon content (i.e. wood, coal, coconut shell). The activated carbon has a very large surface area per unit volume, and the material is very porous allowing adsorption to take place. Pollutants in the air easily latch the porous surface of these adsorbents [7-9]. In the past, the activated carbon that had adsorbed to its capacity was discarded. In order to increase efficiency, companies have been motivated to develop methods to regenerate the activated carbon – i.e. thermal regeneration in vehicles (as described earlier). In hybrid vehicles, however, the gasoline engine is not running for large fractions of time; thus, alternative measures must be considered for the heating of the activated carbon. So, in the case of hybrid vehicles, the desorbed vapors will

condense and go back into the gas tank; therefore, the composition of the gasoline will be consistent for longer periods of time.

5.1.2 Microwave Heating of Activated Carbon

Current progress has shown that microwave heating is a promising alternative method for processing polymers and composites [72-88]. Microwave heating is primarily accomplished by coupling electromagnetic fields into the material via ohmic loss. This loss is often characterized by temperature and frequency dependent dielectric properties. The advantages seen for microwave heating and processing can be of use in other applications. For example, microwave energy has been used to regenerate NO_x saturated carbon adsorbents [8]; microwaves penetrate dielectric materials, so the maximum temperature of the material is dictated by the rate of heat loss and power applied. The efficiency of using microwave energy to regenerate AC has been investigated with promising initial results [7-9]. Microwave radiation allowed for the carbon to be recycled and reused a number of times, resulting in an increased surface area and subsequently a higher value for the carbon as an adsorbent. A thorough understanding of the heating mechanism for AC by microwave energy is of great importance to furthering the development of new techniques for AC regeneration.

When microwave energy is applied to the saturated AC, the carbon heats up and the adsorbed hydrocarbons react with the carbon – resulting in a reduced weight of the sample. By measuring the change in weight of the sample, the effectiveness of the regeneration can be measured. The heating mechanism of the AC will directly be related to the material properties as characterized in the first objective. Once the heating

mechanism is determined, the safety of the microwave regeneration can be evaluated. The temperature profile for a hypothetical sample can be determined using analytical models. Preliminary experiments will provide insight into the temperature distribution during microwave heating.

Investigating the composition of the carbon pellets will be crucial, in order to understand what causes the rapid heating with microwaves. The loss factor must be evaluated for each material; it should be determined whether the loss factor would be dependent on the polarity and the concentration of the adsorbed solvent. The higher the loss factor, the greater the heat-up rate for that material. Even with low-loss solvents, it should be expected that adsorbents with a higher loss factor will regenerate more quickly [7-9]. Thorough analysis into the loss factor as well as dielectric constant for all these materials will provide a basis for evaluation of the feasibility of this concept.

5.1.3 Microwave Mechanisms and Materials Interactions

Materials are classified into conductors, semiconductors and dielectrics according to their electric conductivity. Conductors contain free charges, which are conducted inside the material under alternating electric fields so that a conductive current is induced. Electromagnetic energy is dissipated into the materials while the conduction current is in phase with the electric field inside the materials. Dissipated energy is proportional to conductivity and the square of the electric field strength. Conduction requires long-range transport of charges.

In dielectric materials, electric dipoles, which are created when an external electric field is applied, will rotate until they are aligned in the direction of the field.

Therefore, the normal random orientation of the dipoles becomes ordered. These ordered polar segments tend to relax and oscillate with the field. The energy used to hold the dipoles in place is dissipated as heat into the material while the relaxation motion of dipoles is out of phase with the oscillation of the electric field. Both the conduction and the electric dipole movement cause losses and are responsible for heat generation during microwave processing. The contribution of each loss mechanism largely depends on the types of materials and operating frequencies. Generally, conduction loss is dominant at low frequencies while polarization loss is important at high frequencies. Most dielectric materials can generate heat via both loss mechanisms [10-11].

There are mainly four different kinds of dielectric polarization. Electron or optical polarization occurs at high frequencies, close to ultraviolet range of electromagnetic spectrum [10]. It refers to the displacement of the electron cloud center of an atom relative to the center of the nucleus, caused by an external electric field. When no electric field is applied, the center of positive charges (nucleus) coincides with the center of negative charges (electron cloud). When an external electric field is present, the electrons are pushed away from their original orbits and electric dipoles are created. Atomic, or ionic, polarization occurs in the infrared region of the electromagnetic spectrum. This type of polarization is usually observed in molecules consisting of two different kinds of atoms. When an external electric field is applied, the positive charges move in the direction of the field and the negative ones move in the opposite direction. This mainly causes the bending and twisting motion of molecules. Orientation, or dipole alignment, polarization occurs in the microwave range of the electromagnetic spectrum. Orientation polarization is usually observed when dipolar or polar molecules are placed

in an electric field. At the presence of external electric field, the dipoles will rotate until they are aligned in the direction of the field. The dipolar rotation of molecules is accompanied by intermolecular friction, which is responsible for heat generation. Orientation polarization is fundamentally different from electronic and atomic polarization. The latter is due to the fact that the external field induces dipole moments and exerts displacing force on the electrons and atoms, while the orientation polarization is because of the torque action of the field on the pre-existing permanent dipole moments of the molecules. Lastly, interfacial, or space charge, polarization occurs at low frequencies, e.g. radio frequency (RF). It is a fundamental polarization mode in semiconductors. This type of polarization is caused by the migration of charges inside and at the interface of dielectrics under a large scale field.

5.2 Dielectric Characterization

5.2.1 Dielectric Properties, Measurement, and Microwave Effects

Most polymers and composites are non-magnetic materials. The electromagnetic energy loss is only dependent on the electric field. Incident electromagnetic fields can interact with conductive and nonconductive materials. The fundamental electromagnetic property of nonmagnetic materials for microwave heating and diagnosis is the complex dielectric constant:

$$\varepsilon = \varepsilon' - j\varepsilon'' \tag{5.1}$$

The real part of the complex dielectric constant is dielectric constant – the higher the polarizability of a molecule, the larger its dielectric constant. The imaginary part is

dielectric loss factor, which is related to energy dissipated as heat in the materials. The ratio of the effective loss factor to the dielectric constant is defined as the loss tangent, which is also commonly used to describe dielectric losses:

$$\tan \delta_{eff} = \frac{\varepsilon''_{eff}}{\varepsilon'_r} \tag{5.2}$$

When introduced into a microwave field, materials will interact with the oscillating electromagnetic field at the molecular level. Different materials will have different responses to the microwave irradiation. Microwave heating of conductive materials, such as carbon fibers and acid solutions, is mainly due to the interaction of the motion of ions or electrons with the electric field. However, conductors with high conductivity will reflect the incident microwaves and can not be effectively heated.

The fields attenuate towards the interior of the material due to skin effect, which involves the magnetic properties of the material. The conducting electrons are limited in the skin area to some extent, which is called the skin depth, d_s. Defined as the distance into the sample, at which the electric field strength is reduced to 1/e, the skin depth is given by [10-11].

$$d_s = \frac{1}{\left(\frac{1}{2}\omega\mu_o\mu'\sigma\right)^{\frac{1}{2}}} \tag{5.3}$$

where ω is the frequency of the electromagnetic waves in rad/sec, μ_0 ($=4\pi 10^{-7}$ H/m) is the permeability of the free space, μ' is the relative permeability, and σ is the conductivity of the conductor in mhos/m. For example, $\sigma = 7\text{x}10^4$ mhos/m and $d_s = 38.4$ μm for graphite at 2.45 GHz in a free space. The skin depth decreases as frequency

increases. For a perfect conductor, the electric field is reflected and no electric field is induced inside a perfect conductor at any frequency. Therefore, no electromagnetic energy will be dissipated even though the conductivity of the perfect conductor is infinite [10-11].

During microwave processing, the dielectric properties of materials change as a result of heating and reaction. This affects the electrical field strength and power absorption in the materials. The change in electric field and power absorption in turn affects the temperature and extent of reaction inside the materials. Thus, the modeling of microwave heating is a coupled non-linear problem, which involves Maxwell's equations for solving the electric field strength, a heat transfer equation for obtaining the temperature distribution inside the material, and a reaction kinetic equation for calculating extent of reaction.

5.2.2 Dielectric Properties of Activated Carbon

The dielectric constant and loss factor were measured for unsaturated and saturated activated carbon pellets as a function of temperature at 2.45 GHz. A low-power swept-frequency diagnostic system was used to measure the shift frequency and half-power bandwidth for heated samples, with measurements taken during free convective cooling of the samples at 2.45 GHz [60]. Inversion methods were used to convert these measurements to the dielectric constant and loss factor. The dielectric constant was measured for both saturated and unsaturated carbon as a function of temperature.

Also, the effect of varying morphologies of unsaturated carbon on the overall dielectric properties was analyzed. Three different samples were measured for the

unsaturated carbon – loose powder, bulk pellets, and compressed powder (Figure 5.1). Dielectric properties often depend on frequency as well as temperature and composition; for this reason, the dielectric constant and loss factor were measured for unsaturated compressed carbon powder from 1 – 1000 MHz by using an impedance analyzer with dielectric test fixture, as discussed earlier.

The bulk carbon pellets (both saturated and unsaturated) were ground using a pestle and mortar into a fine powder. Compressed powder samples were compressed by using a small percent of epoxy to act as a binder; the percent of epoxy required as a binder remained below 10% by volume. Figure 5.1 shows the various activated carbon morphologies for this study.

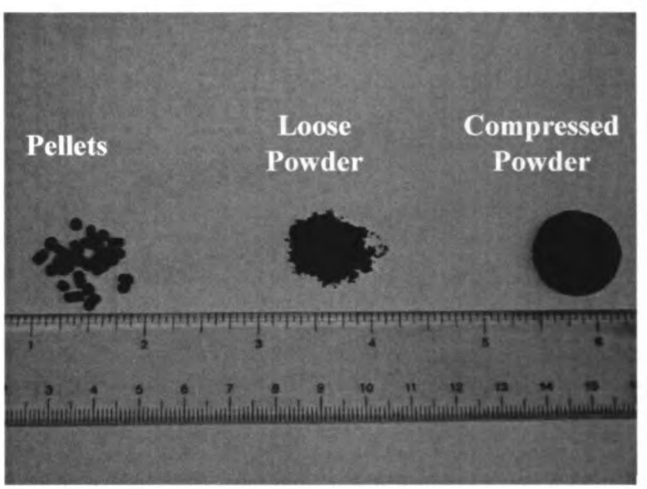

Figure 5.1. Activated carbon morphology: pellets, loose powder, and compressed powder disk.

The loose powder samples and compressed powder samples were analyzed, in addition to the bulk un-saturated carbon pellets. Figure 5.2 shows a summary of the relationship

between dielectric constant and temperature for both saturated and unsaturated bulk carbon pellets.

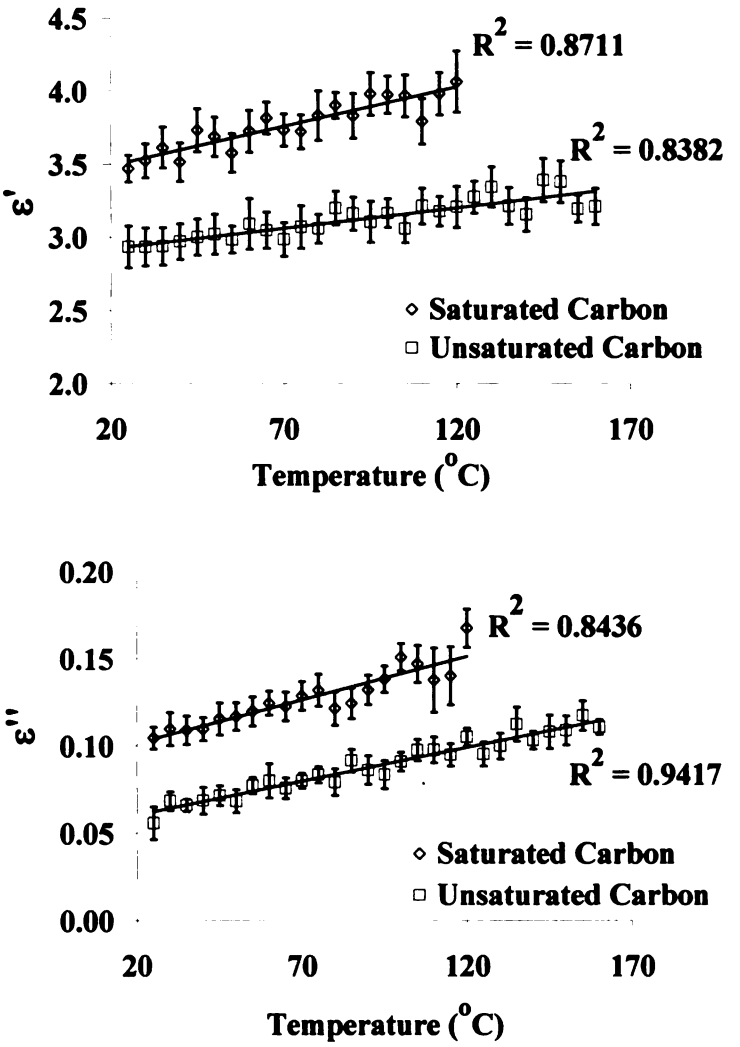

Figure 5.2. Dielectric properties for saturated and unsaturated activated carbon pellets as a function of temperature. *Top*: Dielectric constant, ε', vs. temperature (°C) and *Bottom*: Dielectric loss factor, ε'', vs. temperature (°C).

The dielectric loss factor is a clear indicator of how easily a material can heat in the microwave, as discussed earlier. In the case of microwave heating of activated carbon, higher loss factors are desirable since that would indicate ideal heating in a microwave system. Figure 5.2 highlights the results for the investigation into the dielectric loss factor. The saturated bulk pellets had higher dielectric loss than the unsaturated bulk pellets, perhaps due to the higher density.

Table 5.1 summarizes the key results – dielectric constant and dielectric loss factor, along with the corresponding standard error – for these studies (at 2.45 GHz). The unsaturated loose powder and compressed powder resulted in similar dielectric constants, which were both higher than the bulk pellets. The unsaturated loose and compressed powders also had increased loss compared to the unsaturated bulk pellets. In comparison, the increase in loss factor from compressed to loose powder was even steeper than the change in dielectric constant.

Table 5.1. Dielectric constant, dielectric loss factor, and average standard error for activated carbon. Ranges of values are shown for unsaturated and saturated carbon pellets, unsaturated loose powder, and unsaturated compressed powder, corresponding to the temperature range of 25°C – 150°C.

Morphology	**ε'**	**Standard Error (ε')**	**ε''**	**Standard Error (ε'')**
Pellets, *saturated*	3.72-4.98	0.135	0.109-0.234	0.0094
Pellets, *unsaturated*	2.81-3.31	0.123	0.067-0.123	0.0067
Loose powder, *unsaturated*	3.45-4.59	0.136	0.088-0.220	0.0082
Compressed powder, *unsaturated*	3.71-4.67	0.138	0.152-0.328	0.0086

The dielectric test fixture measured the admittance of the sample while held between two electrodes within the fixture as seen in Figure 3.6 from 1MHz to 1GHz. The conductance (related to the dielectric loss) and the capacitance between the electrodes are measured, and the real and imaginary parts of the permittivity can then be calculated, using these measured values [59]. The results from this analysis are found in Figure 5.3.

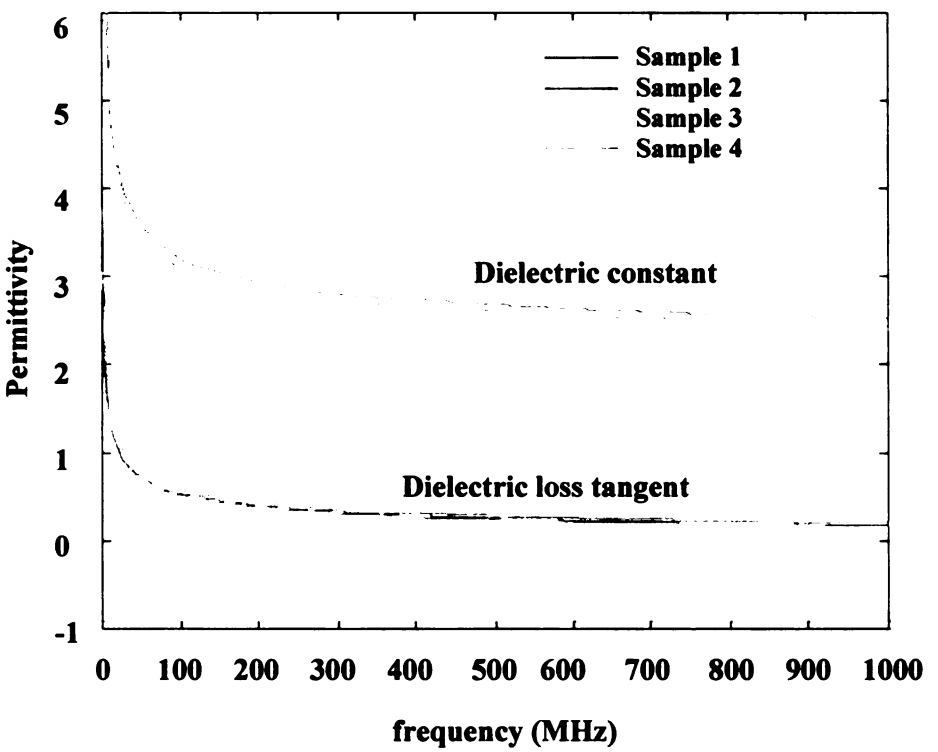

Figure 5.3. Permittivity vs. frequency (MHz) for unsaturated activated carbon disks.

As can be seen from these results, the dielectric constant is very similar to that measured with the swept frequency diagnostic system; the dielectric loss factor is slightly higher

than the value measured with the other method. This could be attributed to having the epoxy addition as a binder.

5.3 Microwave Applicator Design

5.3.1 Design Rationale

Several considerations were taken into account when designing the microwave heating applicator; ultimately, a transmission line design was chosen over a single (or multi-) mode cavity. Cavities are hollow and metallic, designed to be resonant. Theoretically, at the resonant frequency, the electric (and magnetic) field intensity is infinite regardless of the microwave source power, which cannot be realized in practice. A figure-of-merit for a resonant cavity is the quality factor (e.g. the Q of the cavity). The Q-factor is defined as:

$$Q = 2\pi \frac{\text{energy stored}}{\text{energy lost per cycle}} \tag{5.4}$$

A high Q implies that the resonant mode (e.g. the characteristic field pattern that can be supported within the cavity, at a given frequency, and satisfy all the necessary boundary conditions) stores all the energy put into the cavity by the source since very little is lost as heat. A superconductor can achieve quality factors on the order of10^{11}, while copper cavities can have a Q on the order of 5,000. The Q is directly proportional to the square root of the electrical conductivity. Hence, for a drum cavity, the theoretical Q is given by

$$Q = \lambda \sqrt{\pi f \mu_0 \sigma} \frac{2.405}{2\pi(1 + a/d)} \tag{5.5}$$

where f is the frequency, λ is the wavelength, μ_0 is the free-space permeability, σ is the electrical conductivity, a is the drum radius, and d is the drum length. Hence, the higher the conductivity, the higher the Q will be. Better electric conductors (such as silver or gold) will result in a higher Q for a given design. The reason high Q cavities are desirable is that for a given input power, the peak electric field will be higher as shown in Equation 5.6.

$$|E(\omega)|^2 \propto \frac{1}{(\omega - \omega_0 - \Delta\omega)^2 + (\omega/2Q)^2} \tag{5.6}$$

where $\omega = 2\pi f$ is the radial frequency, ω_0 is the resonant frequency of the cavity, and $\Delta\omega$ is the half-power bandwidth of the cavity. Note that the bandwidth $(\Delta\omega)$ is also inversely proportional to the electrical conductivity. For a perfect cavity, the Q is infinite, the bandwidth is zero; therefore, at the resonant frequency, the electric field strength is infinite [11].

One of the consequences of a highly resonant cavity is that its performance is strongly dependent on the permittivity of the material in the cavity; if a highly resonant cavity were used for this case, changes in the carbon material due to physical changes (e.g. density of the granules) or chemical mixture changes (e.g. loading by fuel) may "de-tune" the cavity sufficiently so that it becomes inefficient for heating the carbon/fuel mixture. This de-tuning is represented by a shift in the resonant frequency. With such a shift, the impedance of the cavity, as seen by the microwave source, is changed resulting in reflection at the input port keeping a fraction of the microwave power from being used to heat the material. In addition, a single-mode cavity (most efficient type) has a field pattern with "hot-spots" defined by the mode and the material properties. These can lead

to inefficient heating. Alternatively, a waveguide can be used as the microwave applicator [10-11].

The idea for the coaxial waveguide set-up for heating activated carbon can be found in Figure 5.5. The resulting properties from the characterization discussed previously were used for the modeling calculations.

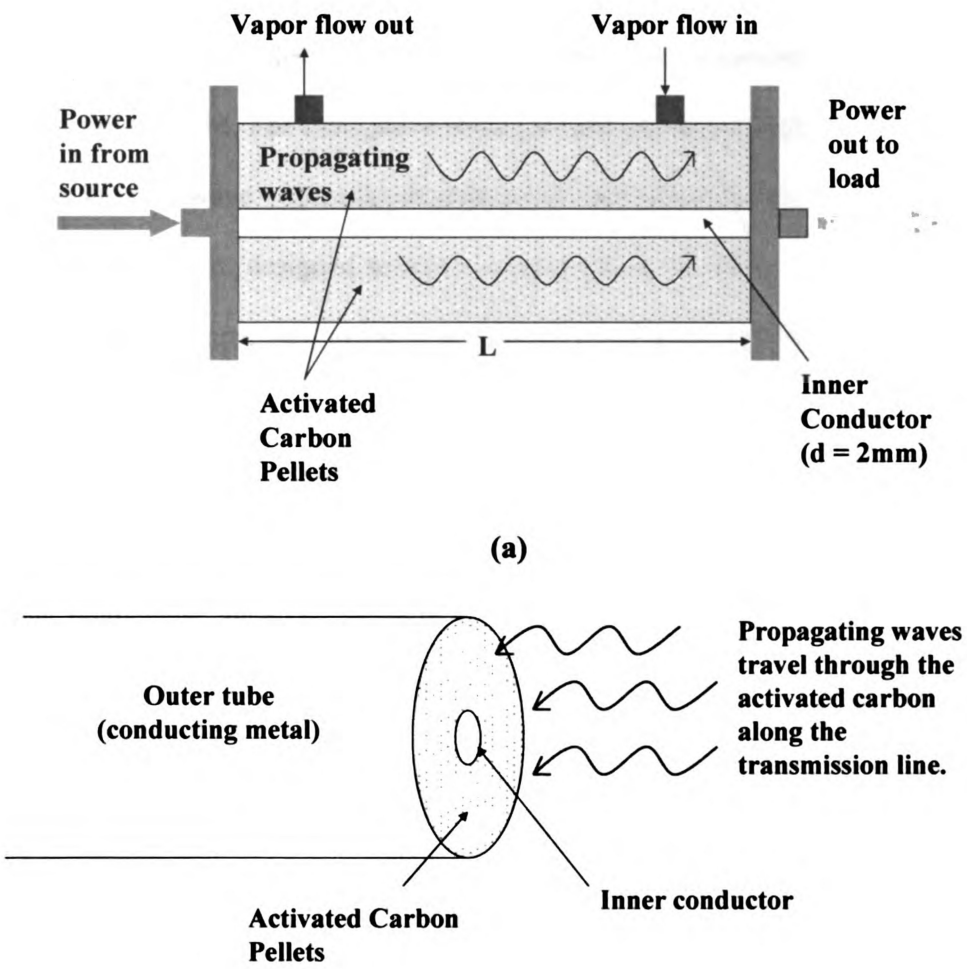

Figure 5.4. Design concept for transmission line heating device. (a) Coaxial waveguide set-up for activated carbon heating and (b) Cross-sectional view of coaxial waveguide.

As shown in Figure 5.4, a coaxial waveguide is constructed by an inner electric conductor of radius d and an outer electric conductor with radius $D > d$ separated by a dielectric filling (commonly air; however, a different dielectric such as carbon granules can be used). Impedance is the ratio of the voltage to the current (for an electric circuit) or alternatively the electric field strength to the magnetic field strength (for microwaves). A fundamental concept of microwave systems is that reflections of the wave occur at the location of impedance discontinuities. The greater the discontinuity, the greater the reflected field will be. For example, a short (or open) have the highest reflected wave – all of the incident wave – since the impedance of such a load is zero (or infinite) whereas most waveguides are designed to have an impedance of 50Ω. The microwave field travels from the source side to the load side. If the load is perfectly matched (e.g. the impedance of the load is identical to the impedance of the waveguide and source), then no reflected wave is present (e.g. wave propagation is unidirectional – left to right in Figure 5.4). If a reflected wave is present, it interacts constructively and destructively at various predictable locations along the waveguide; these interactions will change the ratio of the electric and magnetic field intensities at the source end will change with respect to the frequency (or filling material permittivity) leading to reflections (due to an unplanned impedance discontinuity) at the source end leading to inefficient heating and potential damage to the source. If no reflections exist, the impedance is only weakly dependent on either frequency or material fill. Since all sources exhibit frequency variations (with temperature, age, etc), some variation in frequency (not much) is expected in practice. Variations in material fill are expected since the carbon may

crumble, settle, etc; nevertheless, a coaxial waveguide applicator will be very tolerant of such practical changes in the device.

5.3.2 Design Results

The applicator design will included an activated carbon fill along with low-loss windows to contain the carbon. This design was based on computer simulated models (e.g. Ansoft HFSS) which were highly dependent on the material properties. It was decided to examine coaxial line designs to see if they could act as a load with minimal reflected power being returned to the source. To match the source, a coaxial line was designed with characteristic impedance of 50 Ω using the following equation (for non-magnetic materials such as carbon, air, and alumina)

$$Z_0 = \frac{1}{2\pi}\sqrt{\frac{\mu_0}{\varepsilon_0 \varepsilon_r}}\ln\left(\frac{D}{d}\right) \tag{5.7}$$

where D is the diameter of the outer conductor, d is the diameter of the inner conductor, μ_o is the permeability of free-space, ε_o in the permittivity of free-space, and ε_r is the permittivity of the carbon [10-11].

It can be seen that the characteristic impedance of a coaxial line is determined by the ratio of diameters of the inner and outer conductors and the material between the two conductors. The length of the line does not have an effect on the characteristic impedance. It is desirable to support only the fundamental, transverse electromagnetic (TEM), mode since (5.7) assumed a TEM mode. Higher-order modes may exist if the operating frequency exceeds the cut-off frequency of the waveguide. This cut-off frequency is given by

$$f_c = \frac{2c}{\pi\sqrt{\varepsilon_r}(D+d)} \tag{5.8}$$

As a consequence, the inner diameter (d) must be 8mm or less so the cutoff frequency is high enough to prevent higher order modes from propagating down the transmission line [11].

The loss of the carbon will absorb the power entering the coaxial line converting it into heat and thereby raising the temperature of the carbon. The amount of power absorbed by the carbon per unit length can be calculated by considering the loss tangent of the carbon (Equation 5.2), which is a measure of the loss of the material. Assuming that the wave is propagating from the reference position to a position L from that point, the field attenuation is given by

$$|E(L)| = |E(0)|e^{-\alpha_D L} \tag{5.8}$$

As can be seen, the field strength undergoes exponential decay as it propagates through a lossy material such as carbon. The attenuation coefficient (in dB/meter) [10] is given by

$$\alpha_D = 8.68588\frac{\pi\sqrt{\varepsilon_r}\tan(\delta)}{\lambda_0} \tag{5.9}$$

Figure 5.6 illustrates the relation between attenuation and line length. For a line length of approximately 780mm, 10 dB (90%) of the power was absorbed by the carbon. As a consequence, the load at the end of the waveguide (see the right side of Figure 5.4), can be a short (or open) without causing a substantial reflection. Larger loss factors will result in a higher attenuation coefficient and consequently higher attenuation as the wave propagates; accordingly, a shorter line length can be used as the material becomes increasingly lossy. However, as seen in Equation 5.7, the impedance of the waveguide

was dependent on the inverse square root of the complex permittivity. Since sources typically have no reactance by design, a lossy waveguide cannot be perfectly matched to a source without a reactive matching network; hence, excessive loss significantly complicates the microwave system design and the cost of each unit. Alternatively, a shorter line can be used if a matched load is put at the end of the line with the cost of reduced efficiency [10-11].

A transmission line was modeled using Ansoft's HFSS software, an industry standard full-wave electromagnetic solver, which was also used for the modeling discussed in Chapter 4. First, a transmission line with a carbon dielectric was simulated to verify the theoretical predictions. The magnitude of the electric field decayed as it propagated down the coaxial line, with the highest field strength near the source and the field strength near the load near zero. The power absorbed by a lossy dielectric, such as carbon is given by

$$P(z) = \frac{\omega \varepsilon''}{2} |E(z)|^2 \tag{5.10}$$

and so it is clear that more power is delivered to the carbon, raising the temperature locally, in regions where the field is greatest.

Using the coaxial transmission line design in the previous section, it was determined that placing a shorting plate on the far end of the transmission line can be used as the load. The shorting plate would cause reflection if the field has not been sufficiently attenuated prior to arriving at the load, thereby setting up a standing wave in the line. The loss due to carbon will attenuate the power, so a load of sufficient length would have minimal power be returned to the source. Measure of the reflected field (and

hence power which is proportional to the square of the field intensity) is the voltage standing wave ratios (VSWR). The VSWR is given by

$$\text{VSWR} = \frac{1+|\Gamma|}{1-|\Gamma|} \tag{5.11}$$

where Γ is the field reflection coefficient. For a short, $|\Gamma| = 1$ and so the VSWR is infinite while for a perfect match, $|\Gamma| = 0$ and so VSWR=1. Even with a line as short as 500mm, there was very little power being returned to the source (VSWR was below 2). A VSWR less than 2 is generally considered acceptable; however, some sources may have more stringent requirements [10].

The HFSS simulation of a line 500mm long with a shorting plate on the end resulted in a standing wave through the device, with areas of low and high field intensity. In a TEM transmission line, the electric field has only a radial component while the magnetic field have a θ-component (note that propagation is along the axial direction). With this in mind, if axial windows are cut in areas of low magnitude electric field, there would be minmal change to the field structure inside the line and little radiation. The width of these slits should be less than $\lambda/20$ or alternatively, the slit should be covered with a fine metallic mesh (similar to that used with microwave ovens).

Based on these results, it can be concluded that a 500mm shorted transmission line with carbon serving as a lossy dielectric could act as a load that will absorb almost all of the input power to prevent reflections damaging the power source and act as a heating element. Fuel will be able to enter the line via windows cut in specific places (shown in blue above) that will not interfere with the internal field structure. Since the power will not be able to radiate, all of the power that enters the system will have to be

converted to heat in the carbon dielectric. The majority of the power is absorbed in the first half of the transmission line near the feed point and is fairly uniform. The second half of the load does have some cold spots, but this is necessary to allow windows to be cut in the load to allow fuel to enter the heating element. If it is necessary to have a line shorter than 500mm a matched load could be placed at the end of a line of any length. This will absorb power preventing it from reflecting back and damaging the source. The load would also eliminate any hot spots that appear on the line. However, a load would increase the cost of the heating element and reduce the efficiency of the heating since some of the power will be absorbed by the load instead of the carbon.

5.3.3 Bench-top System Construction

Previous results from design calculations and simulations were used to determine the dimensions required for the inner and outer conductors (with diameters of 0.341" and 1.527", respectively). The flanges on either end of the outer conductor were welded in place, and a ridge was cut into the coax to N converters to allow for a perfectly centered fit in the outer conductor (see Figure 5.5). Mounting plates were machined to secure the converters to the flange on the outer conductor. In order to allow for air flow in future experiments, slots were cut on both ends of the outer conductor; also, holes were cut along the length for temperature measurement with fluoroptic probes. Figure 5.6 below shows a schematic of the machined outer conductor.

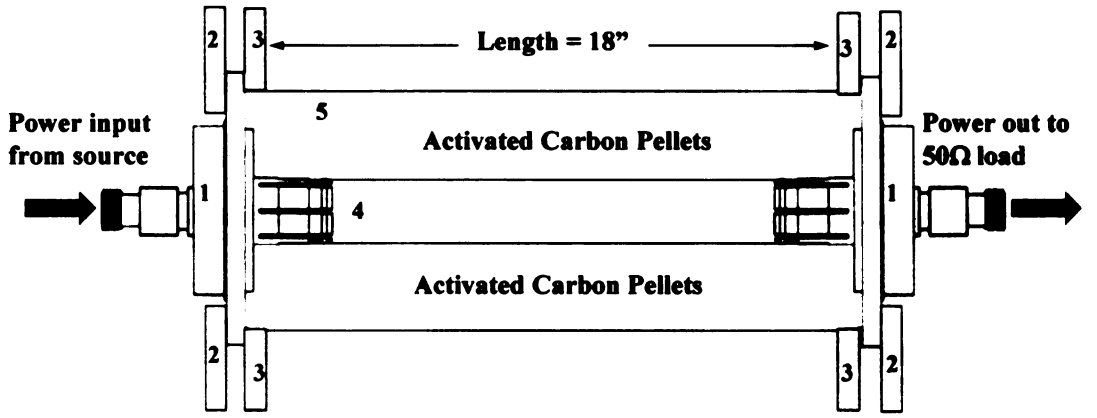

Figure 5.5. Microwave heating applicator bench top system set-up.

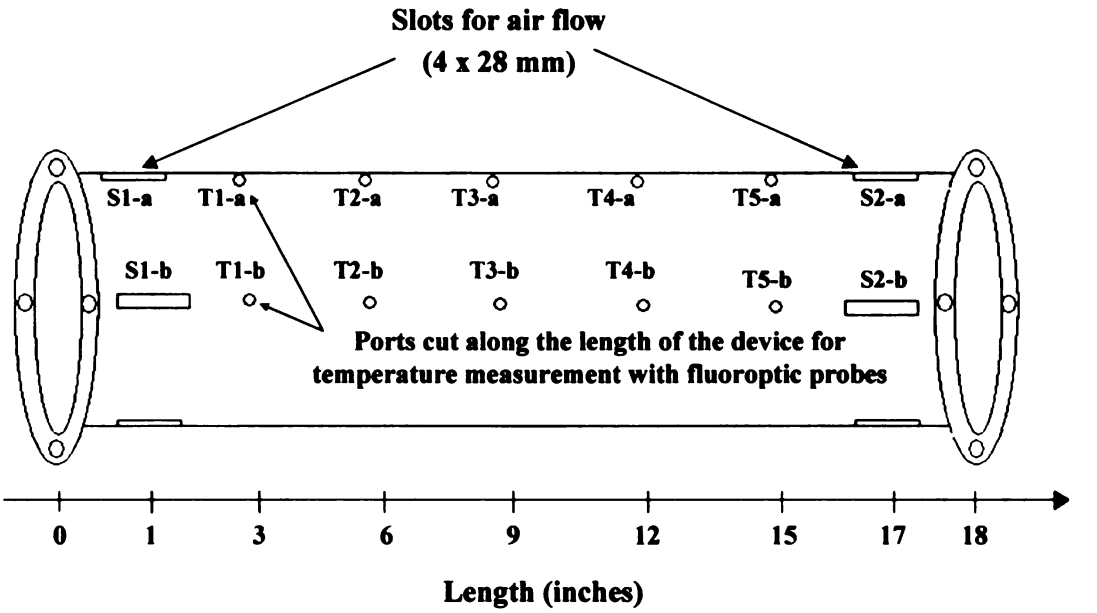

Figure 5.6. Outer conductor with ports for temperature measurement and slots for vapor.

5.4 Microwave Applicator Performance

5.4.1 Experimental Set-up

Figure 5.7 highlights the set-up for the microwave device. The magnetron was connected to a circulator, which was used to prevent the source from being damaged by any reflected power. The reflected power would instead be reflected to a 50 ohm load. At the end of the transmission line, any power was also sent to another 50 ohm load. To measure power, directional couplers and attenuators were attached to power meters to record forward, reflected, and outgoing power.

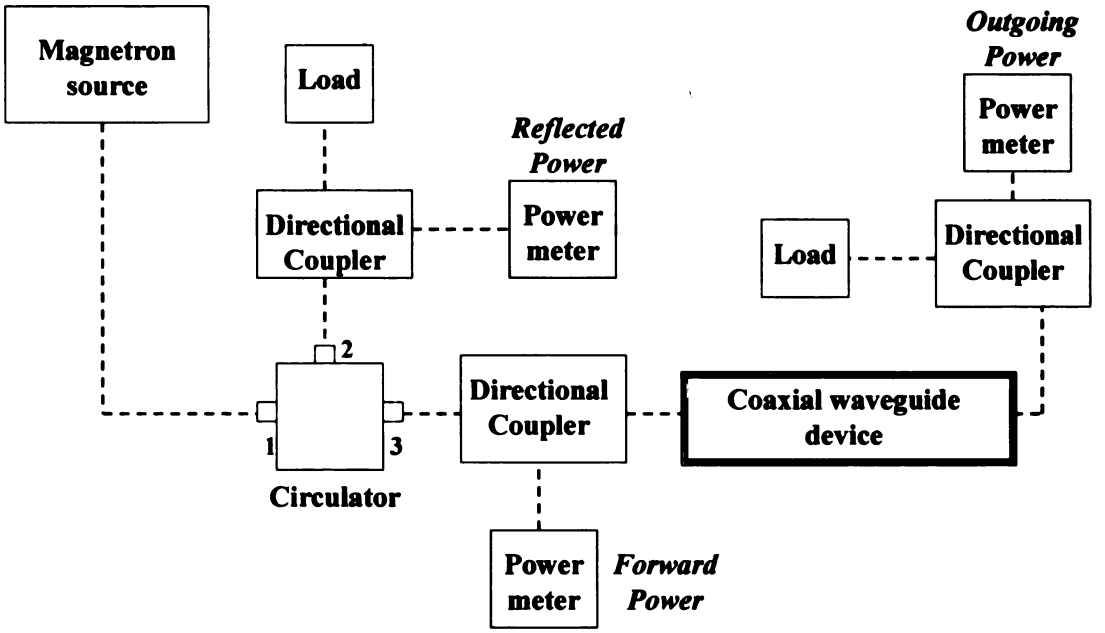

Figure 5.7. Microwave applicator bench-top system – experimental set-up.

5.4.2 Temperature Profile Measurements

Initial experiments were conducted to measure the temperature profile within the microwave heating system for varying power input. Also, it would be important to

measure the reflected power. Table 5.2 highlights the range of values for reflected power for different power inputs from the source.

Table 5.2. Range of reflected power for varied power inputs.

Avg. Forward Power (W)	Avg. Reflected Power (W)	Avg. Total Power (W)	% Reflected Power
53.6	1.12	54.7	2.05%
60.5	1.54	62.0	2.48%
71.4	1.65	73.1	2.26%
85.1	1.94	87.0	2.23%
101.0	2.50	103.5	2.42%
112.6	2.67	115.3	2.32%

As seen in this table and as predicted with earlier simulations, the reflected power remained very minimal. This implies that the power is going into the carbon and hence allowing the carbon to heat up. The circulator could be eliminated from the system since the reflected power remained so low.

For varying power inputs from the source, the temperature was measured at ports along the outer conductor. Figure 5.8 shows an example of the temperature profile for varying input power, with temperature measured 1" from the start of the applicator (Figure 5.6). As expected, the maximum temperature increased as the input power increases.

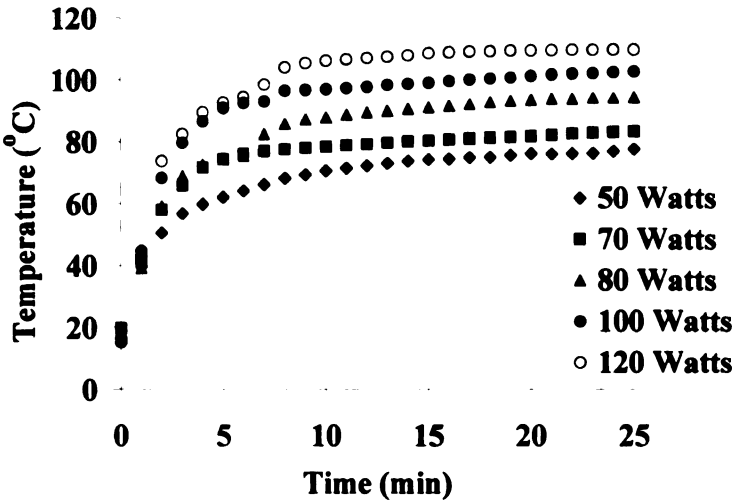

Figure 5.8. Temperature (°C) vs. time (min) for varying power inputs measured 1" from the start of the transmission line.

As the distance along the transmission line increased, the temperature decreased. Figure 5.9 shows the temperature measured at distances along the applicator length with an input power of 120 Watts. Further down the length of the device (after 12"), the temperature did not increase as much as for locations along the first half of the transmission line. The temperature at 17" from the start of the line only reached 35-40°C for the highest input power (120 Watts).

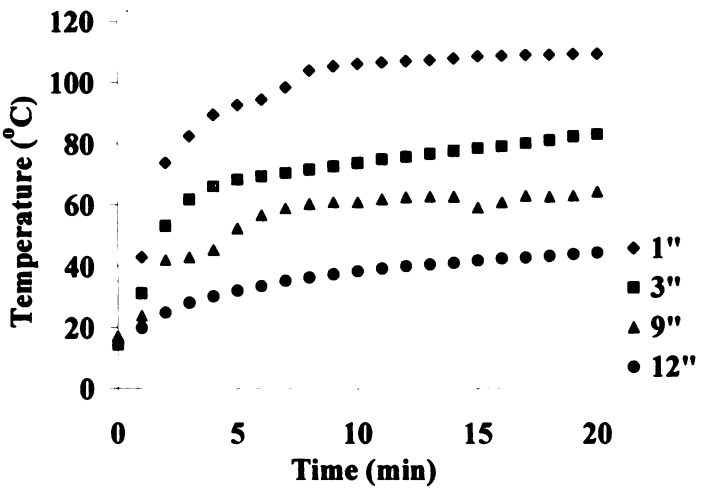

Figure 5.9. Temperature (°C) vs. time (min) for varying lengths along the 18" applicator with 120 Watts of input power.

Additionally, an investigation of the temperature profile radially as well as down the length of the transmission line would be important. Figures 5.10 includes a temperature profile for an input power of 80 Watts and compares temperatures measured at ports S1-a vs. S1-b, T1-a vs. T1-b, T2-a vs. T2-b, and T3-a vs. T3-b (see Figure 5.6). The depth of the probe into the device was varied to measure the temperature as the distance from the inner conductor to the outer conductor wall changes. Figure 5.11 shows the temperature profile for temperature measured at one location (S1-a) at varying probe depths (Power = 85W, Reflected Power = 2.1W).

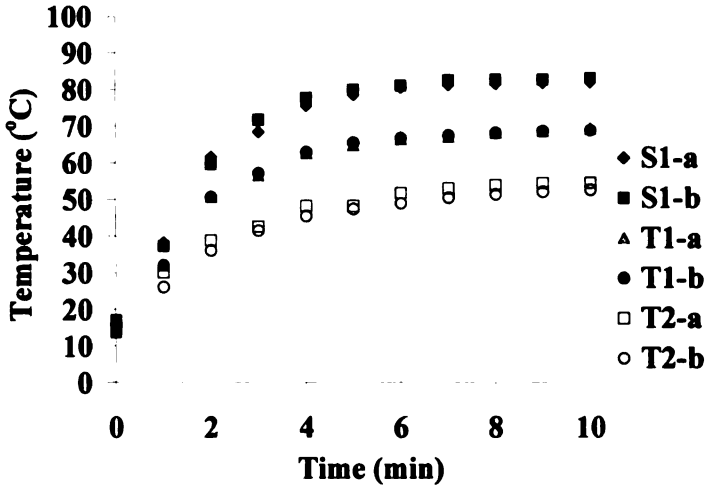

Figure 5.10. Temperature (°C) vs. time (min) comparisons for radial measurements for 18" microwave applicator, input power = 80 Watts.

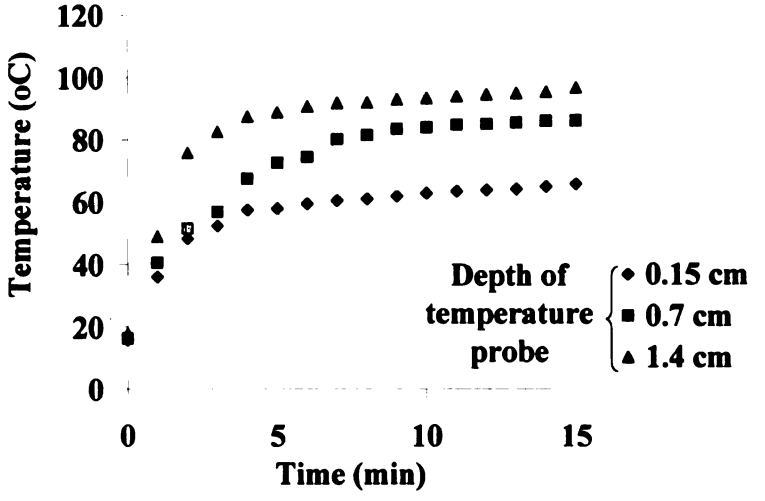

Figure 5.11. Temperature (°C) vs. time (min) at location S1-a for varying temperature probe depth for the 18" microwave applicator, input power = 85 Watts.

At the center near the inner conductor, the temperatures were at a maximum; whereas, towards the wall of the outer conductor, the temperature reached the minimum. This was

predicted with the earlier simulation calculations, and can be correlated to the electric field strength through the transmission line.

A supplementary power meter was added to measure power coming out of the transmission line before the 50 ohm load (see Figure 5.7). This power decreased over time and the plot of Power (W) vs. Time (sec) can found in Figure 5.12.

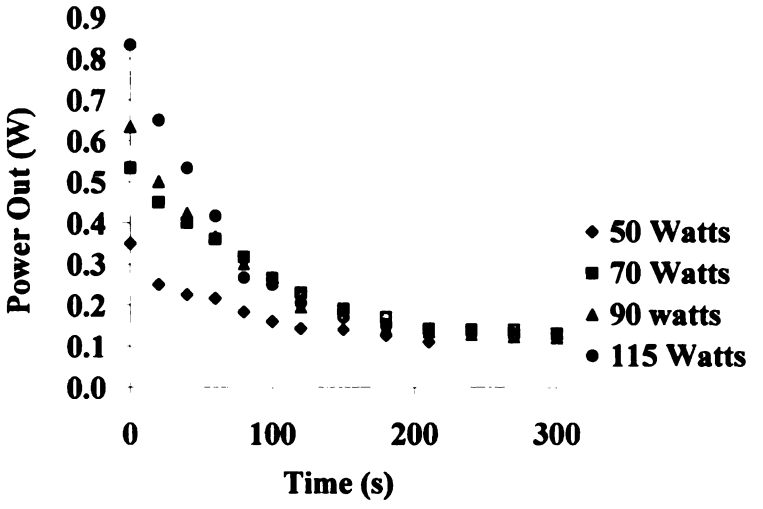

Figure 5.12. Outgoing power (W) vs. time (s) for 18" microwave applicator with varying input power.

The amount of power exiting the system at the start time increased for increasing power inputs, which can be expected. However, in all cases the carbon absorbs the majority of the incoming power and levels off after about 3 minutes. Roughly 95-98% of the power is absorbed by the activated carbon within the transmission line. This indicates the system is effective in heating the carbon efficiently.

5.4.3 Design Modifications

5.4.3.1 Change in Device Length

The bench top system for the full length microwave heating device as designed (18 inches) was shown to heat the activated carbon without generating "hot spots" along the length of the applicator. The average temperature in the carbon bed did not reach an adequate temperature necessary for activated carbon regeneration (150°C). A secondary bench-top system half the length of the original device (Figure 5.13) was constructed with the hope of using a shorting plate to elevate the average temperature in the carbon bed without increasing the input power.

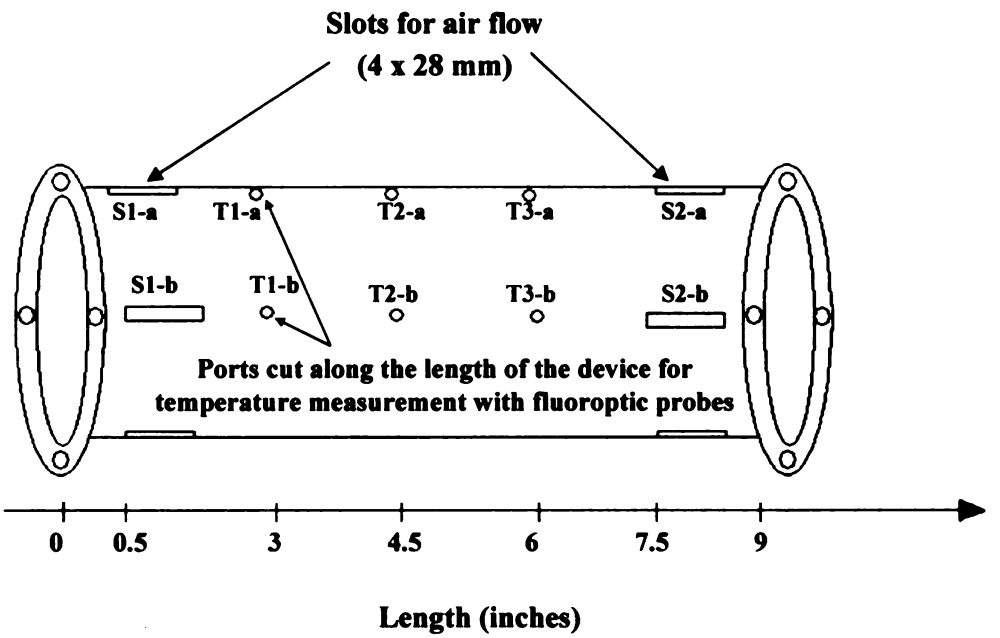

Figure 5.13. Revised (shortened) microwave heating device outer conductor with ports for temperature measurements and slots for vapor flow.

The decreased length of the system resulted in a different temperature profile throughout the transmission line at varied power inputs. Figure 5.14 below shows the temperature throughout the transmission line as a function of temperature for an input power of 80 Watts.

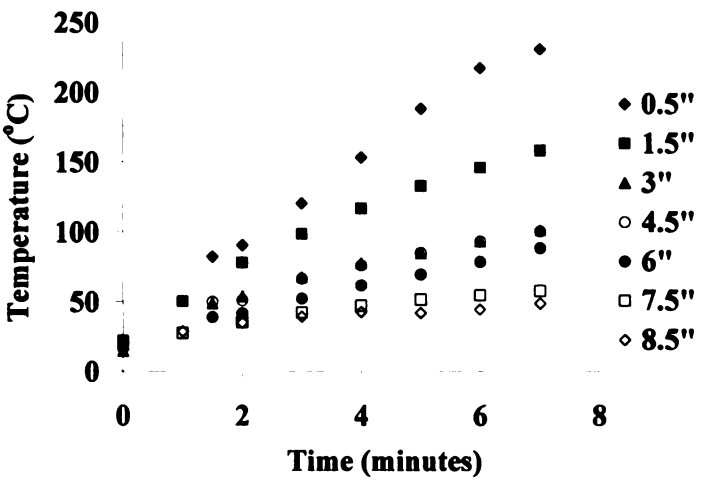

Figure 5.14. Temperature (°C) vs. time (min) for 9" microwave heating applicator with 80 Watts of input power.

When comparing the temperature profile for the 9" set-up to the same power input with the 18" set-up, it can be noted that the heating is much more efficient for the shorter device. This could be attributed to a better electrical connection for the shorter set-up, an improved impedance matching, or less heat lost due to convection.

5.4.3.2 Addition of Shorting Plate and Insulation

Earlier simulations were carried out to analyze the effects of placing a shorting plate at the end of the transmission line to reflect unabsorbed power back through the

carbon. Figure 5.15 shows the percent of power absorbed by the carbon in the newly revised bench-top system.

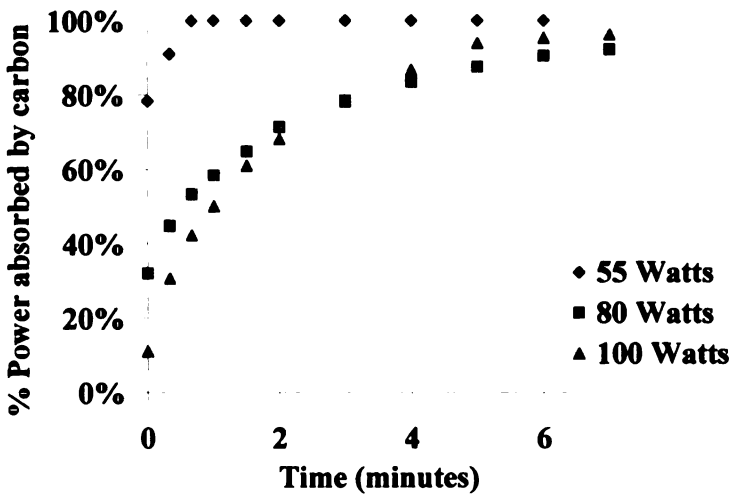

Figure 5.15. % Power absorbed by carbon vs. time (min) for 9" microwave applicator for varying input power.

As seen in Figure 5.15, because of the shortened length of the modified applicator, a higher percentage of power would be exiting the system, and after about 5 minutes of heating, all the input power is absorbed by the carbon. This power that is exiting the applicator during the initial heat-up can be used to heat the carbon near the end of the transmission line by placing a shorting plate at the end of the device, thereby allowing the carbon towards the end of the line to heat up more efficiently.

Figure 5.16 shows the temperature profile for this set-up with the additional shorting plate at the end of the transmission line for an input power of 100 Watts.

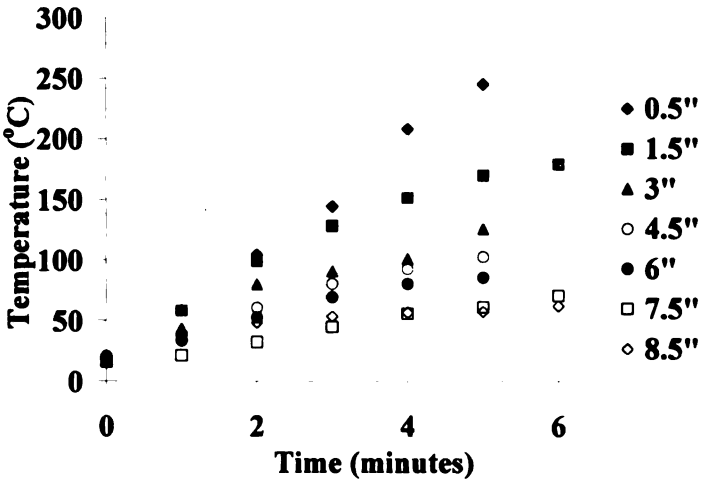

Figure 5.16. Temperature (°C) vs. time (min) for 9" microwave applicator with addition of a shorting plate with 100 Watts of input power.

The temperature at the very end of the transmission line (8.5") increases quickly for the first couple minutes, which goes along with the results from the power absorption measurements (Figure 5.15). After a couple minutes, the percentage of power absorbed by the carbon reaches 80%, so less power is being reflected at the end of the line; therefore, the increase in temperature at the end of the line is more noticeable for the first couple minutes of heating.

The reflected power was measured for cases with and without the additional short for the 9" transmission line, shown in Table 5.3.

Table 5.3. Average reflected power for different power inputs for 9" microwave applicator with and without a shorting plate.

Avg. Forward Power	Avg. Reflected Power	Avg. Total Power	Avg. % Reflected Power	
105	1.0	106	0.94%	with short
78.71	0.63	79.34	0.79%	
53.5	0.4	53.9	0.74%	
105.4	0.63	106.03	0.59%	without short
77.57	0.48	78.05	0.61%	
55	0.4	55.4	0.72%	

Still very little power was reflected back to the source, as was the case for the longer transmission line. Yet, when compared to results using the 18" transmission line (Table 5.2), the % reflected power was lower for each case. For both the 18" and 9" microwave heating devices, the reflected power was minimal; even the decrease seen for the shorter set-up did not account for the increased temperatures in the transmission line.

In order to answer the question of whether heating by convection allows for higher temperatures in the shorter transmission line (when compared to the 18" transmission line, both without a short), the original set-up was altered with an addition of fiberglass insulation around the transmission line (thickness = 2 in). The insulation did allow for an increased temperature as seen in Figures 5.17, which shows the temperature profile for 100 Watts, for both cases with and without insulation.

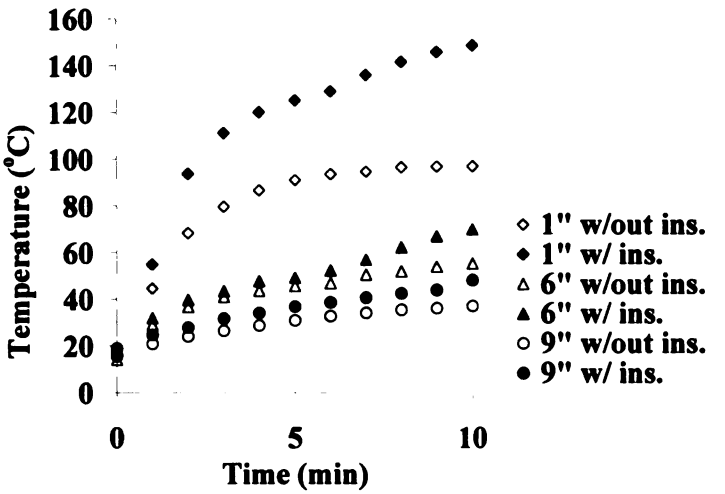

Figure 5.17. Temperature (°C) vs. time (min) for 18" microwave applicator with and without insulation, with input power of 100 Watts.

More noticeable changes were seen for temperatures closer to the start of the transmission line. Still the temperatures were not increased to the extent seen for the shorter device without a short (Figure 5.14). The same insulation was used for the 9" microwave heating device without the short added. Figure 5.18 is the resulting temperature profile for the 9" device with both insulation and an added shorting plate for 75 Watts input power.

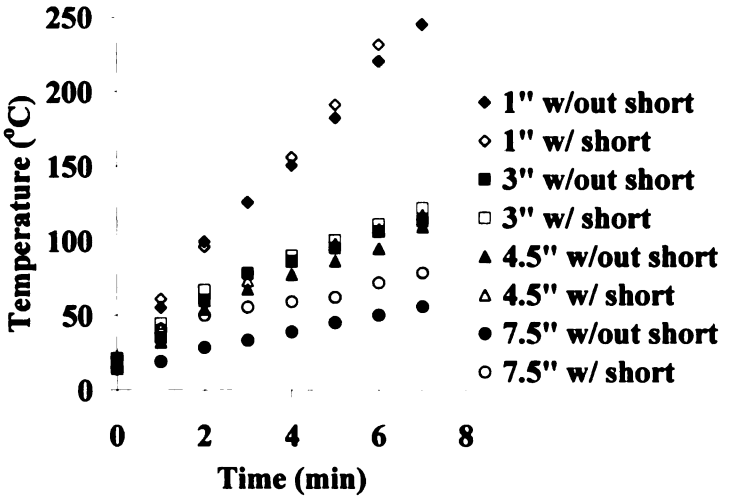

Figure 5.18. Temperature (°C) vs. time (min) for 9" microwave applicator with insulation, with input power of 75 Watts.

The additional short to the insulated 9" set-up resulted in a noticeable improvement in the temperatures further down the transmission line (towards the end). As seen in Figure 5.18, at 7.5" down the line, there was nearly a 30°C increase in temperature when a short is added to the system.

5.4.3.3 Power Cycling

It was observed that when the power was decreased toward the end of an experimental run, that the temperature near the beginning of the transmission line decreased rapidly; whereas, near the end of the line, the temperature still increased. In order to take advantage of this additional heating, the power was cycled from a high power to minimum power to decrease temperatures near the beginning of the line, while still increasing the temperature near the end of the line. Figure 5.19 is a plot of a case

where the power was kept constant at 100 W, but then cycled from 100 Watts to 5 Watts for the next 5 minutes.

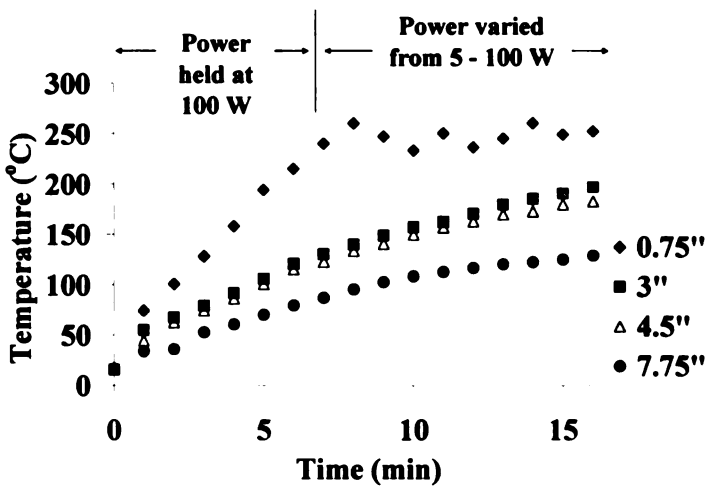

Figure 5.19. Temperature (°C) vs. time (min) for 9" microwave applicator with insulation and shorting plate, with cycling of power at the end of heating.

During the last 7 minutes of heating (while the power was cycled), an additional increase of 30°C was noted for the temperature at 3", 4.5", and 7.75", while an increase of only 10°C was noted 0.75" location.

Another test case was completed during which the power was ramped slowly from 50 Watts to 100 Watts, followed by the same cycling used previously. Figure 5.20 highlights the resulting temperature profile for this study.

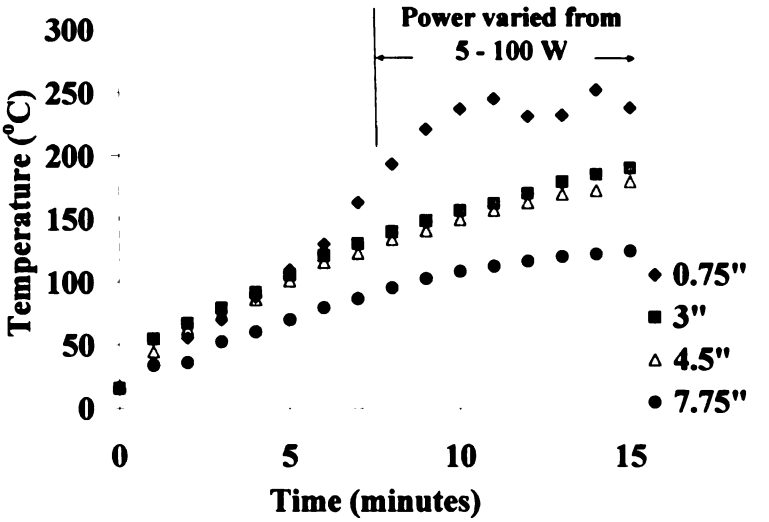

Figure 5.20. Temperature (°C) vs. time (min) for 9" microwave applicator with additional shorting plate and insulation, with cycling of power throughout heating time.

When comparing the two cases using the change in power, the first case resulted in better heating. The average temperature reached 120°C after 5 minutes of heating with only 120 Watts of input power. Further analysis will be devoted to raising the average temperature by using higher input power. Applications involving microwave heating of carbon may involve flowing a waste stream or vapor through the device, which would heat the carbon towards the end of the transmission line and thereby result in a more even heating pattern.

5.5 Modeling Microwave Heating

5.5.1 Energy Balance

Electromagnetic theory must provided the basis for the modeling. An energy balance for the system served as the foundation for the model with the following

elements taken into account: microwave energy absorbed, heat produced via chemical reactions (regeneration), heat removed by product gas, energy lost through radiation to the surroundings, heat used to increase the temperature of the carbon, and heat lost due to convection [7]. To predict the carbon temperature at locations along the microwave device, the solution for the energy balance over the system was used.

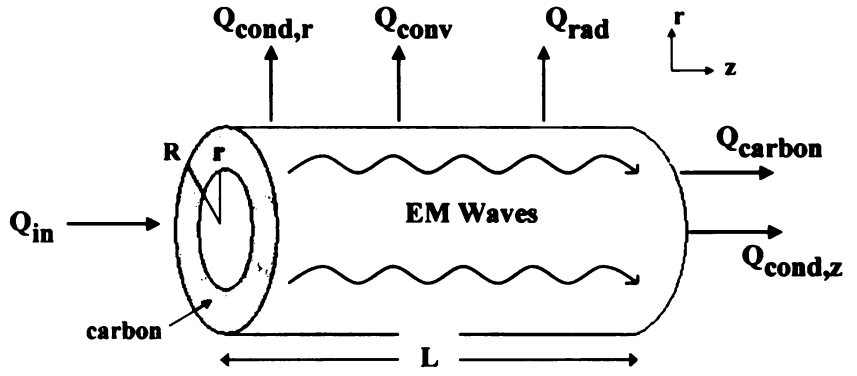

Basic Energy Balance:

$$Q_{in} = Q_{carbon} + Q_{cond,r} + Q_{cond,z} + Q_{conv} + Q_{rad}$$

Figure 5.21. Energy balance diagram for microwave heating applicator system.

The energy balance can be written for the system and includes heat by conduction ($Q_{cond,r}$ and $Q_{cond,z}$), heat lost by convection (Q_{conv}) and radiation (Q_{rad}) , heat used to increase the temperature of carbon, and the heat from the source or power absorbed by carbon (Q_{in}) [89].

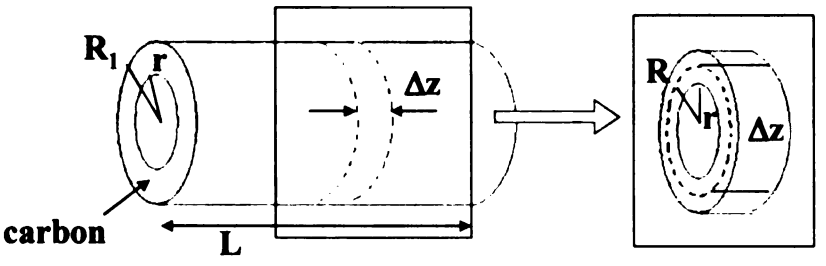

Figure 5.22. Shell balance used to solve the overall energy balance at a location, R from the inner conductor.

To simplify the energy balance for computational purposes, the conduction in the r-direction can be neglected. The distance (R-r) that is occupied by carbon is very small when compared to the length (L) of the device. The contribution of conduction in the z-direction will be significant and must be included for an accurate temperature prediction. Conduction will occur in both the r and z direction along the transmission line. As explained earlier, only conduction in the z-direction will be considered for these calculations. The conduction can be shown using the following equation:

$$Q_{conduction} = \pi(R^2 - r^2)[q_z|_z - q_z|_{z+\Delta z}] \tag{5.12}$$

$$q_z = -k_{carbon}\frac{\partial T}{\partial z} \tag{5.13}$$

The thermal conductivity of carbon, k_{carbon}, used for these calculations was 0.31 W/m K [ref].

The microwave energy generated by the source at various input powers will be absorbed by the activated carbon. The power absorbed per unit volume of carbon can be calculated at any point along the transmission line, using the following relationship,

$$Q_{absorbed} = \frac{|E|^2 \varepsilon'' \omega}{2} \tag{5.14}$$

where E is the magnitude of the electric field at the specific location in the carbon bed, ε" is the dielectric loss factor of the carbon, and ω is the angular frequency (2πf with f = frequency). The magnitude of the electric field was previously measured using Ansoft HFSS. The E-field magnitude was plotted for cross section with a constant r-value, thereby allowing values to be determined for various lengths, z, along the carbon line. The dielectric loss was measured for the activated carbon as previously discussed, and the following relationship was established between T and ε":

$$\varepsilon''(\text{F/m}) = 8.854 \times 10^{-12}(0.0004T - 0.0546) \quad (\text{T is in Kelvins}) \tag{5.15}$$

Heat loss occurs through two mechanisms, convection and radiation. The heat lost due to radiation can be represented with the following equation,

$$Q_{radiation} = \varepsilon\sigma A(T^4 - T_{air}^4) \tag{5.16}$$

$$A = 2\pi R\,\Delta z \tag{5.17}$$

where ε is the emissivity of the activated carbon (0.85), σ is the Stefan-Boltzman constant [$(5.67 \times 10^{-8}$ W/(m^2 K^4)], T_{air} is the temperature of the surrounding air, and T is the temperature of the carbon.

The heat lost through natural convection is shown below:

$$Q_{convection} = h\,A\,(T - T_{air}) \tag{5.18}$$

The temperature in this equation refers to the temperature at the wall. Taking into account the highly conductive metal of the wall and the very low thickness (1 mm), an assumption was made that the temperature of the carbon can be used for this equation.

The convection heat transfer coefficient, h, can be calculated using the Nusselt number (Nu). The relationships [ref] used to evaluate the Nusselt number and the convection heat transfer coefficient is as follows:

$$Nu = \frac{hD}{k_{air}} \tag{5.19}$$

$$Nu = 0.772\,C\,(GrPr)^{1/4} \tag{5.20}$$

$$Gr = \frac{D^3 \rho^2 g \beta \Delta T}{\mu^2} \qquad Pr = \frac{Cp\,\mu}{k_{air}} \qquad \beta = \frac{1}{T_f} \tag{5.21}$$

$$C = \frac{0.671}{\left[1 + \left(\frac{0.492}{Pr}\right)^{9/16}\right]^{4/9}} \tag{5.22}$$

In these equations for the Nusselt number for free convection from a horizontal cylinder, Gr (Graetz number) and Pr (Prandtl number) are both calculated using the properties of the surrounding air and the cylinder dimensions, where D is the diameter of the cylinder, ρ is the density of air, μ is the viscosity of air, Cp is the heat capacity of air, k_{air} (0.025 W/m K [ref]) is the thermal conductivity of air, and T_f is the film temperature for air. The Nusselt number was calculated to be 5, and the corresponding convection heat transfer coefficient was 3.29 W/m^{2}K [89-90].

The energy used to increase the temperature of the carbon in the device can be calculated as shown:

$$Q_{carbon} = \rho\,Cp\,(\pi(R^2 - r^2)\Delta z)\frac{\partial T}{\partial t} \tag{5.23}$$

The properties of carbon, r and Cp, are the density (0.30 g/cm^3) and heat capacity (1.5 J/g K), respectively.

Using the terms described in the previous sections, the overall energy balance can be written, as shown below:

$$\pi(R^2 - r^2)\left[q_z|_z - q_z|_{z+\Delta z}\right] + Q_{absorbed}(\pi(R^2 - r^2)\Delta z) - \ldots$$
$$\ldots (2\pi R)\Delta z\left[h(T - T_{air}) + \varepsilon\sigma(T^4 - T_{air}^4)\right] = \rho Cp\pi(R^2 - r^2)\Delta z\frac{\partial T}{\partial t} \tag{5.24}$$

After dividing by $\pi(R^2-r^2)\Delta z$ and taking the limit as z goes to zero, a partial differential equation results as follows:

$$\frac{-\partial q_z}{\partial z} + Q_{absorbed} - \frac{2R\left[h(T - T_{air}) + \varepsilon\sigma(T^4 - T_{air}^4)\right]}{(R^2 - r^2)} = \rho Cp\frac{\partial T}{\partial t} \tag{5.25}$$

The heat conduction can be represented as $q_z = -k\frac{\partial T}{\partial z}$ and substituted into the PDE,

$$\alpha\frac{\partial^2 T}{\partial z^2} + \frac{Q_{absorbed}}{\rho Cp} - \frac{2R}{\rho Cp(R^2 - r^2)}\left[h(T - T_{air}) + \varepsilon\sigma(T^4 - T_{air}^4)\right] = \frac{\partial T}{\partial t} \tag{5.26}$$

$$\alpha = \frac{k}{\rho Cp} \tag{5.27}$$

The following represent the boundary conditions for the overall energy balance:

$$\begin{aligned} &\text{at } t = 0 && T = T_0 && \text{(for all z)} \\ &\text{at } z = 0 && \frac{\partial T}{\partial z} = 0 \\ &\text{at } z = L && \frac{\partial T}{\partial z} = 0 \end{aligned} \tag{5.28}$$

Appendix B highlights the MATLAB functions used to solve this PDE with the boundary conditions.

5.5.2 Theoretical vs. Measured Temperature Profiles

The temperature was calculated at various locations (z) along the length of the transmission line. This was repeated at different locations (R) from the inner conductor,

since the E field also was dependent on r. For 50 Watts, the temperature was calculated at a distance r = 0.1cm (closest to the inner conductor) and these temperatures were compared to measured temperatures (see Figure 5.23). The temperatures are shown at locations 1, 3, 6, and 9 inches along the length of the transmission line. Similarly, Figure 5.31 shows the same results but for an input power of 100 Watts.

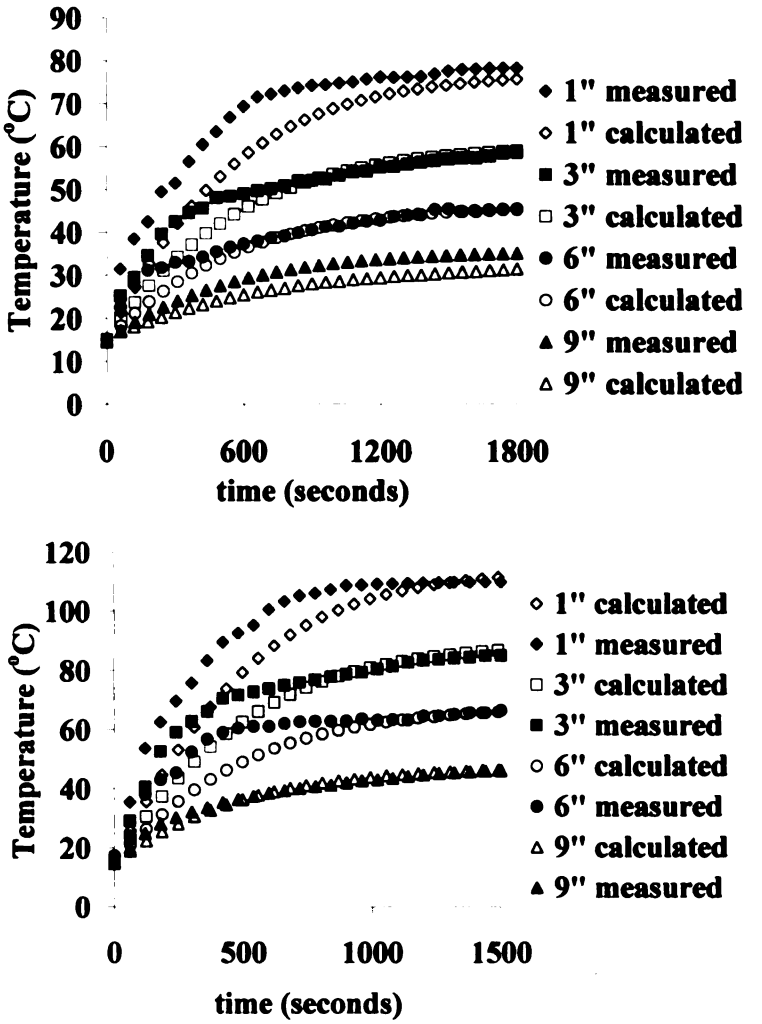

Figure 5.23. Comparison of temperature profiles (predicted vs. experimental) for 18" microwave heating applicator. *Top*: Temperature (°C) vs. time (seconds) for 50 W input power and *Bottom*: Temperature (°C) vs. time (seconds) for 100 W input power.

5.5.3 Effect of Nusselt Number

The temperatures did not vary greatly from the calculated temperatures; yet for the first 5-8 minutes of heating, the greatest difference was noted. This can be attributed to the low temperature of the wall and hence a lower Nusselt number for the initial heating time. The Nusselt number would be very low for the first few minutes of heating since the temperature of the wall is still very low. Figure 5.24 shows the effect of a lower Nusselt number on the temperature profile. As expected, the fit is better for Nu = 1.8 ($t < 500s$) and for Nu = 5 ($t > 800s$).

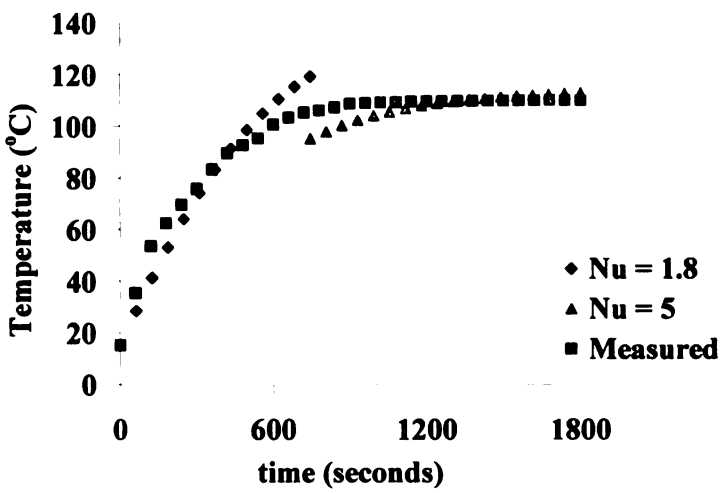

Figure 5.24. Temperature (°C) vs. time (sec) for 100 Watts forward power and varying Nusselt number.

5.6 Conclusions

Activated carbon was heated using a novel microwave based heating device; the problem of "hot spots" found in conventional microwave cavities was eliminated with

this device. The device was designed using Ansoft HFSS software and the dielectric characteristics of the activated carbon. Bench-top systems were constructed based on the design results; the temperature profiles indicated heating throughout the carbon bed. The device allows for the carbon to act as a load and absorb the input power and convert the power to heat since the carbon has a higher dielectric loss. The temperature profiles were modeled using an energy balance over the entire system. The average temperature reached 120°C after 5 minutes of heating with only 120 Watts of input power. Further analysis will be devoted to raising the average temperature by using higher input power. Applications involving microwave heating of carbon may involve flowing a waste stream or vapor through the device, which would heat the carbon towards the end of the transmission line and thereby result in a more even heating pattern.

CHAPTER 6 : Conclusions and Future Work

6.1 Magneto-dielectric Composites

6.1.1 Summary of Materials Design Results

Naturally occurring magneto-dielectric materials are often either non-magnetic at frequencies greater than 1 GHz or exhibit large loss at these frequencies. Other challenges with these materials include their high mass density, which can require external biasing for operation.

Macroscopic composites with magnetic reinforcement material (iron oxide nanocomposites) were fabricated with varying loadings of the iron oxide particles; however, in order to achieve the desired magnetic properties, the volume fraction required was 40% or higher. Such performance can be attributed to the geometry of the inclusions, which does not allow for a large magnetization in the composite; therefore, the permeability is near unity and the material is non-magnetic. Furthermore, the spherical ferrimagnetic particles used in this study have a demagnetization factor of 1/3, meaning that they must be very tightly packed in order to result in a significant increase in permeability. In doing so, the material integrity is sacrificed, since high volume fractions result in brittle composites with poor dispersion quality of iron oxide. High volume fractions would result in high mass density materials, not much better than using the ferrite in bulk. Also, for these composites with tightly packed (high volume fraction) inclusions and great contrast in the dielectric constant for the two phases, modeling these materials using the classical mixing laws would not be accurate.

A secondary approach to designing the magneto-dielectric composites utilized the idea of periodic arrays of metallic patches, which can be designed to act as "inductive"

inclusions, thereby enhancing the properties for the material. Engineered inductive inclusions were designed through one or more frequency selective surface, resulting in an "artificial" magnetic material with low mass density and controlled loss for frequencies greater than 2GHz (details of the design can be found in Chapter 4). What makes these designs novel is that the enhanced effective permeability is greater than 1; whereas, past work in metamaterials design involved designing artificial dielectrics (non-magnetic), dissipative materials like left-handed or double negative (DNG) materials, and other related technologies. The permeability and permittivity are both greater than 2 for frequencies from 2-5 GHz, with loss below 10^{-3}. Another novel aspect of these designs is that with permittivity and permeability both increased to the same extent, impedance matching becomes much easier for application purposes.

FSS element structure-material property relationships were developed for an array of design variables including element size and periodicity, polymer dielectric properties, and polymer thickness. Other variations included scan angle and polarization dependence, multiple layer FSS, and comparison between FSS in a waveguide and infinite FSS. By establishing these material-property relationships, one is able to exploit the flexibility of the FSS design to tailor the material properties based on the application.

The FSS layered composites were fabricated and characterized using a waveguide to measure the reflection and transmission to compare to modeled results. The measurements correlated well with the modeled results.

6.1.2 Future Impact and Outlook

As discussed throughout this thesis, there are several design challenges associated with advancing electromagnetic materials for applications including wireless technologies or energy transport, for example. The work presented here illustrates an approach to designing materials that can circumvent some of the current design difficulties. This approach offers wide flexibility in the magneto-dielectric design space, since the possibility for shapes or patterning is infinite.

This approach has been successfully illustrated through the results shown in Chapter 4; however, before these designs can be implemented in specific applications, further work would be required. Future work may involve optimization schemes to fine tune the FSS elements' shape. Furthermore, in applications, the thickness of the material would need to be reduced; as discussed in Chapter 4, utilizing a higher dielectric property polymer substrate would allow for a thinner composite with similar performance and bandwidth. By incorporating some of the concepts and results from earlier work at lower frequencies by using spherical ferromagnetic inclusions, a wider bandwidth can be achieved. This would require a co-design of layers and inclusions, so that their complementary effects will meet the overall design goal.

Another aspect of the design approach presented here that offers more flexibility for the designer is the possibility of incorporating multiple FSS layers but to use alternate shapes on the multiple FSS layers. For example, by combining dipoles and loops, both the capacitance and inductance can be enhanced.

6.2 Development of a Microwave Applicator for Activated Carbon

6.2.1 Summary of Applicator Design Results

Gasoline emissions can be controlled by flowing vapors through canisters filled with activated carbon to adsorb the vapors and burn them as they are drawn into the engine. However, as saving fuel is 'green,' and technologies have been developed to become more environmentally sound, hybrid vehicles have gained in popularity. For this type of vehicle, the gasoline engine is not running for large fractions of time; thereby requiring alternative measures for the heating and regeneration of the activated carbon.

Activated carbon was heated using a novel microwave based heating device; the problem of "hot spots" found in conventional microwave cavities was eliminated with this device. The device concept was similar to a coaxial waveguide or transmission line, with the activated carbon serving as the load to absorb the power and convert it to heat based on the dielectric characteristics of the carbon. After proper dielectric characterization of the activated carbon, the device was designed using Ansoft HFSS software. Bench-top systems were constructed based on the design results; the temperature profiles indicated heating throughout the carbon bed. The device allows for the carbon to act as a load and absorb the input power and convert the power to heat since the carbon has a higher dielectric loss. The temperature profiles were modeled using an energy balance over the entire system. The average temperature reached 120°C after 5 minutes of heating with only 120 Watts of input power.

6.2.2 Future Design Considerations

Further analysis will be devoted to raising the average temperature by using higher input power. Applications involving microwave heating of carbon may involve flowing a waste stream or vapor through the device, which would heat the carbon towards the end of the transmission line and thereby result in a higher average temperature in the carbon bed. Additionally, an improved model would be necessary to take into account the saturation of the carbon, as that would be affected by the heating and regeneration of carbon.

APPENDIX A: Extracting effective electromagnetic properties

The theoretical equations for determining reflection and transmission through a slab of unknown properties (e and m) are shown in Chapter 4. An iterative routine was used as a root selection scheme to use these equations and the calculated S-parameters from the Ansoft software in order to estimate the effective properties. MATLAB was used to extract the properties, and the code for this algorithm can be found below.

MATLAB M-file

```
Thick=0.03;                                  %slab thickness (m)
C=2.997925e8;                                %speed of light (m/s)
theta_deg = 0;                               %angle of incidence (degrees)
theta = theta_deg*pi()/180;                  %angle of incidence (radians)
FCR=1.e-5;                                   %tolerance
LUB=1.e-5;                                   %tolerance

ui=[2,0];                                    %initial guess for ε' and ε''
vi=[3,0];                                    %initial guess for μ' and μ''
UI=(ui(1)-sqrt(-1)*ui(2));
VI=(vi(1)-sqrt(-1)*vi(2));

%reading in S-parameter data from Excel spreadsheet
frequency = xlsread('case1.xls', 1, 'A2:A199');
S11_imaginary=xlsread('case1.xls',1,'B2:B199');
S11_real=xlsread('case1.xls',1,'C2:C199');
S21_imaginary=xlsread('case1.xls',1,'D2:D199');
S21_real=xlsread('case1.xls',1,'E2:E199');

%creating array for output ε and μ and S11 and S21
NR=length(frequency);
QRIMU21=zeros(2, NR);
QRIEP21=zeros(2, NR);

for i = 1:NR;
    QPS_s11(i)=S11_real(i)+sqrt(-1)*S11_imaginary(i);
    QPS_s21(i)=S21_real(i)+sqrt(-1)*S21_imaginary(i);
end
```

```
%calling function "extract" to calculate ε and μ
for pk=1:NR,
      QF=frequency(pk)*1e9;
      Omega=2*pi*QF;
      S21s=QPS_s21(pk);
      S11s=QPS_s11(pk);
[U(pk),V(pk)] = extract(UI,VI,FCR,LUB,Thick,S11s,S21s,Omega,C,theta);
end

%output ε and μ
QEP21=U;
QMU21=V;
QRIMU21=[real(QMU21);imag(QMU21)];
QRIEP21=[real(QEP21);imag(QEP21)];


%function "extract" - a root selection routine which calls subfunctions
%"W" and "Z" to calculate S11 and S21 using initial guess ε and μ to
%compare to numbers read in from the Excel sheet
function [U,V] = extract(UI,VI,FCR,LUB,Thick,S11s,S21s,Omega,C,theta)
    for kk=1:10000,
        NOI=kk;
      if NOI == 10000,
            disp('Too many iterations');
      else
            DU=FCR*UI;
            DV=FCR*VI;
            W0=W(UI,VI,Thick,S11s,Omega,C,theta);
            Z0=Z(UI,VI,Thick,S21s,Omega,C,theta);
            WU=(W(UI+DU,VI,Thick,S11s,Omega,C,theta)-W0)/DU;
            WV=(W(UI,VI+DV,Thick,S11s,Omega,C,theta)-W0)/DV;
            ZU=(Z(UI+DU,VI,Thick,S21s,Omega,C,theta)-Z0)/DU;
            ZV=(Z(UI,VI+DV,Thick,S21s,Omega,C,theta)-Z0)/DV;
            DET=WU*ZV-WV*ZU;
            DLU=(WV*Z0-ZV*W0)/DET;
            DLV=(ZU*W0-WU*Z0)/DET;
            U=UI+DLU;
            V=VI+DLV;
            T=sqrt(abs(DLU*DLU)+abs(DLV*DLV));
      if T > LUB
            UI=U;
            VI=V;
      else
                break
            end
        end
    end


%subfunction "W" which calculates the difference in the S11 calculated
%from the initial guesses and the S11 from the Excel spreadsheet
function [W] = W(EP,MU,Thick,S11s,Omega,C,theta)
Beta=sqrt(((Omega/C)*sqrt(EP*MU))^2-((Omega/C)*sqrt(1)*sin(theta))^2);
Shift=exp(-i*Beta*Thick);
Gam=(sqrt(MU/EP)-1.)/(sqrt(MU/EP)+1.);
```

```
W=Gam*(1.-Shift^2)/(1.-(Gam*Shift)^2)-S11s;
return
%subfunction "Z" which calculates the difference in the S21 calculated
%from the initial guesses and the S21 from the Excel spreadsheet
function [Z] = Z(EP,MU,Thick,S21s,Omega,C,theta)
Beta=sqrt(((Omega/C)*sqrt(EP*MU))^2-((Omega/C)*sqrt(1)*sin(theta))^2);
Shift=exp(-i*Beta*Thick);
Gam=(sqrt(MU/EP)-1.)/(sqrt(MU/EP)+1.);
Z=Shift*(1.-Gam^2)/(1.-(Gam*Shift)^2)-S21s;
return
```

Validation

In order to validate that the extraction code shown above was correctly extracting the effective properties, the reflection and transmission data for a material with known properties, specifically Rogers (RT) Duroid 6006, were used as the input for the code. Figure A.1 below shows the output effective properties which correlated with the known material properties for Rogers (RT) Duroid 6006 ($\varepsilon = 6.15 - 0.0019\,j$ and $\mu = 1$).

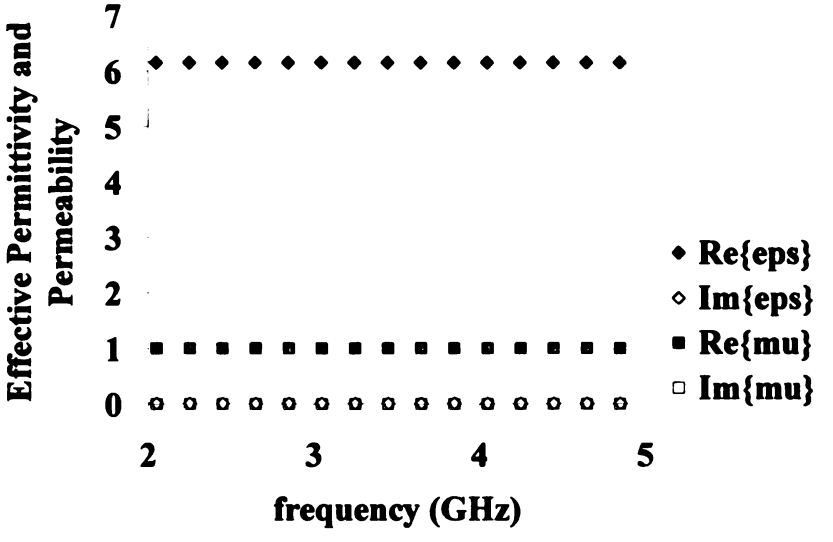

Figure A.1. Effective properties for Rogers (RT) Duroid 6006 as extracted with the MATLAB code.

APPENDIX B: Modeling of microwave heating

To model the microwave heating in the applicator designed in Chapter 5, an energy balance over the system was analyzed. The shell balance and resulting partial differential equation as well as the boundary conditions are explained in Chapter 5. MATLAB was used to solve the PDE at a certain cross section (R) from the center point and along the length of the transmission line. The function "pdepe" is a MATLAB function used to solve parabolic PDE's that follow the following format:

$$c(x,t,u,\frac{\partial u}{\partial x})\frac{\partial u}{\partial t} = x^{-m}\frac{\partial}{\partial x}(x^m f(x,t,u,\frac{\partial u}{\partial x})) + s(x,t,u,\frac{\partial u}{\partial x})$$

When compared with the PDE from Section 5.5, we have the following relations (knowing that x = z and u = T for the microwave problem):

$$c(x,t,u,\frac{\partial}{\partial x}) = 1$$

$$m = 1$$

$$f(x,t,u,\frac{\partial u}{\partial x}) = \alpha\frac{\partial T}{\partial z}$$

$$s(x,t,u,\frac{\partial u}{\partial x}) = \frac{Q_{absorbed}}{\rho Cp} - \frac{2R}{\rho Cp\,(R^2 - r^2)}[h(T - T_{air}) + \varepsilon\sigma(T^4 - T_{air}^4)]$$

To us the MATLAB function "pdepe," when entering the boundary conditions, they must satisfy the following expression:

$$p(x,t,u) + q(x,t)f(x,t,u,\frac{\partial u}{\partial x})) = 0$$

Therefore, for our case, with the limits being z = 0 and z = L, the boundary conditions must satisfy that p = 0 and q = $1/\alpha$ for both boundaries. The initial condition is that at t =

0, T = T_0. The following is the M-file used for solving the PDE and includes the sub functions used to solve for the temperature profile.

MATLAB M-file

```
% spacing the points for the length and time and setting the variables
clear all
m = 0;
x = linspace(0,.4572,50);
t = linspace(0,1800,30);

% calling MATLAB function "pdepe" to solve the equations
sol = pdepe(m,@pdex1pde,@pdex1ic,@pdex1bc,x,t);
u = sol(:,:,1);
u=u-273;    %output temperature along length of trans line in deg. C


%function "pdex1pde" creates the PDE and variables
function [c,f,s] = pdex1pde(x,t,u,DuDx)

u_o = 300;          %initial temperature in K
rho = 300000;       %density of carbon in g/m3
Cp=1.3;             % heat capacity of carbon in J/g K

A = 0.05570945;      % surface area for convection in m^2
D_outer = 0.0387858; % outer diameter for h calculation

r=0.0042;       % radial location for measurement of temperature in m
r_outer=0.020;

Nu=2.5;             % Nusselt number
k_air = 0.04;       % air thermal conductivity in W/mK
h= k_air*Nu/D_outer;
alpha = 0.225/rho/Cp;

%inputting variables for the PDE to be solved
c = 1;
f = alpha*DuDx;
s = 2*(3182.5*exp(-3.4304*x))^2*(0.0004*u-0.0546)*8.854*1e-
12*pi()*2.45e9/rho/Cp-h*(2*r_outer)/(r_outer^2-r^2)/rho/Cp*(u-u_o)-
(0.85*(2*r_outer)/(r_outer^2-r^2)*5.67e-8)/rho/Cp*(u^4-u_o^4);


%function "pdex1bc" creates the boundary conditions
function [pl,ql,pr,qr] = pdex1bc(xl,ul,xr,ur,t)
rho = 300000;       %density of carbon in g/m3
Cp=1.3;
```

```
alpha = 0.225/rho/Cp;

pl = 0;
ql = 1/alpha;
pr = 0;
qr = 1/alpha;


%function "pdex1ic" creates the initial conditions at t=0
function u0 = pdex1ic(x)
u_o = 288;          %initial temperature in K
u0 = u_o;
```

BIBLIOGRAPHY

1. Mosallaei, H. and K. Sarabandi. "Magneto-dielectrics in Electromagnetics: Concepts and Applications." *IEEE Transactions on Antennas and Propagation.* 52(6): 1558-1567, 2004.

2. Ikonen, P., et al. "Magnetodielectric Substrates in Antenna Miniaturization: Potential and Limitations." *IEEE Transactions on Antennas and Propagation.* 54(11): 3391-3399, 2006.

3. Ermutlu, M.E., et al. "Miniaturization of Patch Antennas with New Artificial Magnetic Layers." *IEEE International Workshop on Antenna Technology.*

4. Golt, M.C., et al. "Magnetic and Dielectric Properties of Composites Consisting of Oriented, Iron Flake Filler within a Thermoplastic Host: Part I. Material Fabrication and Electromagnetic Characterization." *Journal of Thermoplastic Composite Materials.* 2008.

5. Golt, M.C., et al. "Magnetic and Dielectric Properties of Composites Consisting of Oriented Iron Flake Filler within a Thermoplastic Host: Part II. Transport Model Review and Evaluation." *Journal of Thermoplastic Composite Materials.* Vol. 22, 2009.

6. Mirza, I., et al. "A Study of Loop Antenna Miniaturization Using Split Ring Resonators." IEEE Antennas and Propagation International Symposium. pp. 865-1868. 2007.

7. Ania, C.O., et al. "Microwave-induced regeneration of activated carbon polluted with phenol. A comparison with conventional thermal regeneration." *Carbon.* 42. 2004. 1383-1387.

8. Kong, Y. and Y.C. Cha. "Microwave-induced Regeneration of NOx Saturated Char." *Energy and Fuels.* 10. 1996. 1245-1249.

9. Price, D.W. and P.S. Schmidt. "Microwave Regeneration of Adsorbents at Low Pressure: Experimental Kinetic Studies." *Journal of Microwave Power and Electromagnetic Energy.* 32(3). 1995.

10. Pozar, D. *Microwave Engineering.* 2nd Edition. John Wiley & Sons. 1998.

11. Harrington, R. F. *Time Harmonic Electromagnetic Fields.* IEEE Press, pp. 1-65. 2001.

12. http://image.absoluteastronomy.com/images/encyclopediaimages/d/di/dielectric_responses.svg.png.

13. Gammon, D.C., Electromagnetic Scattering Properties of Selected Magnetic Thin Films. Masters Thesis: Air Force Institute of Technology. 1989.

14. Ishimaru, A., Electromagnetic Wave Propagation, Radiation, and Scattering. New Jersey: Prentice Hall. 1991.

15. http://www.polyflon.com

16. http://rogers-corp.com/mwu/translations/prod.htm

17. http://www.arlonmed.com

18. http://www.dupont.com

19. http://rogers-corp.com/cmu/pdf/matl3.pdf

20. http://www.rdcircuits.com/vendorspecs.html

21. Endo, Y., et al. "Air and Water Permeation Resistance across Dust Cake on Filters: Effects of Particle Polydispersity and Shape Factor," Special Issue in Memory of Dr. Iinoya, Powder Technology, 118(1-2), 24-31, 2001.

22. Woo, K.S., et al. "Use of Continuous Measurements of Integral Aerosol Parameters to Estimate Particle Surface Area," Special Issue on Particulate Matter and Health: The Scientific Basis for Regulatory Decision, Aerosol Science and Technology, 34(1), p57-65, 2001.

23. Woo, K.S., et al. "Measurements of Atlanta Aerosol Size Distribution: Observation of Ultrafine Particle Events," Special Issue on Particulate Matter and Health: The Scientific Basis for Regulatory Decision, Aerosol Science and Technology, 34(1), p75-87, 2001.

24. Huang, J. and Richard B. Kaner, "A General Chemical Route to Polyaniline Nanofibers," J. Am. Chem. Soc., 126, 851, 2004.

25. Huang, J., et al., "Polyaniline Nanofibers: Facile Synthesis and Chemical Sensors," J. Am. Chem. Soc., 125, 314, 2003.

26. Virji, S., et al.. "Polyaniline Nanofibers as Gas Sensors: Response to Classes of Vapors and Comparison to Thin Films," *Nano Lett.*, 4(3), 591, 2004.

27. Hay, J.N. and S. J. Shaw. 2000. *Nanocomposites - Properties and Applications.* Abstracted from "A Review of Nanocomposites 2000."

28. Vaia, R. and R. Krishnamoorti. 2001. "Polymer Nanocomposites: Introduction." *Polymer Nanocomposites: Synthesis, Characterization, and Modeling.* American Chemical Society, pp. 1-7.

29. Kickelbick, G. and U. Shubert. 2003. "Organic Functionalization of Metal Oxide Nanoparticles." *Synthesis, Functionalization, and Surface Treatment of Nanoparticles.* American Scientific Publishers, pp. 91-101.

30. Park, S.S. et al. 2003. "Processing of Iron Oxide-epoxy Vinyl Ester Nanocomposites." *Journal of Composite Materials.* 37(5): 465-476.

31. Yang, C. et al. 2005. "Effect of ultrasonic treatment on dispersibility of Fe_3O_4 nanoparticles and synthesis of multi-core Fe_3O_4/SiO_2 core/shell nanoparticles." *Journal of Materials Chemistry.* 15: 4252-4257.

32. Mallikarjuna, N.N., et al. 2005. "Novel High Dielectric Constant Nanocomposites of Polyanaline Dispersed with γ-Fe_2O_3 Nanoparticles." *Journal of Applied Polymer Science.* 97:1868-1874.

33. Bai, Y., et al., "High dielectric constant ceramic powder polymer composites," *Applied Phys. Letters*, 76, pp. 3804-3806, 2000.

34. Vollath, D., et al. "Synthesis and properties of ceramic-polymer composites," *Nanostructured Mater.*, 12, pp. 433-438, 1999.

35. Lebedev, S.M., D.P. Agoris, and O.S. Gefle, "Application of new composite materials for the field control in solid dielectrics," *Proc. 6th Intl. Conf. Properties & Application of Dielectric Mater.*, Xi'an, China, June 21-26, 2000, p. 101-103.

36. Calberg, C., et al. "Electrical and dielectric properties of carbon black filled co-continuous two-phase polymer blends," *J. Phys. D: Appl. Phys.*, 32, pp. 1517-1525, 1999.

37. Nakamura, S., et al. "Dielectric properties of carbon black – Polyethylene composites below the percolation threshold," *Proc. on Electrical Insulation and Dielectric Phenomena*, pp. 293-296, 1999.

38. Priou, E. Dielectric properties of heterogeneous materials., *Progress in Electromagnetic Research*, PIER-6, p. 398, 1992.

39. Van Beek, L. Dielectric behavior of heterogeneous systems, *Progress in Dielectrics*, 7, pp. 69-114, 1967.

40. Jonscher, A.K. "Low-loss dielectrics," *J. Mater. Sci.*, 34, pp. 3071-3082, 1999.

41. Boudida, A., et al. "Permittivity of lossy composite materials," *J. Appl. Phys.*, 83, pp. 425-431, 1998.

42. Brosseau, C., A. Beroual, and A. Boudida, "Permittivity com composite composites," *Proc. Conf. on Electrical Insulation and Dielectric Phenomena*, pp. 74-77, 1999.

43. Yamada, T., et al. "Piezoelectricity of a high-content lead zirconate titanate/polymer composite," *J. Appl. Phys*, 53, pp. 4328-4332, 1982.

44. Jayasundere, N. and B.V. Smith, "Dielectric constant for binary piezoelectric 0-3 composites," *J. Appl. Phys.*, 73, pp. 2462-2466, 1993.

45. Grimes, C., "Calculation of Anomalous Permeability and Permittivity Spectra" *IEEE Transactions on Magnetics*, 27, pp. 4310-4316, 1991.

46. Slama, J., et al. "The model simulating the magnetic properties of composite polymers," *Int. J. Applied Electromagnetics and Mechanics*, 11, pp. 19-26, 2000.

47. Meta-Materials Workshop, DARPA/DSO, Sept. 2000.

48. Cui, T., et al. *Metamaterials: Theory, Design, and Applications*. Springer. 2009.

49. Walser, R. "Metamaterials: An Introduction" from *Introduction to Complex Media for Optics and Electromagnetics*. SPIE Publications. 2003.

50. Kazantsev, Y., et al. "Broadening of Operating Frequency Band of Magnetic-Type Radio Absorbers by FSS Incorporation." *IEEE Transactions on Antennas and Propagation*. 58(4): 1227-1235. 2010.

51. Zhang, J.C., et al. "Resonant Characteristics of Frequency Selective Surfaces on Ferrite Substrates." *Progress in Electromagnetics Research*. 95, 355-364. 2009.

52. Oraizi, H. and M. Afsahi. "Design of Metamaterial Multilayer Structures as Frequency Selective Surfaces." *Progress in Electromagnetics Research*. 6, 115-126. 2009.

53. Gorkunov, M., et al. "Effective magnetic properties of a composite material with circular conductive elements." *The European Physical Journal B*. 28: 263-269. 2002.

54. Stupf, M., et al. "Some Novel Design for RFID Antennas and Their Performance Enhancement with Metamaterials." *Microwave and Optical Technology Letters*. 49(4): 858-867. 2007.

55. Yang, T., et al. "Magneto-dielectric properties of polymer – Fe_3O_4 nanocomposites." *Journal of Magnetism and Magnetic Materials*. 320: 2714-2720. 2008.

56. Mosallaei, H. and Kamal Sarabandi. "Engineered Meta-substrates for Antenna Miniaturization." *URSI EMTS*. 2004.

57. Nussbaum, A. *Electromagnetic and Quantum Properties of Materials*. Prentice-Hall. 1966.

58. Kobidze, G. et al. 2005. "A novel and efficient method for accurate analysis of scattering from periodically arranged nano-structures." *MSU Electrical and Computer Engineering Technical Report*, pp. 1-37.

59. Agilent Technologies, *Agilent E4991A RF Impedance/Material Analyzer Operation Manual*, Agilent, July 2006.

60. Zong, L., Zhou, S., Sgriccia, N., Hawley, M., Sun, R., Kempel, L. "Dielectric properties of an epoxy-amine system at a high microwave frequency". *Polymer Engineering and Science*, 42(15), 2871-2877, 2005.

61. Killips, D., *Composite material design and characterization for RF applications*, Ph.D Thesis, Michigan State University. 2007.

62. Munk, B. *Frequency Selective Surfaces: Theory and Design*. John Wiley & Sons. 2000.

63. Munk, B. *Finite Antenna Arrays and FSS*, Wiley, New York, NY, 2003.

64. Weile, D.S. and E. Michielssen, "The control of adaptive antenna arrays with genetic algorithms using dominance and diploidy," *IEEE Transactions on Antennas and Propagation*, 49, 10, 1424 – 1433, Oct. 2001.

65. Mittra, R., C.H. Tsao, and W.L. Ko, "Frequency selective surfaces with applications in microwaves and optics," *IEEE Microwave Symp.*, 80, 447-449, 1980.

66. Peterson, A., S. L. Ray and R. Mittra. *Computational Methods for Electromagnetics*, IEEE Press, New York, NY, 1997.

67. Wang, J.J., *Generalized Moment Methods in Electromagnetics*, Wiley, New York, NY, 1991.

68. Wu, T.K., *Frequency Selective Surface and Grid Array*, Wiley, New York, NY, 1995.

69. Hooberman, B. "Everything you ever wanted to know about frequency-selective surface filters but were afraid to ask." May 2005.

70. *Automotive Emissions: An Overview.* http://www.epa.gov/otaq/consumer/05-autos.pdf.2005.

71. Wei, J.B., T. Shidaker, and M.C. Hawley. "Recent progress in microwave processing of polymers and composites." *Trends in Polymer Science.* 4(1). 1986. 18-24.

72. Wei, J., et al., *SAMPE Journal*, 27(1), p. 33, 1991.

73. Wei, J., et al.. Microwave Processing of Materials V, *Materials Research Society Symposium Proceedings*, 430, pp. 21-28, 1996.

74. Adegbite, V., Ph.D. Dissertation, Michigan State University, 1995.

75. Qui, Y., et al., *27th International SAMPE Technical Conference Proceedings*, pp.173-183, October 1995.

76. Fellows, L. et al., *26th International SAMPE Technical Conference*, Oct. 1994.

77. Qiu, Y. and M.C. Hawley, Proceedings of the 13th Annual Technical Conference, American Society for Composites, 1998.

78. Qiu, Y. Ph.D. Dissertation, Michigan State University, 2000.

79. Hawley, M., et al. "Microwave Pultrusion Apparatus and Method of Use", U.S. Patent, No. 5,470,423, Nov. 28, 1995.

80. Hawley, M., et al. "Improved Electromagnetic Curing Apparatus and Method of Use", Michigan State University, Patent number 5,406,056, 1995.

81. Hawley, M., et al. "Novel Microwave Applicator Design for Processing of Polymers and Composites", *Michigan State University Invention Disclosure* Number 93-038, 1993.

82. Wei, J., et al. "Scale-up Study of the Microwave Heating of Polymers and Composites", *37th Intern. SAMPE*, Anaheim, CA, March, (1992).

83. Fellows, L. and M. Hawley, "Thermogravimetric Analysis System with a Single-Mode Microwave Cavity", *Michigan State University Invention Disclosure.* Number 93-066, 1993.

84. Wei, J., et al. "Dielectric and Crystallinity Analysis of Poly(ethylene terephthalate)", *MRS Spring Meeting*, CA, San Francisco, April, (1994).

85. Delgado, R., et al. "Identification of Dielectric Relaxation Mechanism of a Thermosetting Polycarbonate", *AIChE 1993 Summer National Meeting*, Seattle, Washington, (1993).

86. Wei, J., Hawley, M., and M. T. Demeuse, *Polymer Engineering and Science*, 35(6), 461 (1995).

87. Zhou, S; Yang, H; Zong, L; Hawley, MC. Status of Microwave Adhesive Bonding Research. *Proceedings of 2001 SPE Automotive Composites Conference*. (2001).

88. Zhou, S; Hawley, MC. "A Study of Effect of Conducting Additives on Microwave Heating and Curing Rates of Epoxy". *Proceedings of 46th International SAMPE Symposium*: 2243 (2001).

89. Bird, R., Stewart, W., and E. Lightfoot. *Transport Phenomena*. 2nd Edition. Wiley. 2001.

90. Rice, R. and D. Do. *Applied Mathematics and Modeling for Chemical Engineers*. Wiley. 1994.